University of Southern Queensland

MODELLING AND NUMERICAL INVESTIGATIONS OF TRANSCRANIAL FOCUSED ULTRASOUND STIMULATION

A Thesis Submitted by

Yi Huang

For the award of

Doctor of Philosophy

2022

ABSTRACT

Transcranial focused ultrasound is a non-invasive stimulation modality delivering mechanical energy to deeper brain regions in the form of an acoustic pressure wave, which can result in numerous bioeffects. Computational techniques and models are becoming increasingly relevant to creating and optimising stimulation devices, treatment efficacy, safety evaluation, and improving knowledge of the underlying physical and physiological mechanisms. They provide a high level of control and ease the investigation of enormous parameter spaces. This thesis is to numerically investigate the applications of transcranial focused ultrasound based on detailed human head models constructed from medical images. Specifically, the influence of energy distribution within the brain tissues was studied using customised, focused ultrasound transducers. Secondly, the mechanical and cavitation indexes, as two metrics reflecting ultrasound-induced brain blood barrier disruption, are used to analyse the changes in intracranial fields. Thirdly, the effects of low-intensity focused ultrasound with dual single-element transducers in beam profiles, including the volume of full width at half maximum, and axial and lateral directions of the focal area, were investigated. Fourthly, the influence of the skull effects, including the different transducer placements on the head and differences between 0.35 MHz and 0.5 MHz acoustic frequency for both female and male models, was studied. The outcomes of this study suggest that a suitable combination of transducer size, location, and power level can achieve the most promising performance based on location in the brain. In addition, the numerical studies in this project provide a valuable method for highly detailed and specific non-invasive brain stimulation using focused ultrasound stimulation, which could be further explored and utilized in future research applications and clinical practices.

CERTIFICATION OF THESIS

I Yi Huang declare that the PhD Thesis entitled Modelling and Numerical Investigations of Transcranial Focused Ultrasound Stimulation is not more than 100,000 words in length including quotes and exclusive of tables, figures, appendices, bibliography, references, and footnotes. The thesis contains no material that has been submitted previously, in whole or in part, for the award of any other academic degree or diploma. Except where otherwise indicated, this thesis is my own work.

Date: 15/November/2022

Endorsed by:

Prof. Paul (Peng) Wen
Principal Supervisor

Prof. Yan Li
Associate Supervisor

Dr. Bo Song
Associate Supervisor

Student and supervisors' signatures of endorsement are held at the University.

ACKNOWLEDGEMENTS

This thesis has been made possible by the generous help and support given by my principal supervisor, Professor Paul (Peng) Wen, and associate supervisors, Professor Yan Li and Dr Bo Song. I would like to take this opportunity to express my sincere gratitude to this supervising team. Thanks for sharing all the valuable research skills and knowledge with me along the way.

No funding means no fun! I am extremely thankful to the University of Southern Queensland (UniSQ) for providing scholarships to support my PhD program. I am grateful to the sponsors as I would not be able to complete my studies at the UniSQ without their financial support. Also, I would like to express my gratitude to the supporting staffs at School of Engineering.

A big thank you to my friends and co-works from the Faculty of Health, Engineering and Sciences; in particular, Xing Chen, Mingkan Shen, Xiaopeng Ji and Wei Pei are acknowledged. Thanks for sharing all the valuable things in these four years. I learned so much from you guys, and this will be the everlasting memory of my life.

To my wonderful parents, thank you for supporting and encouraging me to pursue my PhD in Australia. Sometimes I feel guilty being apart from you for so many years since I came to Australia in 2016. I hope the achievements I made in these years bring you happiness and joy. I love you all from the bottom of my heart. My family and the good people from Wuhan mean a lot to me – they are like a backup dispatchable power source easing my mind of variability. Seeing my family cheering me on from my side is a feeling I will cherish forever.

Finally, my deepest gratitude goes to my beloved wife, Hui Liang, who has lived through every minute with me. You have been incredibly patient with me, and I owe you the deepest apology whenever I became unreasonable and fragile. You are the reason that I am so complete and blessed right now. You are the butter to my bread and the breath of my life. Also, I would like to thank our son, Marcus Jinyi Huang, who is always eager to explore new places and create wonderful memories along the way.

DEDICATION

To Hui Liang

For her advice, her patience, and her faith,
Because she always understood.

TABLE OF CONTENTS

LIST OF ABBREVIATIONS

AIUM	the American Institute of Ultrasound in Medicine
APs	Action Potentials
ARF	Acoustic radiation force
BBB	Blood-Brain Barrier
CEUS	Contrast-enhanced Ultrasound
CFL	Courant-Friedrichs-Lewy
CI	Cavitation Index
CNS	Central Nervous System
CSF	Cerebrospinal Fluid
CT	Computerised Tomography
DBS	Deep Brain Stimulation
DCS	Direct Current Stimulation
DPC	Distance-based Phase Corrections
DSET	Dual Single-element Transducers
ECoG	Electrocorticogram
EEG	Electroencephalography
EM	Electromagnetic
FDA	The Food and Drug Administration
FDTD	Finite-Difference Time-Domain
FEM	Finite Elements Methods
fMRI	Functional Magnetic Resonance Imaging
FSL	FMRIB's Software Library
FWHM	Full Width at Half Maximum
FUS	Focused Ultrasound Stimulation
GM	Grey Matter
GPU	Graphic Processor Unit
HIFU	High-intensity Focused Ultrasound
LAPWE	The Linear Acoustic Pressure Wave Equation
LIFU	Low-intensity Focused Ultrasound
MI	Mechanical Index

MRI	Magnetic Resonance Imaging
MR	Magnetic resonance
MST	Magnetic Seizure Therapy
NEMA	the National Electrical Manufacturers Association
NHP	Non-Human-Primate
PBE	Pennes' bioheat equation
PML	Perfectly Matched Layer
PNS	Peripheral Nervous System
PRF	Pulse Repletion Frequency
ROI	Regions of Interest
rTMS	Repetitive Transcranial Magnetic Stimulation
SEFT	Single-element Focused Transducers
SPC	Simulation-based Phase Corrections
STN	Subthalamic Nucleus
TES	Transcranial Electrical Stimulation
tDCS	Transcranial Direct Current Stimulation
tFUS	Transcranial Focused Ultrasound Stimulation
TMS	Transcranial Magnetic Stimulation
TI	Thermal Index
VHP	Visible Human Project
WLE	Westervelt-Lighthill Equation
WM	White Matter

LIST OF TABLES

LIST OF FIGURES

CHAPTER 1: INTRODUCTION

Brain stimulation techniques, such as direct current stimulation (DCS) and transcranial magnetic stimulation (TMS), as non-invasive methods, are typically used to modulate brain functions. These brain stimulation modalities contribute to a more profound understanding of brain activities by stimulating the specific brain tissues or neural substrates for neuromodulation. However, the electromagnetic modalities of brain stimulation are limited by penetration depth (in the case of TMS) and spatial specificity (in the case of DCS) [1]. Deep brain stimulation can achieve high spatial resolution as an electrode is placed inside the brain to deliver electrical impulses and signals to a specific brain region for invasive stimulation [2]. Also, recent developments in the optogenetic brain stimulation method demonstrate higher spatial resolution; however, the invasive procedures require cell-level intervention [3]. Thus, the high demand for brain stimulation techniques with penetration depth, higher spatial resolution, and a non-invasive method is warranted. As a non-invasive brain stimulation modality, focused ultrasound uses single or multiple acoustic transducers to deliver highly-localized acoustic energy to a specific target region in the brain [4, 5]. Compared with the diagnostic imaging ultrasound modality (frequency between 1-15 MHz), a lower acoustic frequency (<1 MHz) in focused ultrasound stimulation allows acoustic waves to propagate through the intact skull and form a focal spot area in the brain [6]. These characteristics of focused ultrasound have distinct advantages over other modalities of brain stimulation, which provide higher spatial resolutions in a focal manner (on the order of a few millimetres) across the brain and superior penetration depth without invasive clinical procedures.

1.1 Transcranial focused ultrasound stimulation

Focused ultrasound stimulation (FUS) is a promising alternative to pre-clinical and clinical trials as the mechanical and thermal effects can be induced to intervene in neuromodulation for various brain conditions non-invasively. The ability of FUS for neuromodulation was first proposed by Fry et al. in their pioneering work in 1958 [7]. They used ultrasound to irradiate the lateral geniculate nuclei of the thalamus and induced temporary potential suppression of the visual cortex in cats. Later, the potential change monitored using electroencephalography (EEG) in cats by Manlapaz et al. was demonstrated with the suppression of seizure activity [8]. Furthermore, the ability of Transcranial Focused Ultrasound Stimulation (tFUS) was proven to enhance and suppress electrically-evoked neural field potentials by stimulating rodent hippocampal tissues [9]. In recent years, several studies have proved that tFUS induces excitatory and suppressive effects on neuromodulation not only for the central nervous system (CNS) but also for the peripheral nervous system (PNS) [10, 11]. In addition, short bursts of ultrasound pulses were applied in tFUS for modulating neural activity [12, 13]. These studies demonstrated that a wide range of pulsing schemes, such as frequency, pulse repletion frequency, pulse intensity, sonication time, and duty cycle, might induce different effects on the focal spot displacement magnitude in acoustic neuromodulation. Meanwhile, continuous ultrasound waves also demonstrated the ability to modulate the brain's neural activities [14].

The principal attraction of treatment applied by FUS is to exert biological effects induced by acoustic waves through the intact skull. Compared with the non-invasive FUS modality, invasive brain stimulation modalities have higher surgical risks in tissue trauma, inflammation, and pain treatment [15]. However, bone, as the main barrier for acoustic wave propagation, strongly attenuates and reflects ultrasound, which results in distortion of targeting efficiency. Also, the skull's density, structure, and thickness vary

between individuals [16]. In the past two decades, several technological developments have accelerated research activities in the field of FUS. Multiple acoustic transducers (phased array transducers) and real-time magnetic resonance imaging (MRI) thermometry monitoring techniques implemented in FUS applications make it feasible in clinical surgery. The computer-assisted transducer design, including the phase and amplitude of piezoelectrical elements, can correct the ultrasonic aberrations while acoustic waves propagate through the skull for specific subject adjustments [6]. The specific adjustments are induced by CT scans of the skull and numerical acoustic modellings [6, 17]. Magnetic resonance (MR) coupling provides real-time information about the lesion and temperature changes during sonication, which might overcome technical limitations, such as stereotactic radiosurgery [18]. In some low-intensity focused ultrasound (LIFU) applications, a single-element transducer, as a cost-effective alternative approach, is used for lens-based aberration correction and directly placed on the specific region of the scalp [19]. Though phased array transducers and lens-based single-element transducers are utilized for acoustic wave aberration, reliable and highly detailed 3D human head models are still desired in numerical modelling. Also, brain tissues (e.g., skull, cerebrospinal fluid (CSF), grey matter (GM), white matter (WM), blood, muscles) properties, such as material attenuation, density, and acoustic impedance, vary between individuals. Therefore, the construction of high-resolution human head models with increasing model complexities is expected to address acoustic wave propagation precisely and investigate the acoustic wave effects on homogeneous and heterogeneous brain tissues. Furthermore, compared with the phased array transducer, single-element transducers have the poorer spatial resolution at the focal spot area, especially in the axial direction. It is still challenging to explore FUS neuromodulation with low cost, better accessibility, and higher spatial resolutions. Therefore, the highly detailed human head model is desired to be utilized for precision applications of tFUS. Also, energy deposition, temperature changes, and higher spatial resolutions in the brain are

increasing and need to be addressed. Those attempts demonstrate promising and meaningful research applications and clinical practices in tFUS studies.

1.2 Research objectives and strategies

The focus of this project is to numerically investigate the mechanical effects of acoustic wave propagation through detailed human head models. The major objectives of this project are listed as follows:

The first objective is to numerically investigate the ultrasound wave propagation and the energy distribution within the brain tissues using customised single-element focused ultrasound transducers (SEFT) targeting the hippocampus.

The second objective is to investigate the effects of ultrasound beam on FUS-mediated Blood-Brain Barrier (BBB) opening. The mechanical index (MI) and cavitation index (CI), as two metrics that reflect ultrasound-induced BBB disruption, are used to analyse the intracranial field changes.

The third objective is to computationally investigate the effect of LIFU spatial resolution with dual single-element transducers (DSET) in beam profiles, including ultrasonic energy change, the volume of full width at half maximum (FWHM), and axial and lateral directions of the focal area.

The fourth objective is to evaluate the skull effects of acoustic wave propagation. The detailed human skull models are constructed using medical images, and the linear and non-linear wave propagation models are used to simulate in the water tank as a baseline computational case. The frequency, placements of transducers, and skull morphology are investigated for the intracranial intensity distribution, pressure, and FWHM volumes.

Computational models are essential for predicting and compensating for the acoustic wave distorting effects of the complex, inhomogeneous brain structure. A 3D realistic human head model frame is constructed using commercial packages, and a series of human head models is developed. Acoustic full-wave 3D models based on the finite-difference time-domain (FDTD) method are used for the computational modelling of acoustic wave propagation. First, a spherical single-element ultrasound transducer is built to conduct acoustic wave transmission modelling in a water tank, and the purpose is to validate the numerical results with peers' studies. Later, the customised ultrasound transducers are used to induce acoustic energy deposition in the human head model. The influence of transducers' placement, homogeneous and heterogeneous brain tissues, and the tissue properties of the skull have been examined to derive how acoustic energy deposition changes in specific brain tissue. Then, the MI and the CI are characterised to evaluate the BBB opening, and the role of incidence acoustic wave angles, operating frequency, and complexity of the skull have also been explored. Due to the ability of transcranial focused ultrasound stimulation to deliver a focal spot in the deeper brain tissues, DSETs are applied to investigate the spatial resolution at the focal area.

1.3 Research outcomes

In this project, a high-resolution detailed human head model with seven tissue types was constructed from MRI. Meanwhile, the two detailed human skull models have been constructed from computerised tomography (CT) images. A full-wave FDTD simulation platform, Sim4life, was then used to simulate a 3D non-linear ultrasound wave equation to the specific deep brain regions. In the application of acoustic neuromodulation, ultrasound energy deposition, the ultrasound spatial resolutions, the performance of FUS-mediated BBB opening, and skull effects between individuals on intracranial intensity and pressure maps were investigated.

Firstly, in the study of energy deposition in the deep brain tissue induced by focused ultrasound, an optimised application of a SEFT was customised to deliver 100 W/m^2 intensity of energy deposition in the hippocampus region. About 85.65% of the generated volume beam was delivered to the targeted hippocampus region, and the beam overlap parameter was affected by different transducer positions. Deflection angle changes of SEFT at the range of ±5% did not have a significant effect on energy delivery and position displacement. Only 0.5% of peak pressure change was observed between heterogeneous and homogeneous brain models. The sensitivity analysis also showed that sound speed is the most influential acoustic parameter.

Secondly, in the study of focused ultrasound-mediated BBB opening, a 3D non-linear ultrasound wave equation to the specific region of interest, the putamen and caudate was simulated. MI, CI, the volume of FWHM, percentage of beam overlap and target overlap were applied as parameters related to the performance of FUS-mediated BBB opening. In addition, the impact of centre frequency, the skull, and incidence angles of ultrasound wave propagation were assessed. The results show that MI and CI are relatively less sensitive to variations at the lower centre frequency (0.35 MHz) than those at the higher frequency (0.5 MHz). Also, MI and CI are most dramatically affected by changes in attenuation and sound speed, while only a minor effect on MI and CI (within $\pm$5%) is caused by changes in density. In the sensitivity analysis of the skull effect, changes in the sound speed of the skull have a greater effect on the volume interaction between target regions and focal spots than density and attenuation. The incidence angle analysis also indicates that greater deflection angles (at 7° and 10°) lead to a greater percentage change of focal spots and correspond to the target overlap and beam overlap than deflection angles at 3° and 5°.

Thirdly, the role of spatial resolutions induced by focused ultrasound in the deep brain regions was investigated. This study was to study the ultrasonic wave propagation through a 3D highly detailed human head model and computationally investigate the effect of LIFU with DSET in beam profiles, including ultrasonic energy change, the volume of FWHM, axial and lateral directions of the focal area. The results showed that dual transducers have superior target spatial resolution over SEFT. The focal diameter in the axial direction is around 7 mm at 80° crossing angle, which is around 5.5 times the improvement in the axial resolution compared with SEFT when the frequency is at 0.5 MHz. Moreover, the case of crossing angle at 80° has the highest axial resolution and robustness to phase difference in terms of FWHM volume and maximum intensity of side lobes. The higher frequency (0.65 MHz) has a better spatial resolution than lower frequencies (0.35 MHz and 0.5 MHz) in axial and later directions, but it has poor resolution in FWHM volume due to the presence of side lobes.

Fourthly, the skull as the primary barrier of transcranial focused ultrasound propagation was investigated. The two detailed human skull models were constructed from the CT images, and the acoustic properties were calculated. Validation of the linear and non-linear models was conducted in a water tank, and no significant difference was observed for peak intensity, pressure, and FWHM volumes. The ultrasound frequency takes into consideration of the skull effects, as the intracranial intensity, pressure, and FWHM volumes experienced greater changes when the frequency was at 0.35 MHz compared to the frequency at 0.5 MHz in the relatively smaller geometry of the female skull than the male skull.

1.4 Dissertation outline

This dissertation consists of eight chapters. The first three chapters provide the research background, a comprehensive literature review of the research, and the methodology applied. Chapters 4 to 7 illustrate the work of the

model design, simulation development, implementation, and evaluation. The conclusions are drawn in Chapter 8.

Chapter 2 focuses on a literature review of focused ultrasound technology and its applications in human brain research. Firstly, the basic theory of focused ultrasound and transducers is introduced. A comprehensive literature review and comparison between ultrasound stimulation and other brain stimulation techniques, such as DCS, deep brain stimulation (DBS), and TMS, are conducted. In addition, the applications of focused ultrasound, such as neuromodulation and BBB disruption, are briefly introduced.

Chapter 3 describes the numerical modelling and framework. It starts with computational motivation and a detailed human head model. This chapter provides the details of the computational framework from acoustic full-wave models, FDTD method, thermal modelling, and boundary conditions, which describes how acoustic wave propagation is proposed as one of the most fundamental methodologies in this project; the basic computational setting are presented. Furthermore, the limitations of computational modelling have also been discussed.

Chapter 4 explores the ultrasound wave propagation and the energy distribution within the brain tissues using customised SEFT, targeting the hippocampus. In this chapter, a high-resolution, detailed human head model with seven tissue types was constructed from MRI. A full-wave FDTD simulation platform, Sim4life, was then used to simulate a 3D non-linear ultrasound wave equation for the specific region of interest, the hippocampus. Three customised SEFTs were used to test the effect of transducer positions, and another customised transducer was used to compare the sensitivity effect on heterogeneous and homogeneous brain models. Finally, the sensitivity and performance of LIFU stimulation were evaluated.

Chapter 5 investigates the feasibility of transcranial focused ultrasound with microbubble-inducing BBB opening in targeted areas and facilitates drug delivery. In this chapter, a 3D non-linear ultrasound wave equation was used to simulate acoustic wave propagation to the specific region of interest, the putamen and caudate. MI, CI, the volume of FWHM intensity, percentage of beam overlap, and target overlap were applied as parameters related to the performance of FUS-mediated BBB opening. In addition, the impact of centre frequency, the skull, and incidence angles of ultrasound wave propagation to the intracranial fields were assessed.

Chapter 6 studies the spatial resolutions at the focal spot area induced by acoustic waves in the deep brain region. This chapter computationally investigates the effect of LIFU with DSET in beam profiles, including ultrasonic energy change, the volume of FWHM, and axial and lateral directions of the focal area. The impact of operating frequency, phase difference, and DSET with different cross angles was investigated through the focal area and corresponding FWHM focal volume.

Chapter 7 investigates the influence of the skull in the intracranial intensity distribution, pressure maps, FWHM volumes, and energy deposition. The details of the two skull models are constructed using medical images. Then, the medical images are used to convert them into maps of acoustic properties. Two different types of ultrasound transducers, including single-element focused ultrasound and multiple-elements transducer, are proposed to compare the influence of intracranial intensity distribution and focal spot region. The placement of transducers, such as the temporal window, is also evaluated.

Chapter 8 summarizes and concludes all the work conducted in this project. Results, outcomes, and major contributions in this study are presented. Limitations in this study are also discussed. At last, the future research directions of tFUS combined with multi-physical modalities are suggested.

CHAPTER 2: LITERATURE REVIEW

This chapter provides an overview of focused ultrasound technology, including ultrasonic transducers and different brain stimulation modalities. Also, the applications of focused ultrasound, such as ultrasound neuromodulation and BBB disruption, are reviewed. Firstly, we introduce the different types of ultrasound transducers and their applications in clinical and pre-clinical trials. Then, brain stimulation techniques, divided into electromagnetic stimulation and transcranial focused ultrasound stimulation, are explained. We continue by discussing focused ultrasound stimulation for different applications.

2.1 Focused ultrasound

Ultrasound waves are generated by high-frequency mechanical vibrations (frequency 20 kHz–10 GHz), which are employed by several techniques. Transcranial focused ultrasound technique produces an acoustic wave, and the mechanism phenomenon is called the piezoelectric effect. This phenomenon refers to the conversion of mechanical energy and electrical energy. When the crystals inside an ultrasound transducer are applied by the electric current, the crystals contract or expand while the electric current travels in. The occurring contraction or expansion of crystals leads to the vibration, and acoustic energy is generated when the vibration is taking place.

The piezoelectric effect has two ways of converting electrical energy and mechanical energy (seen in Figure 2-1). The direct piezoelectric effect involves the conversion of mechanical energy into electrical energy. Piezoelectric material is compressed or squeezed to generate piezoelectricity, and the voltage is linearly proportional to the material deformation. Also, the polarity of the voltage is associated with the direction of the deformation. A voltage is of the same polarity when the

direction of squeezing along the polarization axis or tension is perpendicular to that axis and vice versa. The converse piezoelectric effect involves the conversion of electric energy into mechanical energy. The element tends to stretch if the same polarity voltage is applied to the piezoelectric elements. Alternatively, a voltage of opposite polarity leads to the element being shrunk.

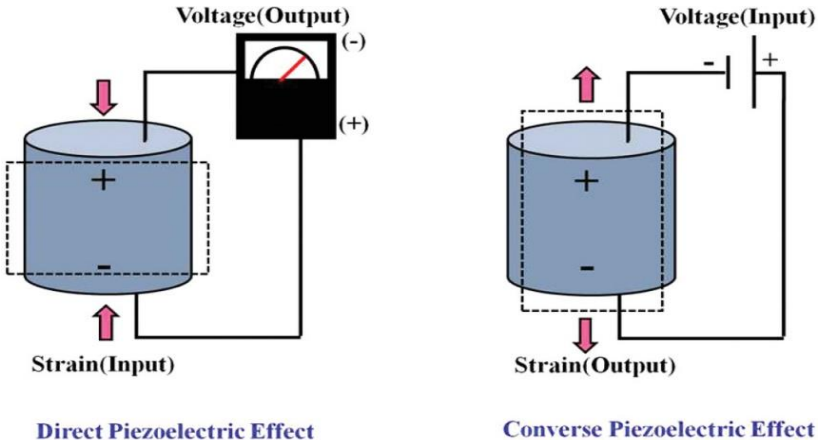

Figure 2-1 Direct and inverse piezoelectric effect [20]

Direct and inverse/converse piezoelectric effects can also be observed when mechanical or electrical voltage changes are alternated in the time domain. Mechanical waves are generated when alternating current yields the compression or tension of the piezoelectric elements, and alternating deformation of the piezoelectric elements yields the voltage change. Figure 2-2 demonstrates the example of acoustic wave transmission. Ultrasound waves can be generated and detected by ultrasonic transducers because of the property of piezoelectric materials.

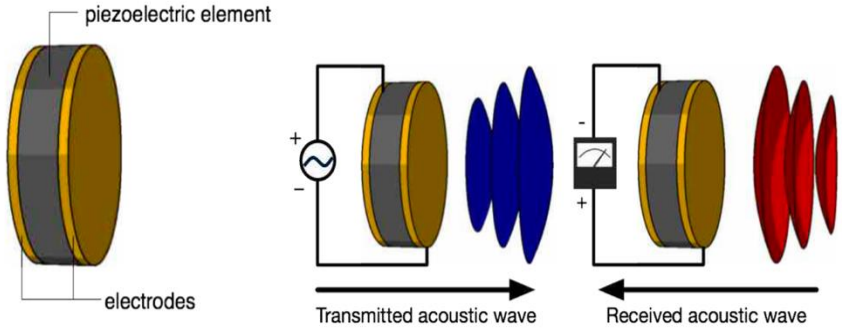

Figure 2-2 Generation and detection of ultrasound waves [21]

2.2 Ultrasonic transducers

Piezoelectric transducers can be machined into different sizes and shapes. Commonly focused ultrasound transducers are single-element focused transducers and multi-array ultrasound transducers, depending on the number of piezoelectric elements. Piezoelectric elements permit the conversion between acoustic energy and electricity. The appropriated dimension of the elements plays a vital role in generating a specific acoustic wave in medical applications.

2.2.1 Single-element ultrasound transducer

SEFT naturally generates an ultrasonic field with a focus spot area using a single piezoelectric element as a sphere or hollow shape (see Figure 2-3 and Figure 2-5), and these types of SEFT are referred to as spherically focused transducers and cylindrically focused transducers. Because of the different shapes of the transducers, the beams of the focal spot area are different.

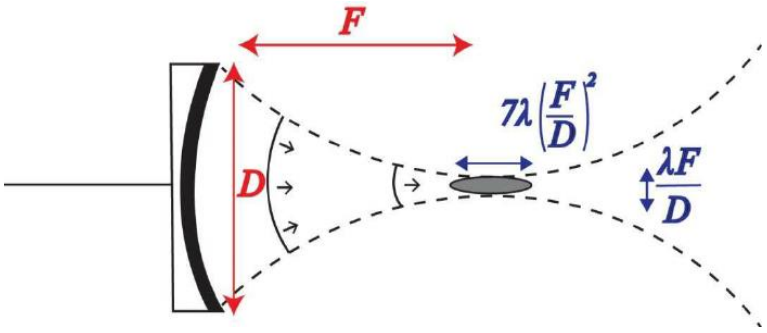

Figure 2-3 A spherically focused transducer [22]

2.2.1.1 A spherically focused transducer

The characteristic of spherically focused transducers is to generate a focal spot area with a spherical shape and then diverge again as the acoustic waves continue to propagate in the medium (see Figure 2-4 (a)). The geometric focus point of a spherically focused transducer lies at the centre of the piezoelectric element. The shape and size of the focal spot area, which is converged by the ultrasound beam, depends on the geometry of the transducer, such as curvature radius R and diameter d (see Figure 2-4

(b)). Generally, the F-number, which is the ratio of R and d ($F = \frac{R}{d}$), is used to describe the geometrical focusing [23]. Obviously, the distance between the focal point and the transducer will be greater when increasing the curvature radius and vice versa.

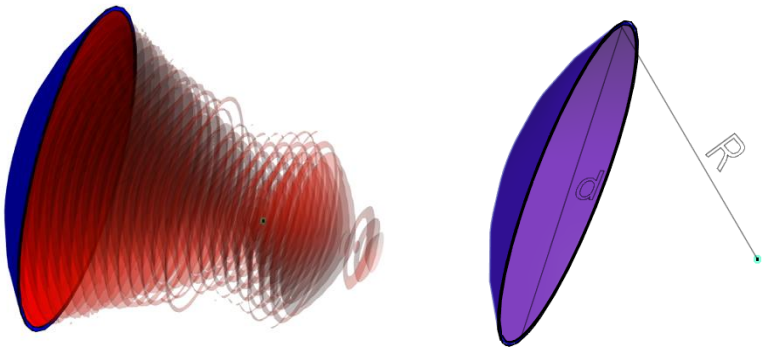

(a) (b)

Figure 2-4 (a) Ultrasonic wave propagation (b) Illustration of a spherically focused transducer

2.2.1.2 Acylindrically focused transducer

The shape of the focal spot generated by spherically focused transducers is a narrow ellipsoid, as displayed in Figure 2-3. However, the property of the focal spot is a continuous line when applied to cylindrically focused transducers (

see Figure 2-5), and this type of transducer is also known as a line-focused transducer. As with spherically focused transducers, the dimensions of the focal spot depend on the F-number of transducers, defined as the focal length divided by the aperture of the beam [23]. The larger the transducer's diameter used, the smaller the dimension of the focal spot produced. At the same time, the size of the focus spot area is proportional to the acoustic wavelength and the transducer's F-number. The convergence of beams at the focal spot area has a far higher pressure and intensity than the pressure and intensity at the near face of the transducer, and focal gain is used to describe the ratio of these two properties. Thus, the non-thermal and

thermal effects will be induced by acoustic waves when the ultrasound propagates through the brain without causing any side effects on the overlaying tissues.

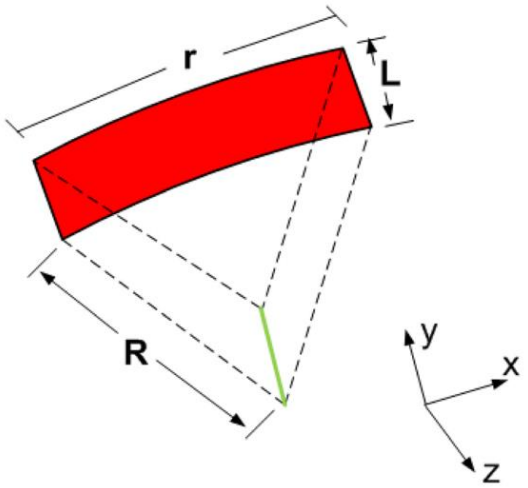

Figure 2-5 A cylindrically focused transducer [24], The parameter R is the radius of curvature of the transducer, r is the aperture size or width, and Lis the length of the transducer

2.2.2 Ultrasonic transducer arrays

Compared with ultrasound transducer arrays, the hardware demand for the SEFTs is relatively low; the cost is much lower, and a simple driving system is required in the ultrasound application. In a transcranial focused ultrasound case, assuming the acoustic waves propagate in a homogeneous medium, the ultrasound beam is formed at a given location. However, moving the focal spot is required to induce the thermal or non-thermal effect in a larger tissue region in medical applications. 3D translation devices are utilized to move transducers mechanically in the case of SEFTs, as these kinds of devices are inaccurate to move and inflexible to operate. Furthermore, the brain tissues are highly heterogeneous structures, especially in the skull. The skull has a higher density and sound speed, which might induce a mismatch of impedance.

Transducer arrays are assemblies of multiple piezoelectric elements, referred to as multi-element arrays or phased arrays, which can be used as an alternative to SEFTs. Transducer arrays have as many as 16 to hundreds of individual piezoelectric elements, and each element has its own driving

system. Thus, the transducer arrays can be controlled by a computer in real-time and exhibit desired frequencies. In this way, a delay between each piezoelectric element stimulus can be introduced, which can be directly controlled by the driving system via computer. This characteristic of transducer arrays enables them to generate different patterns of acoustic waves, and the convergent beam will have many different combinations. Thus, transducer arrays exhibit different shapes and sizes of focal spot areas than SEFTs. However, the disadvantages of transducer arrays are higher costs and complicated operations. Figure 2-6 demonstrates that the transducer arrays generate numerous focal points, hence treating large regions at the desired position. Also, focal steering can be achieved by correcting beam aberrations to converge a focal spot at a millimetre.

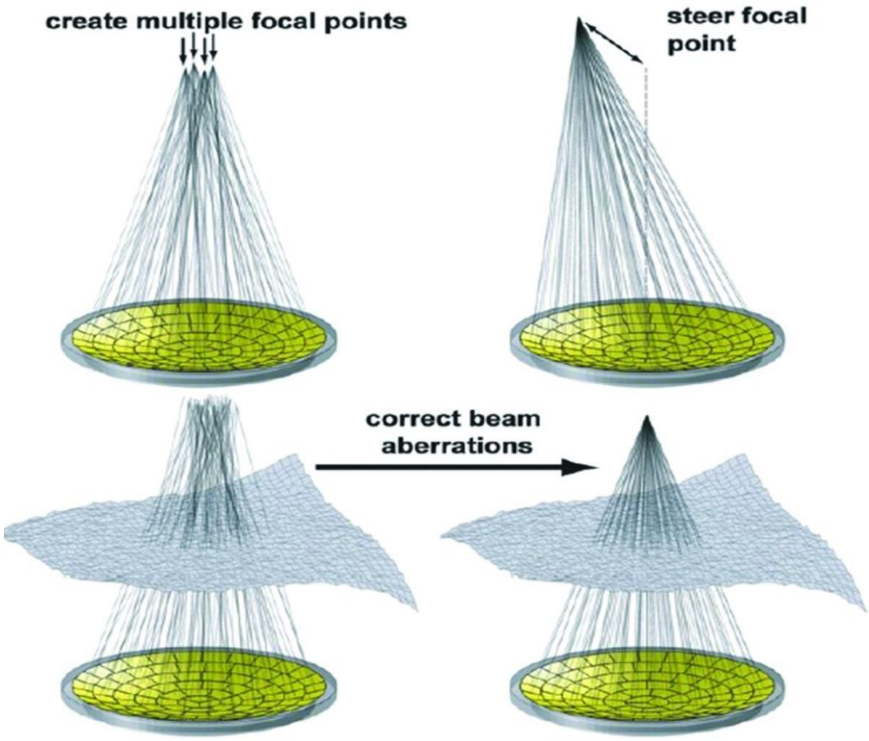

Figure 2-6 Multi-element transducer with multiple focal points and a steer focal point [25]

2.3 Brain stimulation

Electromagnetic and acoustic brain stimulation are applied in a wide range of research and therapeutic applications. Therefore, the brain stimulation techniques are divided into two categories, electromagnetic stimulation

(including direct current stimulation, deep brain stimulation, and transcranial magnetic stimulation) and ultrasound stimulation. This section aims to provide some background information about different brain stimulation types and an overview of the applications of brain stimulation techniques.

2.3.1 Electromagnetic stimulation

Electromagnetic (EM) brain stimulation refers to excitation, regulation, inhibition, or other effects on the brain tissues or nervous system using electric or magnetic fields. The technique of EM brain stimulation has been demonstrated to be of great value in medical treatment, particularly in the approaches for which pharmacology is not suitable. Besides, brain neuromodulation using the EM technique has been successfully applied in therapeutical applications, such as epilepsy, Parkinson's disease, essential tremors, depression, and motor rehabilitation [26-28]. The basis of EM stimulation is to induce a magnetic field or electric field source outside (non-invasive) or inside (invasive) the body. A time-varying current induces currents and electric changes in the biological tissues to generate magnetic fields. Also, electrodes are used to direct contact with the body to induce electric fields.

There are several different modalities of EM stimulation, such as DCS, transcranial direct current stimulation (tDCS), DBS, and TMS. Non-invasive EM brain stimulation employs a pair or array of electrodes placed on the scalp using direct or alternating currents [29]. The invasive EM modality utilizes implanted electrodes to do the brain stimulation. The implanted electrodes are typically placed near target regions deeper inside the brain, depending on the treatment requirements and neurological conditions [30].

2.3.1.1 Direct current stimulation

During the past decade, transcranial direct current stimulation has been applied in numerous trials across a variety of neurological and psychiatric conditions, such as medication-resistant depression, brain tumours, and Parkinson's disease [31]. Transcranial direct current stimulation, as a non-invasive neuromodulation technique, delivers low-amplitude direct current via anode and cathode electrodes, which are attached to the distinct area over the scalp. The anode electrode is attached over the head for excitation, and the cathode over the regions for hyperpolarization (see Figure 2-7). The current penetrates the skull from the anode electrode, travels via brain tissues, and exists at the cathode electrode [32]. The current and the placement of electrodes depend on the number of electrodes and stimulation protocols [33]. Also, the short and long durations of the tDCS have different effects on regional and local areas [34]. Compared with tFUS, the electrodes are relatively large, and the stimulation area cannot be focused on a higher spatial resolution. Also, the study of tDCS is generally restricted to the brain cortex stimulation due to field strength dropping as quickly as increasing the distance. Meanwhile, tDCS differs from other brain stimulation modalities, such as TMS and transcranial electrical stimulation (TES), as tDCS modulates spontaneous neuronal network activity rather than inducing neuronal firing by modulating membrane depolarization [35].

The treatment in tDCS needs to be tailored or at least be informed by the patient's brain anatomy, as the brain tissues have great interpersonal differences that might have influenced the ability of penetration of stimulation. Thus, computational modelling plays an important role in the pre-clinical steps to improve the success of target stimulation. While it is difficult to understand the precise mechanism of tDCS, some experiments and numerical modelling works have been done to explore the neuroplasticity in the human motor cortex [36]. The tDCS is relatively portable and low-cost, can be placed bilaterally, and has a painless and safe profile.

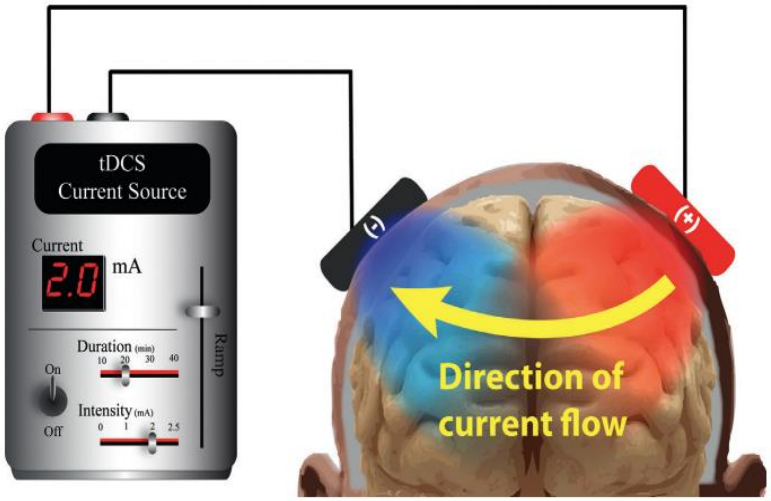

Figure 2-7 Illustrations of a tDCS system [37]

2.3.1.2 Deep brain stimulation

Deep brain stimulation is an important modality in the application of EM stimulation, as the DBS technique is applied for therapeutics such as chronic pain and movement disorders [38]. DBS is an invasive brain stimulation modality, and an electrode is implanted into the deep of the brain, which is placed near the targeted cerebral structure, such as the subthalamic nucleus (STN), involved in the neurological diseases (STN-DBS on cognition in Parkinson's disease) [2].

The shaping of the stimulation field depends on the polarity configuration and electrode design. Also, the characteristics of the stimulation, such as amplitude, rate, and frequency, affect the stimulation field. Furthermore, interleaving DBS enables improved treatment outcomes [39]. Thus, the detailed brain anatomical structures and a well-shaped stimulation field play a vital role in achieving the desired therapeutic performance and avoiding undesired side effects. Numerical modelling as an efficient method can optimise these procedures using the computational DSB system. Figure 2-8 demonstrates the concept of DBS.

The stimulus safety and efficacy are important factors in the stimulator design of DBS applications. Charge injection is used as a safety metric in DBS clinical trials [40, 41]. Some factors, such as electrode type, dielectric properties, and brain anatomy, may affect the charge injection. Also, neuron activation in the DBS is related to the charge injected, and electrochemical reactions are related to charge density, which occurs at the interface between electrode and tissue [42]. Thus, the impedance of the interface, brain tissue heterogeneity, and stimulation field should be considered before clinical trials. Computational modelling as an efficient method positively quantifies the accurate charge injection and investigates the effect of parameter setting. Numerical models of brain neuromodulation using DBS techniques have been useful in different neural targets in Parkinson's disease and tissue activation [43].

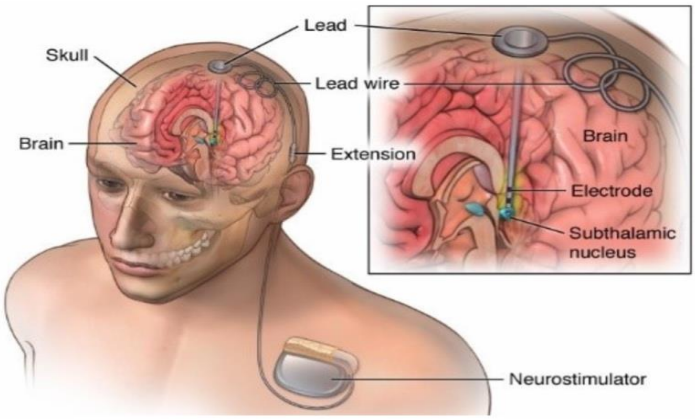

Figure 2-8 Concept of deep brain stimulation (DBS) [44]

2.3.1.3 Transcranial magnetic stimulation

The effect of TMS is similar to that of the tDCS neuromodulation modality. For TMS, a coil of wire referred to as the magnetic coil (see Figure 2-9 (a)) is used to produce a high-current pulse. The plane of the coil is typically placed tangential to the scalp, and the magnetic fields are induced by lines of flux perpendicular to the coil (see Figure 2-9 (a)). Meanwhile, a time-varying magnetic field is induced perpendicularly to the electric field. There are different shapes of magnetic coils in the application of TMS. Compared with the round coils (see Figure 2-9 (b) A), figure-of-eight-shaped coils (see Figure 2-9 (b) B) produce the current focally, and the maximum current is

induced at the intersection position of the two round coils. Also, there are other shapes of coils, such as double-cone coils, H-coils, and magnetic seizure therapy (MST) coils. The different types of coils determine the volume of the stimulus target, and the stimulus amplitudes affect the activation of the target volume as well [45].

Monophasic and biphasic waveforms are two common stimulation pulse waveforms for TMS. A biphasic pulse waveform as a standard waveform is used for delivering repetitive TMS (rTMS) when a lower energy requirement is applied [46]. However, compared with biphasic pulse waveforms, monophasic pulse waveforms have an advantage in sustained after-effects, as biphasic pulse waveforms induce complex neural activation in rTMS protocol [46]. Fregni et al. investigated a meta-analysis of 12 studies and demonstrated that rTMS has a positive effect on motor function in Parkinson's disease [47]. Also, the technique of rTMS has been applied for the treatment of medication-resistant depression, strokes, and Alzheimer's disease [48, 49]. However, the inter-individual variability of the modulatory effects is large, and inverse responses are observed in some excitation cases when they are expected to be inhibited [50]. Thus, computational models as an efficient approach could help investigate and study the different situations before clinical trials.

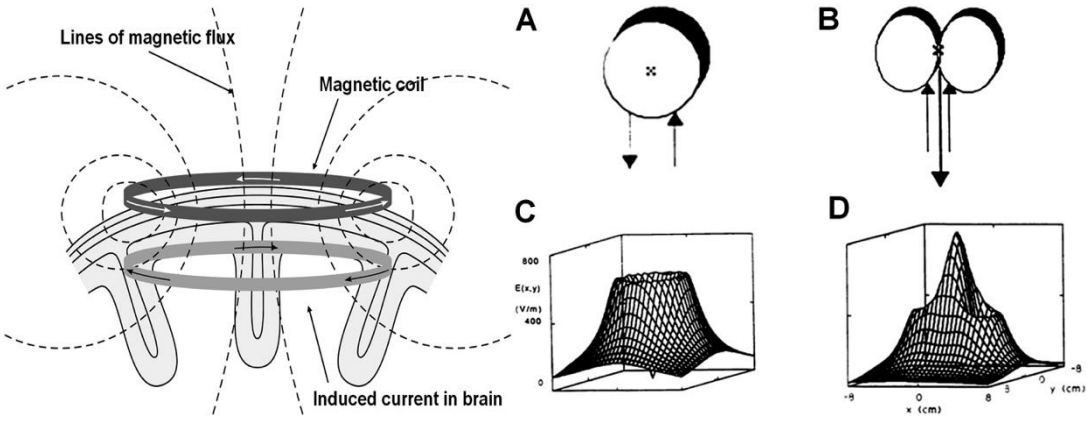

(a) (b)

Figure 2-9 (a) Illustration of transcranial magnetic stimulation with current flows (b) Placement of the magnetic coil [51].

2.3.2 Transcranial focused ultrasound stimulation

The tFUS, as a new modality of brain stimulation, induces activation, inhibition, and synchronization of neurons through acoustic waves. Compared with other modalities of brain stimulations, acoustic transducers do not excite neurons directly, as the active area of acoustic mechanisms is used for acoustic neuromodulation. Compared with the EM brain stimulation technique, tFUS as a new stimulation modality has yet to be translated into clinical practice. The disadvantages of non-invasive EM stimulation are difficulty localizing the target area and the limitation of stimulus depth in the brain. Besides, the surgery of invasive EM stimulation of a deeper target area needs further steps in steering techniques. However, ultrasound, as a promising brain stimulation modality, is a non-invasive technique to stimulate deeper brain tissues, and the focal area can be millimetres sized. Also, the desired focal spot area can be formed without affecting tissues along the propagation.

In focused ultrasound brain stimulation, typically, an electrical waveform induced by a pulse generator is carried to a transducer, which is coupled with a piezoelectrical element. The electrical signals are excited by the piezoelectric element, and the element then oscillates on the surface of the transducer. Operating frequency, pulse intensity, sonication time, duty cycle, and pulse repletion frequency (PRF), are five key parameters defined in ultrasound sonication protocol. Slightly changing these parameters may lead to different effects on the focal spot displacement magnitude of neuromodulation [52, 53]. The operating frequency is the fundamental frequency emitted from transducers, and it is defined as the total oscillatory cycles in a unit of time. The transducer's operating frequency is related to the spatial resolution of the focal spot area in the brain target. It is known that the ultrasound frequency is proportional to the wavelength inversely. Thus, a higher operating frequency will have a tighter and narrower focal spot area than a lower operating frequency, and the spatial resolution can

be achieved in a few millimetres when the frequency is above 1 MHz [6, 54]. The PRF parameter determines the acoustic pulse rate in the ultrasound propagation, and the duty cycle is defined as the proportion of total cycles in each pulse. Compared with the continuous sonication modality, the pulse wave stimulation modality has a lower risk of thermal effect and neural activation [55, 56]. Sonication duration is the total time from the first to the last pulse, and sonication duration may lead to different effects in pre-clinical neuromodulation [57]. A needle hydrophone is typically used in clinical trials to measure power deposition in the brain, which is characterized as acoustic intensity [58]:

$$I = \frac{p^2}{2Z} = \frac{p^2}{2\rho c} \qquad \text{Equation 2-1}$$

where I is measured acoustic intensity, p is pressure, Z is impedance, ρ is density, and c is the sound speed in the medium. Also, acoustic intensity as a quantity metrics to investigate therapeutic effect and safety in tFUS.

tFUS delivers mechanical forces to the deep area in the brain, which induces bioeffects, such as thermal and mechanical effects, depending on the acoustic pulse regime [59]. Acoustic radiation force (ARF) and cavitation effect are two relevant mechanical effects in neuromodulation applications. The ARF generates a force on the tissue, which is induced by the attenuation that occurs in the tissue [60].

$$F_{ARF} = \frac{2\alpha I}{c} \qquad \text{Equation 2-2}$$

where α is the attenuation, I is the intensity, and c is the sound speed. Acoustic cavitation refers to the formation of bubbles is the tissue as the tensile phase over a threshold [61], and the threshold depends on operating frequency, total stimulus time, and pressure.

Fry et al. first used the focused ultrasound technique to conduct a therapeutic experiment for lesion thermal ablation in the 1950s [62]. They used high-intensity focused ultrasound (HIFU) to destroy a region of tissue in the mammalian central nervous system. This therapeutic modality has

been applied to treating brain cancers and brain disorders [63]. Additionally, therapeutic delivery of ultrasound using shorter pulse waves with contrast-enhanced ultrasound (CEUS), which involves intravenous contrast agents, opens the BBB via acoustic and mechanical mechanisms [64]. Thus, the focused therapeutic ultrasound with HIFU can be used for pharmacological neuromodulation applications targeting drug delivery to the brain [65]. In contrast, LIFU without therapeutic agents can directly apply to neurons neuromodulation [10, 56]. Consequently, tFUS, as a non-invasive brain stimulation method, has the potential to achieve deep brain targeting and spatial selectivity.

2.4 Applications of Focused Ultrasound

In the applications of focused ultrasound, multiple preclinical experiments, including immunohistochemistry, electrophysiological, in vivo calcium imaging, neuroimaging, and behavioural testing, have proven that low-intensity pulsed FUS can inhibit and stimulate neuronal activity in superficial and deep brain areas, respectively [66]. Meanwhile, BBB disruption is one of the most thoroughly researched FUS applications, with the safety and effectiveness of FUS BBB disruption proven in several preclinical and clinical investigations, including rodents, non-human primate models, as well as in human trials [67].

2.4.1 Ultrasound neuromodulation

2.4.1.1 Ultrasound neuromodulation in animals and human trials

Stimulation in animals

Ultrasound has been proven to induce excitatory and suppressive effects on CNS tissue, which depends on the pulsing regime of ultrasound. Fry et al. first observed partial suppression of the primary visual cortex of cats in 1958 [7]. Also, Ballantine et al. found that shorter pulsing waves enable suppressive effects on CNS [68]. On the other hand, Mazoue et al. observed that ultrasound was capable of exciting neuronal tissues with high

frequency ultrasonics [69]. Furthermore, several studies demonstrated that ultrasound induced temporally bioelectrical activities (evoked filed potentials) on the neural fibres [9, 70]. Neural activity was studied in subcortical and cortical regions of animals in ultrasound neuromodulation. The regions of the cortex, such as the caudate nucleus, hippocampus, and thalamus of rates regarded as stimulation target areas, were investigated to evoke potential changes related to depression [71]. Velling et al. investigated the functional state of the brain and demonstrated that bioelectrical activity occurs at lower stimulation intensity (1-100 mW/cm^2) and that higher intensity (1-100 W/cm^2) induces the amplitude of electrocorticogram (ECoG) to decrease [72]. A milestone work was published by Tyler et al. in 2008, and they showed the ability of ultrasound to induce action potentials (APs) in central neurons, which affected the flux of Ca^+ and Na^+ in CNS [10]. Subsequently, several in vivo research were conducted to investigate the excitatory and suppressive effects on various targeted brain tissues using different techniques, such as functional magnetic resonance imaging (fMRI), and electroencephalography (EEG). Different ultrasound parameter settings, also as a research direction, have been applied for eliciting motor responses in mice [52, 73] and rats [53, 57]. Furthermore, LIFU was employed to the depth of rats' brain tissue, the thalamus, which has the advantage of reducing recovery time from anaesthesia.

Studies in PNS applied ultrasound neuromodulation were conducted in parallel to the studies in CNS. Ultrasound stimulation on PNS induces excitation of spiking activity and then depresses spontaneous activity, which was refereed as reversible effects in the brain [74]. Several recent studies have proven that amplitudes of evoked potential increased up to 9% before the amplitudes decreased [75]. As described in ARF and cavitation effects in Section 2.3.2, both these two mechanisms have been applied for ultrasound mediated PNS neuromodulation. Wahab et al. demonstrated the negative correlation between amplitudes of AP, conduction velocities, and

ARF while decreasing [76]. Wright et al. showed that the excitation of APs occurred when cavitation signatures were acquired [77, 78].

Ultrasound stimulation in human trials

Some studies have reported that FUS can induce tactile sensation, thermal, types of pain on hand stimulus-responses [79]. Hameroff et al. utilized high-frequency (8 MHz) on the scalp over the posterior frontal cortex to alleviate the pain [80]. Furthermore, a human study on the primary somatosensory cortex (S1) was conducted, and significant changes in EEG responses were observed [81]. Lee et al. chose the same target area, S1, to examine hand tactile sensations using the image-guided tFUS system [82]. In addition, this research group further studied different tactile sensations by stimulating S1 and the secondary somatosensory cortex (S2) together [83]. They also reported that LIFU stimulation on the primary visual cortex (V1) could induce evoked potentials and elevate fMRI blood oxygen level-dependent (BOLD) signals [84]. A recent human study was conducted and demonstrated the feasibility of waking up a post-traumatic disorder patient, which was conducted in animals previously [85, 86].

2.4.1.2 Mechanism of ultrasound neuromodulation

Despite the obvious progress in recent ultrasound neuromodulation applications and the ability of ultrasound to induce the activity of electrically excitable tissues, the mechanisms of ultrasound stimulation remain poorly understood. Many researchers have been conducted to investigate various hypotheses, including experiments and numerical studies. However, the interaction between the nature of acoustic waves and neurons or even molecular-level things is still unclear. Therefore, the heating effect, the ARF effect, and the acoustic cavitation effect, as the main biological effects, have been investigated in many studies.

Thermal effects caused by high intensity focused ultrasound induce biological changes, which may lead to cellular death eventually, and the procedure might contain different tissue changes, such as tissue homogenization, protein denaturation, and DNA fragmentation [87]. Thermal effects induced by LIFU manifest the modulation of neuronal activity levels, such as ultrastructural synaptic changes [88], and synaptic signalling pathways might be disrupted and induce suppression of neuronal activity when thermal changes are below the ablation threshold [89]. Ultrasound parameters, such as sonication time and pulsing waves, might directly affect neuronal tissues. It is worth noting that a number of studies have observed only slight temperature changes (less than 0.1℃) during LIFU neuromodulation [12, 56, 77, 90].

The acoustic cavitation effects induced by the ultrasound mechanism in the bilayer membrane might be another mechanism used to modulate brain function [91]. In the application of tFUS, acoustic cavitation may also induce transient localized BBB disruption, resulting in enhancing the permeability of the BBB and allowing the passage of molecules into the brain [92]. When ultrasound propagates through the tissues in the brain, small bubbles are formed by cavitation effects (vapour and gas pockets are dissolved in the medium). The cavitation effects depend on ultrasound parameters, such as operating frequency, temperature, and negative pressure [93].

2.4.1.3 Safety considerations in low-intensity ultrasound neuromodulation

As described in Section 2.4.1.1 and Section 2.4.1.2, the effects on different ultrasound mechanisms might be induced by exposure parameters (operating frequency, intensity, sonication time, duty cycle, pulse repetition frequency) used in ultrasound stimulation. Compared with LIFU, HIFU can induce irreversible cell death. Thus, safety considerations of LIFU in

neuromodulation need to take seriously as temporal modulation of neural activity without brain damage is required.

The Food and Drug Administration (FDA), the National Electrical Manufacturers Association (NEMA), and the American Institute of Ultrasound in Medicine (AIUM) have reported safety requirements for ultrasound examinations, which contains the MI, the thermal index (TI), spatial-peak pulse-average intensity (I_{sppa}) and spatial-peak temporal-average intensity (I_{spta}) [94, 95]

2.4.2 Blood-brain barrier disruption

2.4.2.1 Approaches for blood-brain barrier disruption

The BBB plays an important role in maintaining cerebral function by isolating the parenchyma selectively [96]. Pardridge has shown that almost large-molecule in neuronal therapeutics and small-molecule drugs cannot pass to the treatment region in the brain [97]. In treating pharmacological CNS diseases, however, it is difficult to deliver the candidate drugs to the target area in the brain as highly selective barriers protect the CNS.

Chemical stimuli to enhance BBB permeability

A number of studies investigated the improvement of paracellular permeability by utilizing chemical stimulation methods to act on the tight junction between endothelial cells. Greenwood et al. used hyperosmotic solutions and mannitol for arterial injection, resulting in shrinking endothelial cells and disruption of the BBB [98]. Salahuddin et al. then demonstrated that chemical substances might induce cellular damage and vascular structural changes [99]. The limitation of the chemical stimulus is the precise target of the desired brain regions, as the chemical substances mostly pass a global effect on peripheral tissue or the whole brain. In addition, some progression of neurological diseases, such as stroke, and

Parkinson's diseases, are heterogeneous, which might induce a potential risk of side effects on unaffected tissues.

Biological stimuli to enhance BBB permeability

Biological stimuli have also been developed to increase the permeability of BBB, and most of the methods are limited to in vitro studies [100]. The mechanism of biological stimuli is similar to chemical stimuli, as biological agents are used for tight junctions, which have an enhancement effect on BBB opening [101]. Various biological agents, such as histamine, used for vasoactive stimulus, are applied [102]. Also, the biological agents, as compounds, can be modified to enhance BBB permeability [103]. The limitation of biological stimuli is similar to chemical stimuli in that the spatial resolution is restricted to precise targeting in the brain. Even though the precise quantities of drugs can be measured, delivering the substances to desired regions in the brain is still different. Jones and Shusta studied specific drug delivery using transport vectors and receptors, but only limited drug doses could successfully be delivered to desired brain regions [104].

Physical stimuli to enhance BBB permeability

Besides tFUS on BBB disruption, some other physical stimuli methods were utilized to open the BBB. Stereotaxic intracranial injections as an invasive method achieved some degree of deep brain targeting, but deeper brain structures (brainstem) cannot be reached [105]. The thermal effect in the brain tissue is studied as another physical stimulus method to open the BBB. Kiyatkin and Sharama applied low-level microwave energy to warm several brain tissues (cortex, hippocampus, thalamus, and hypothalamus) at different levels of temperature (32-42 ℃) [106]. Moriyama et al. showed that temperature increases to 40 ℃ at least in the brain might induce to open BBB [107]. However, thermal manner, as a non-invasive therapy, may lead to the risk of infection when brain temperature increases to such a degree [108]. Another thermal manner for opening BBB is induced using

a low radiofrequency method and electromagnetic pulses [109]. It is difficult for these physical stimuli to reach the specific targets in the brain non-invasively.

2.4.2.2 Ultrasound for blood-brain barrier disruption

Bakay et al. in 1956 first reported the work on enhancing the permeability of BBB when using the HIFU stimulation on lesions [110], and similar studies and observations were also introduced in [68, 111]. These significant works at the early stage of focused ultrasound established the technique of HIFU for tissue ablation and also inspired the idea of opening BBB by tFUS. Then, research works on focused ultrasound brain stimulation in the 1990's proposed that cavitation effects induced by tFUS might enhance the permeability of BBB opening without tissue damage [112] . Later, based on the previous foundation, in 2001 , Hynynen et al. introduced an ultrasound contrast agent (intravenous administration of microbubbles) to the application of tFUS induced BBB opening [92]. Hosseinkhah et al. thought that the behaviour of microbubbles was induced by mechanical effects on the vessel walls [113]. The treatment of microbubble-assisted focused ultrasound (MB+FUS) has an obvious advantage over only FUS applied. The cavitation threshold with the vasculature is lower in MB+FUS than the values in FUS, which means a reduction in the requirement for acoustic intensity for increasing the BBB permeability. Thus, the thermal accumulation induced by acoustic intensity on the skull might also be reduced, which has a positive effect on the safety of MB+FUS applications.

2.4.2.3 Ultrasound parameters affecting blood-brain barrier disruption

Ultrasound operating frequency in the BBB disruption applications has a strong effect on microbubbles response [114]. Several studies have demonstrated that the higher threshold of pressure in the ultrasound field induced BBB disruption with higher operating frequency [115-118]. The

typical range of acoustic frequencies used in BBB disruption is from 28 kHz to 8 MHz [119, 120]. However, because of the characteristics of the skull, the higher frequency might induce a higher degree of attenuation by the skull due to the higher pressure, and the lower frequency might cause an increased focal spot area, which might be beyond the size of the desired target. The optimal frequency is dependent on the desired target and application purpose. In some clinical trials, the range of frequency is between 0.2 MHz and 1.5 MHz [121].

Burst repetition frequency also affects the permeability of BBB disruption. McDannoal et al. studied BBB disruption effects ranging in the burst repetition frequency from 0.5 Hz to 5 Hz [116]. The range was narrowed from 0.1 Hz to 1 Hz, and found a significant increase in the permeability of BBB disruption in [122].

McDannold et al. also demonstrated that increasing the burst duration from 0.1 to 10 ms affects the permeability of BBB disruption, however, there were no extra effects when the burst duration was over 10 ms [116]. A longer burst duration might destruct the microbubbles at the focal spot area during that time, and a short burst duration also enables reaching the threshold for BBB disruption when pressure amplitude is achieved at a high enough level. Chopra et al. demonstrated the enhancement of BBB disruption using the contrast-enhanced MRI technique, and they also reported that the long duration time might induce irreversible tissue damage [123].

Including ultrasound parameters, microbubble parameters, such as the size of microbubbles, types of microbubbles, and injection method of microbubbles, also affect the permeability of BBB disruption [124, 125]. Various sonication parameters and characteristics of microbubbles mentioned in the above studies can induce the effects of BBB disruption.

Thus, regarding safety in the BBB disruption without tissue damage, parameters should be considered based on the experimental conditions.

2.5 Summary

tFUS is a promising brain stimulation technique for its non-invasiveness and higher spatial resolutions and is used for various neuromodulation applications. This chapter provides a thorough literature on focused ultrasound techniques and applications in human brain study. The fundamental principle behind focused ultrasound and various ultrasound transducers used in clinical and pre-clinical trials are presented initially. Then, brain stimulation techniques, such as DCS, DBS, and TMS, are comprehensive compared with tFUS. In addition, the key applications of focused ultrasound in brain stimulation, including ultrasound neuromodulation and BBB disruption, are introduced.

CHAPTER 3: NUMERICAL MODELLING FRAMEWORK

This chapter introduces the relevant numerical models, including a detailed 3D human head model construction, ultrasound wave propagation, acoustic neuromodulation, and thermal effect. We start with a human head model construction, then a basic overview of acoustic and thermal models and how to solve them numerically.

3.1 Computational modelling

Computational methods, as valuable tools, play a vital role in improving the effectiveness of clinical trials and pre-clinical applications. They can help with the simulation of acoustic propagation, ultrasound transducer design, the position of target region selection, and operating system design to improve treatment efficacy. It is possible to obtain quantifiable observations and test hypotheses in different situations by placing the pre-clinical and clinical conditions in a mathematical model. It is difficult and sometimes impossible to manually explore various stimulation conditions with large parameter space as the therapeutic treatment trials are too complex. Numerical modelling and algorithms in focused ultrasound stimulation are feasible to explore different treatments and find optimal parameters.

The growth of computational resources, including high performance of graphic processor unit (GPU) hardware, high-quality imaging modalities (MIR and CT images), and the development of mathematical frameworks, enables the placement of various clinical trials (experience independent data and observed phenomena) into numerical models. For example, MRI and CT can be used as efficient imaging modalities to construct a detailed human head model and quantify brain connectivity maps in tFUS

applications. In addition, numerical modelling methods can be used to visualize how acoustic waves propagate through the skull and the temperature changes in the desired brain tissue. Setting parameters is more flexible based on experimental needs, and real-time feedback can also be achieved in real-time treatment.

Numerical models of ultrasound stimulation have been applied in many therapeutic applications, which have led to an understanding of the mechanisms of ultrasound neuromodulation and improved treatment safety. Huh et al. studied the effects of incidence angles of acoustic waves on different brain tissues on BBB permeability using the same power of focused ultrasound [126]. Suomi et al. used numerical methods to investigate the attenuation, sound speed, perfusion, thermal conductivity and the variability of heating induced by HIFU for the non-invasive treatment of kidney cancer [127]. Furthermore, the impact of skull heterogeneity and parameters of CT images have been studied on the accuracy of acoustic wave propagation in a numerical way [128]. These computational models set an example of safety considerations for clinical trials and enable the computation of some extremum values that cannot be directly measured and must be estimated.

3.1.1 Human head model geometry and brain tissue properties

The geometry of a 3D, highly detailed human head model was built from the MRI human-head datasets, which was used to generate volumes of MRI data from the Simulated Brain Database of the Brain Web [129]. The volume images have a 1 mm^3 isotropic voxel resolution with 181×181×217 slices in the axes of transverse, sagittal, and coronal. The detailed construction process followed the same pipeline as our previous studies [130]. Specifically, GM, WM, CSF, fat, muscles, eyes, and scalp tissues were segmented by applying T1-weighted MRI volume data. Meanwhile, T2-weight and Proton Density MRI volume data were applied to segment skull

and CSF. The brain tissue masks of GM, WM, CSF, skull, scalp, and nine subcortical tissues (thalamus, hippocampus etc.) were generated using FMRIB's Software Library (FSL) [131]. The tissues of fat, muscle and eyes were semi-automatic segmented using the ScanIP module from the commercial software package, Simpleware Version P-2016.09.

Blood, skull, muscle, CSF, GM, WM, fat, scalp, and brain, as the main structures of the anatomical models, were used for focused ultrasound stimulations. Table 3-1 provides the material properties of these tissues from IT'IS database [132]. The distance between SEFT and the brain scalp was 15 mm, which was regarded as the water layer [57, 73]. The completed 3D human head model with brain tissues is displayed in Figure 3-1.

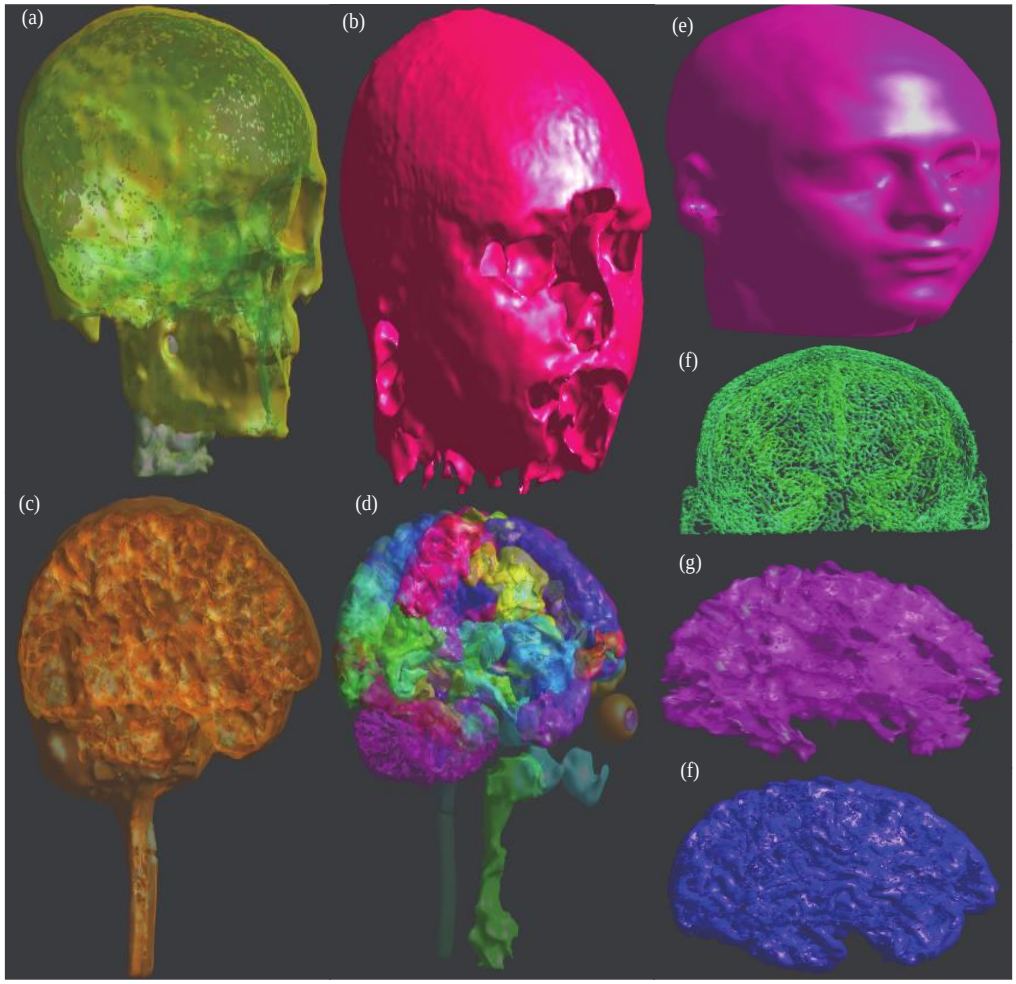

Figure 3-1 A 3D human head model (a) Skull, (b) Fat, (c) CSF, (d) Brain tissues, (e) Scalp, (f) Blood vessel, (g) White matter, (h) Grey matter

Table 3-1 Tissue properties [132]

Material	Sound of speed (m/s)	Density (kg/m^3)	Acoustic impedance (Mpa·s/m)	Attenuation coefficient (Np/m)
Water	1483	999.5	1.5	0.02
Skull (inner table)	2300	1912	4.4	81
Skull (outer table)	2300	1875	4.3	81
Skull (dipole)	2013	1740	3.5	60.8
CSF	1483	999.5	1.5	0.02
GM	1550	1030	1.6	0.92
WM	1550	1030	1.6	0.92
Fat	1440	911	1.3	2.1
Scalp	1624	1109	1.8	10.6
Brain	1552	1046	1.6	2.76

3.2 Computational framework

Sim4Life is a computational simulation platform developed by the IT'IS Foundation and ZMT Zurich MedTech. The platform combines multi-physics solvers (such as EM full wave solvers, thermodynamics solvers, and acoustic solvers) with advanced computable tissue models (such as IT'IS Virtual Population models), for directly designing complex medical devices and simulating real-world biological phenomena. The computable human and animal phantoms provide a realistic biological and anatomical environment for mechanistic computing and validation. The platform also offers a medical image segmentation framework for reconstructing specific tissue models, an integrated high-performance computing framework, analysis and visualization functionalities, and a controlling framework via Python scripting.

3.2.1 Acoustic full-wave models

The Rayleigh-Sommerfeld integral and the Angular Spectrum method are two typical acoustic beam models. However, the capabilities of acoustic

beam models are restricted by certain conditions, such as a homogeneous medium. The details of this type of acoustic model can be found in [133-135]. Compared with acoustic beam models, acoustic full-wave models provide an accurate and realistic acoustic wave propagation method, and they have advantages in heterogeneous mediums. The linear acoustic pressure wave equation (LAPWE) is the most fundamental full-wave model of acoustic wave propagation [136]. LAPWE is derived through fluid dynamic equations, and the partial differential equation of LAPWE is provided below:

$$\rho \nabla \frac{1}{\rho} \nabla \rho - \frac{1}{c^2} \frac{\partial^2 p}{\partial t^2} - \frac{\tilde{\alpha}}{c^2} \frac{\partial p}{\partial t} = 0$$

$$\tilde{\alpha} = 2\alpha \sqrt{\frac{\alpha^2 c^4}{\omega^2} + c^2} \qquad \text{Equation 3-1}$$

where ρ is density, c is sound speed, α is attenuation, p is pressure, t is time, and ω is angular frequency.

LAPWE as a simple and efficient model, has been implemented with some popular methods, such as FDTD [137] and finite elements methods (FEM) [138] for solving partial differential equations. In addition, as an acoustic full-wave model, LAPWE can account for various acoustic wave transmission phenomena, such as reflection, scattering, and diffraction [22]. However, the capabilities of the LAPWE are limited by modelling in non-linear acoustic wave propagation [139]. Thus, LAPWE is most limited in applying HIFU, as the LAPWE model can only be used for longitudinal waves. Another factor that LAPWE cannot be accounted for is energy absorption, which is induced by a medium in acoustic propagation. Thermal effects diminish the application of LAPWE in focused ultrasound stimulation. Mast et al. proposed the Lossy LAPWE method to overcome these limitations [140], and this method has been implemented with the FDTD scheme into Sim4Life software.

The Westervelt-Lighthill Equation (WLE), as a non-linear full wave equation, is used for modelling acoustic wave propagation in soft tissues. WLE was proposed by Westervelt using the second-order wave equation induced by Lighthill's fluid particle motion equation [141]. In order to investigate the non-linear acoustic effects, WLE is derived based on the LAPWE equation, which is extended with terms of dispersion and frequency terms, and the WLE partial differential equation of WLE is shown below:

$$\rho \nabla \frac{1}{\rho} \nabla \rho - \frac{1}{c^2} \frac{\partial^2 p}{\partial t^2} + \frac{\delta}{c^4} \frac{\partial^3 p}{\partial t^3} + \frac{\beta}{2\rho c^4} \frac{\partial^2 p^2}{\partial t^2} = 0 \qquad \text{Equation 3-2}$$

where ρ is the material density, c is the speed of sound, p is the acoustic pressure, t is time, β is the nonlinearity coefficient, and δ is the sound diffusivity, and $\delta = 2\alpha c^3/\omega^2$, where α is the attenuation coefficient with unit Np/m, and ω is the angular frequency. The WLE solver implemented in Sim4Life has been modified to increase time-steps and improve stability performance, which enhance the ability of converting transient signals into complex phasors at multiples of the carrier frequency [21]. Therefore, it can explain for all acoustic wave propagation phenomena, including non-linearity, without being limited by quasi-axial proximity.

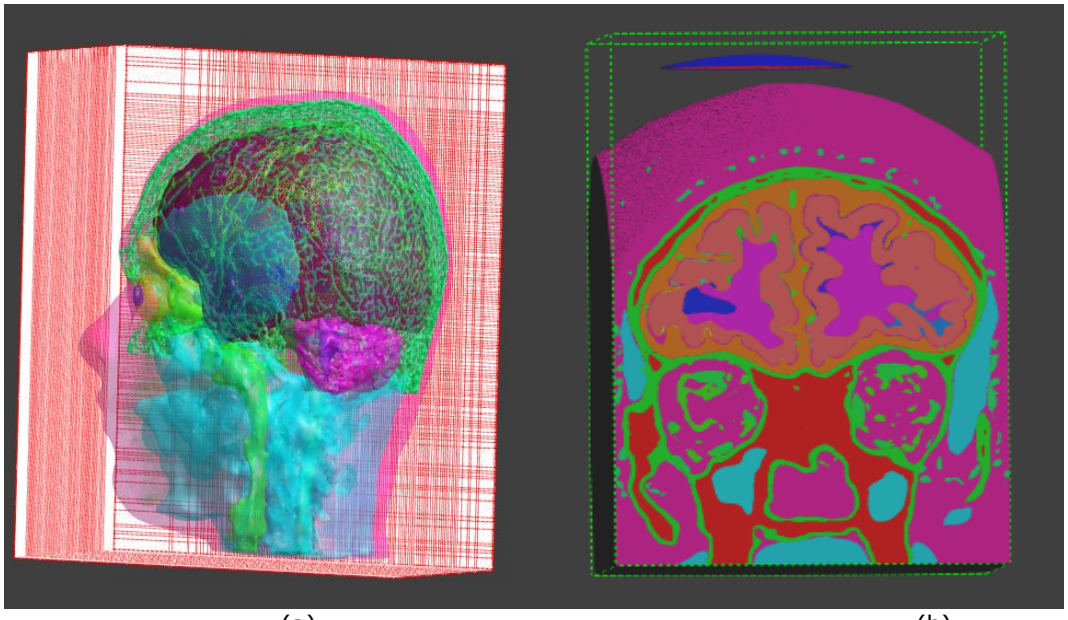

(a) (b)

Figure 3-2 Depiction of the gridding and voxeling applied to a 3D human head model with a single-element transducer. (a) Non-uniform computational grids, (b) A simple example of voxeling.

3.2.2 Finite-differences time-domain method

The FDTD method was introduced by Yee in 1966 [142], and FDTD is a prevalent computational approach to solving Maxwell's equation in a three-dimensional domain across all disciplines. Discretization forms a rectangular or rectilinear grid termed the computational grid as an initial gridded process. Typically, there are two types of grids, uniform and non-uniform computational grids. The FDTD algorithm implements the solver in Sim4Life with non-uniform grids, which enhances the refinement of the discretization, such as the resolution near the source, and sharp features, in computational cells (Figure 3-2 (a)). Voxeling as an assigning procedure followed by a gridding step is processed to assign modelling properties for each material (Figure 3-2 (b)). Thus, a set of rectangles or cuboids termed voxels will be reconstructed.

Maxwell's equations are discretised, and the spatial and temporal derivatives are approximated using finite difference:

$$\frac{\partial F(i,j,k,n)}{\partial x} = \frac{F^n\left(i+\frac{1}{2},j,k\right) - F^n\left(i-\frac{1}{2},j,k\right)}{\Delta x} \quad \text{Equation 3-3}$$

$$\frac{\partial F(i,j,k,n)}{\partial t} = \frac{F^{n+\frac{1}{2}}(i,j,k) - F^{n-\frac{1}{2}}(i,j,k)}{\Delta t} \quad \text{Equation 3-4}$$

where i, j, k as cell integer values refer to spatial variables and *n* terms to the time step.

Electric and magnetic fields are typically discretised on spatially and temporally staggered grids to reduce discretization errors [142]. Finite differences are applied to Maxwell's equations in the following form:

$$\nabla \times H = \frac{\partial}{\partial t}\epsilon E + \sigma E \quad \text{Equation 3-5}$$

$$\nabla \times E = -\frac{\partial}{\partial t}\mu H - \sigma H \quad \text{Equation 3-6}$$

The time-step Δt should be bounded to perform the simulation in a stability state, as the numerical errors induced by the time-step Δt may be accumulated throughout the calculating process. On uniform rectilinear

meshes, Courant-Friedrichs-Lewy condition (CFL condition (detailed in [137])) [143] is used as the criteria to limit the time-step Δt and material properties-dependent in the implementation of FDTD.

$$\Delta t \leq \frac{1}{c\sqrt{\frac{1}{(\Delta x)^2}+\frac{1}{(\Delta y)^2}+\frac{1}{(\Delta z)^2}}} \qquad \text{Equation 3-7}$$

where c is the sound speed and Δ are the dimensions of a given cell.

Grid step as another relevant parameter in the FDTD implementation affects the discretisation degrees of space and stability of numerical calculation. In modelling of acoustic wave propagation, dispersion as a deviation phenomenon is induced by sound speed in a certain tissue and numerical phase velocity [137]. Also, the grid size, acoustic wavelength λ, and wave propagation direction, affect deviation in computational modelling. The accumulation computing errors induced by dispersion might lead to undesired results, such as distance of acoustic wave propagation. Thus, the rule of discretization settings in Sim4Life is that the maximum step must not exceed 1/10 of the wavelength λ ($Grid\ maximu\ step \leq \frac{\lambda}{10}$). For example, the acoustic wave propagates in a water tank, the setting of maximum step should smaller than 0.3 mm (see Figure 3-3) when the operating frequency of transducer is 0.5 MHz, as the speed of sound in water is 1483 m/s (cell size $\leq \frac{\lambda}{10} = \frac{c}{10*f}$).

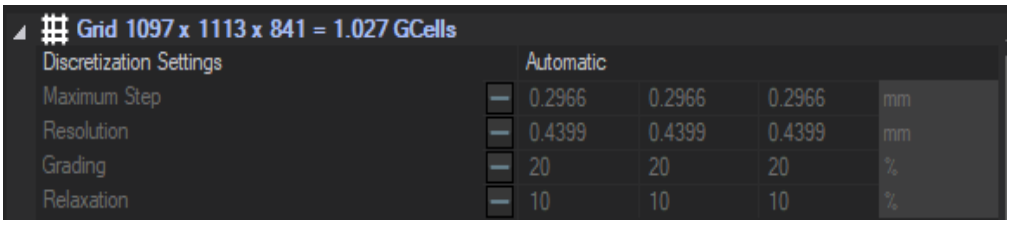

Figure 3-3 Example of gridding settings in Sim4Life

3.2.3 Thermal Modelling

The thermal solver is based on a finite-differences implementation with conformal corrections of Pennes' bioheat equation (BHE) [144].

$$\rho C \frac{\partial T}{\partial t} = \nabla \cdot (k \nabla T) + \rho Q + \rho S - \rho_b C_b \rho \omega (T - T_b) \qquad \text{Equation 3-8}$$

where ρ is the medium density, C is the specific heat capacity, T is the tissue temperature, k is the thermal conductivity, Q denotes the metabolic heat generation rate, ω is the perfusion rate, and ρ_b, C_b, and T_b are the density, specific heat capacity, and temperature of the blood, respectively. The symbol S denotes the time-averaged rate of heat generation by relaxation absorption in a tissue of a continuous sound filed [145].

$$S = \alpha \frac{p^2}{\rho c} \qquad \text{Equation 3-9}$$

where ρ is the medium density, c is the sound speed, α is the absorption coefficient, and p is the absolute acoustic pressure. From the above equations, it is obvious that the thermal solver can be coupled with acoustic solver, and the temperature accumulation in the tissues can be induced and calculated due to the exposure to acoustic fields.

Similar theory with acoustic simulation using the FDTD method, the maximum time step should be guaranteed for stability computing, and it can be calculated as:

$$\Delta t \leq \frac{2\rho c}{\rho\rho_b c_b \omega + 4k(\Delta x^{-2} + \Delta y^{-2} + \Delta z^{-2})} \qquad \text{Equation 3-10}$$

However, in thermal modelling, the calculation of stable time-step is more complicated. There are many factors, such as boundary conditions, grid setting, and interfaces between two different materials, may affect the stable time-step measurements.

3.2.4 Boundary conditions

3.2.4.1 Acoustic boundaries

A perfectly matched layer (PML) is an absorbing layer used as an important numerical condition in wave propagation simulations, which is typically applied to truncate computational regions, especially in the FDTD and FE methods. PML was originally introduced into electrodynamics by Berenger in 1994 [146]. In the application of PML, multiple layers of an absorbing

material are placed to the boundaries of cell grids and the complete computational region is surrounded by a 3D perfectly reflecting boundary (see Figure 3-4). The key difference between an ordinary absorbing material and an PLM is that the acoustic waved do not reflect at the interface when the incident waves propagate upon the PML. Thus, the outgoing acoustic waves from the interior of a computational domain do not propagate back into the interior domain, and the detail of PML analysis and implementation can be found in [137].

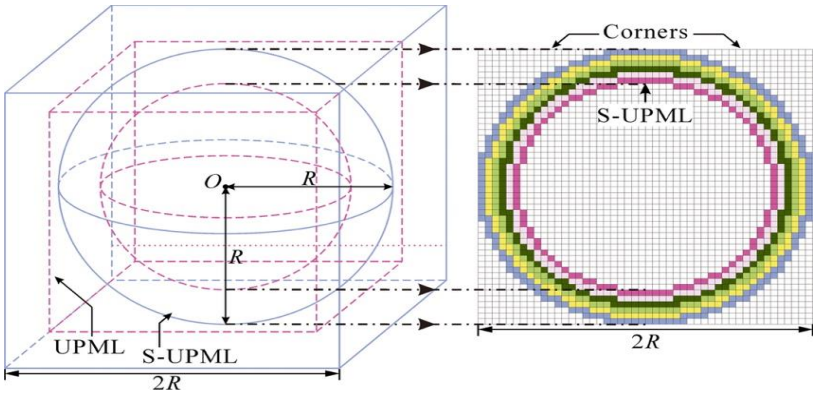

Figure 3-4 A simple example of uniaxial perfectly matched layer (PML) [147]

The boundary condition, PML, implemented in acoustic solver was applied on LAPEW, and then extended by stretched-coordinated approach [148]. The LAPEW is described below:

$$\rho\nabla\frac{1}{\rho}\nabla\rho-\frac{1}{c^2}\frac{\partial^2 p}{\partial t^2}=0 \qquad \text{Equation 3-11}$$

where c is the sound speed of the materials, and the PMLs are used to match against materials:

$$\widetilde{\nabla}_s^2\,\tilde{p}-\frac{1}{c^2}(j\omega)^2\tilde{p}=0 \qquad \text{Equation 3-12}$$

$$\widetilde{\nabla}_s=\frac{1}{s_x}\frac{\partial}{\partial x}+\frac{1}{s_y}\frac{\partial}{\partial y}+\frac{1}{s_z}\frac{\partial}{\partial z} \qquad \text{Equation 3-13}$$

where s_x , s_y , s_z are the stretched coordinates in three dimensional directions (x, y, z directions, respectively).

3.2.4.2 Thermal boundaries

There are three types of thermal boundary conditions which can be applied to selected interfaces between different regions at different conditions.

Dirichlet boundary condition defines a fixed, homogeneous temperature at the interface ($T = T_{boundary}$). Compared with Dirichlet boundary condition, *Neumann* boundary condition specifies a constant heat flux through the boundary. Positive and negative heat flux values indicate the heat flux out and into the active domain ($\frac{k\,dT}{dn} = F_{boundary}$). Lastly, the *Mixed* boundary condition allows to set an energy flux, which relates to a specific environment temperature $T_{outside}$ or a specific temperature at interface, based on the heat transfer coefficient h. The Mixed boundary condition can be expressed as ($\frac{k\,dT}{dn} + h(T - T_{outside}) = F_{boundary}$).

3.3 Computational settings

The figure below demonstrates the computational settings in Sim4Life, including setup for mathematical model selecting, material properties assignment, acoustic sources, boundary conditions, acoustic sensors, gridding and voxeling settings (see Figure 3-5).

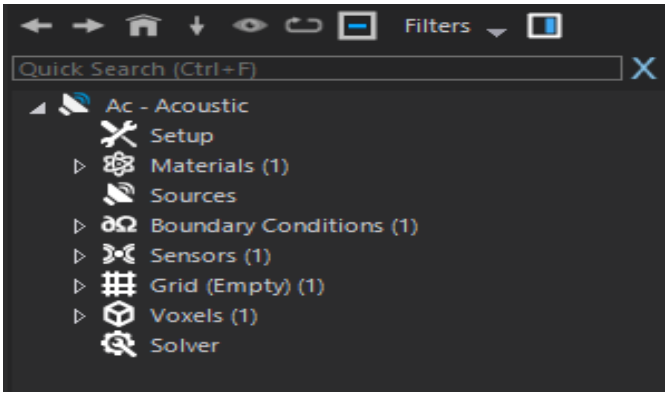

Figure 3-5 Procedure of acoustic simulation

Setup: The mathematical model can be selected as LAPWE and WLE (Figure 3-6). LAPWE as a simple and efficient model, has been described in section 3.2.1. It is worth noting that WLE allows the simulation of the propagation of a harmonic pressure wave in heterogeneous lossy materials, capturing phenomena like scattering, reflection, and absorption. The frequency referred to as the operating frequency from the harmonic sources is specified in MHz. The periods are regarded as the duration of the acoustic

excitation. Typically, the number of periods should be large enough as the acoustic waves propagate to the desired region with sufficient time. In the application of tFUS, acoustic wave reflections, scattering, and interference should be taken into account, and the duration of acoustic wave propagation contains emission and reception time. Periods setting depends on the investigated effects and computational time.

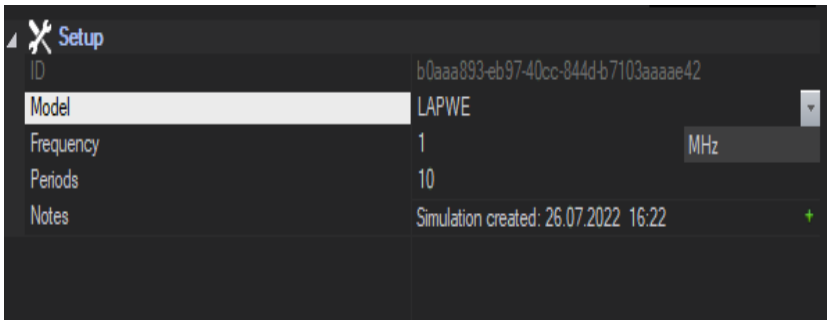

Figure 3-6 Simulation models in setup settings

Materials: The acoustic properties of assigning a material include density, sound speed, attenuation coefficient, and characteristic acoustic impedance. It is noted that the attenuation coefficient determines the absorption characteristics of a specific material at a certain operating frequency.

Sources: The acoustic waves emanate from piezoelectric elements, which is typically represented by volumetric model of transducers. Modern transducers consist of arrays of sources, which are configured at certain amplitude and phase relations.

Boundary conditions: PML are used for absorbing boundary conditions and the details are provided in Section 3.2.3.

Sensors: Sensors are performed to record the acoustic simulation results. Typically, the spatial pressure distribution, acoustic intensity, deposited power density, and specific energy absorption rate are quantity calculated as below, respectively (pressure distribution calculation in Section 3.2.1):

$$I = \frac{p^2}{2 \cdot \rho \cdot c}$$ Equation 3-14

$$\frac{dP}{dV} = 2 \cdot \alpha \cdot I = \alpha \cdot \frac{p^2}{\rho \cdot c}$$ Equation 3-15

$$S = \alpha \cdot \frac{p^2}{\rho^2 \cdot c}$$ Equation 3-16

where I is the acoustic intensity, ρ is the medium density, c is the sound speed, p is the absolute acoustic pressure, α is the absorption coefficient, $\frac{dP}{dV}$ is the deposited acoustic power density, and S is the specific energy absorption rate.

Grid and Voxels: The grid determines the discretization of the computational domain into computational cells, and the details are introduced in Section 3.2.2.

3.4 Needs and limitations of computational modelling

Numerical modelling of brain stimulation in therapeutic applications typically focuses on physical exposure. For example, acoustic wave propagation simulations study the pressure-strength or intensity change in the targeted brain tissues. Thermal modelling focuses on determining thermal accumulation and temperature changes during stimulation time. This is true for numerical simulation in therapeutic treatment planning. However, the quantified metrics of physical exposure are not always direct or highly correlated with physiological changes. The computational modelling might provide a safety or efficacy system for the clinical estimator and identify some limitation exposure metrics. Also, numerical modelling provides an efficient method to compute extreme conditions for metrics testing. Hybrid or multi-physics modelling, such as acoustic and thermal computational simulation in tFUS, might improve the mechanistic insights for therapeutic applications rather than only resulting from one computational physics modelling.

- tFUS: Without computational modelling, it is difficult to predict the focal spot location, acoustic pressure changes, focality of the acoustic waves, and potential physiological impacts on the brain. A number of the research described in Section 2.3.2 used computational tools to study tFUS questions in pre-clinical and clinical trials. However, the computational prediction of tFUS remains unreliable.

- Validation: The high degree of reliability in tFUS applications (e.g., therapeutic treatment and safety consideration) is required, including ultrasound transducer design, method of acoustic propagation, and simulation results. Before conducting simulation experiments, the modelling tools must be verified, and quantity measurements with some clinical data. Also, some factors, such as material properties, placement of transducers, and the size of transducers, should be selected properly, which ascertains the intended model implemented correctly. Results analysis also needs to be quantified, such as the volume of focal spot area, comparison of maximum pressure, and location of the focal point, which has a positive effect on understanding the exposure modelling.

- Personalised treatment: In the clinical trials of focused ultrasound neuromodulation and therapeutic treatment, the characteristic of subjects has great interpersonal differences, such as the structure of tissues, and thickness of the skull, which might have a direct impact on penetration, and absorption of acoustic wave propagation. However, personalised modelling remains limited as the optimisation treatment requires manual adjustment, and a single numerical simulation case cannot easily fit a different variety of simulation parameters. Typically, physiological assessment heavily relies on the experience of clinical experts. With the development of computer-assisted techniques, such as MRI and CT images, the trial-based optimisation is possible to achieve.

- Mechanistic understanding: Mechanistic understanding is not only required to have a clear understanding of principles of physical exposure, such as acoustic and thermal impacts but also to provide therapeutic risks guideline and improve the treatment efficacy.

These needs and limitations motivated our works in this dissertation.

CHAPTER 4: ENERGY DISTRIBUTION IN LOW-INTENSITY TRANSCRANIAL FOCUSED ULTRASOUND NEUROMODUALTION

The objective of this chapter is to numerically investigate the ultrasound wave propagation and the energy distribution within the brain tissues using customised SEFT, targeting the hippocampus. Customised SEFTs were used to test the effect of transducer positions and compare the sensitivity effect on heterogeneous and homogeneous brain models. Also, the sensitivity and performance of LIFU stimulation were evaluated. In the numerical study of ultrasound brain stimulations, ultrasound parameters and the brain model were properly designed to simulate ultrasonic neuromodulations.

4.1 Introduction

One of the challenges in applying ultrasonic neuromodulation is ultrasound delivery through the brain. The skull is a highly heterogeneous structure, with soft tissue surrounding it, and has a higher density and sound speed, which might induce a mismatch of impedance. From small animals to large animals and humans, the aberration and attenuation of the acoustic wave become more significant as the thickness of the skull increases [149]. Like many other non-invasive brain stimulation techniques, the presence of the skull greatly disrupts the penetrated energy when an acoustic wave propagates through it. In addition, the thickness of the skull varies with age, gender, and interpersonal differences.

Multi-element arrays with hundreds of individual transducers are able to address the problem related to the skull, which corrects the acoustic wave to compensate for the aberration and focus in the deep brain region [150, 151]. Compared with the multi-element ultrasound transducer applications, the hardware demand of the SEFT is relatively low, and the cost is much

less, which increases its accessibility. However, it is still difficult to access ideal deep brain regions via SEFT. The development of an acoustic lens, which can adjust the incident wave phase, can correct the aberration and relocate the beam into the target region [152].

Some studies using SEFT have been reported in ultrasonic neuromodulation. Mueller et al. [153] investigated the ultrasound wave propagation and heat transfer through the skull by creating a two-dimensional geometry with axial symmetry, including four main layers of the skull, CSF, GM and WM. Legon et al. [154] have proven it is possible to stimulate cortical tissue in humans using SEFT, presenting the potential of tFUS to modulate neural targets. In their study, however, the deflection angles of the ultrasound transducer were not considered, and the whole brain was modelled as a single tissue type. Mueller et al. [155] numerically investigated the skull effect, different transducer placements, and two different operating frequencies when the ultrasound wave propagates through the brain. It is difficult to evaluate the intracranial effect because the skull is the main barrier to energy attenuation and wave distribution. The construction of a high-resolution, detailed human head model is one of the fundamental steps to precisely evaluate the wave propagation performance within the intracranial tissues.

4.2 Methods

Four sequential works were conducted to numerically investigate the ultrasound wave propagation and the energy distribution within the brain tissues using customised SEFT and targeting the hippocampus. First, the MRI-based high-resolution, detailed human head model was constructed (details in Section 3.1.2). Second, the transcranial focused ultrasound propagation model and proposed transducer configurations were developed. Third, ultrasound propagation in a water tank as a validation case was conducted to test the reliability and feasibility of SEFT. Furthermore, the

simulation of tFUS at low intensity was carried out after assigning tissue properties and boundary conditions. Finally, the sensitivity of ultrasound propagation was investigated by changing the position of the ultrasound transducer and tissue parameters.

4.2.1 Transducer Design

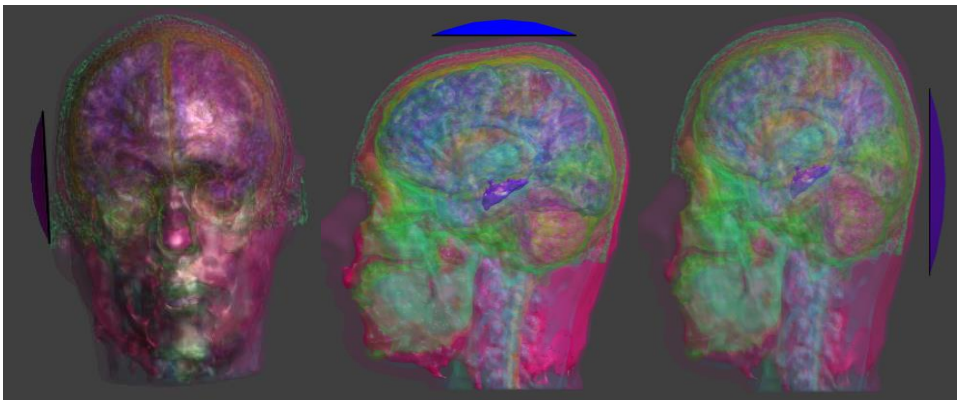

(a) (b) (c)

Figure 4-1 Three customised SEFT at different positions, (a) Left side, (b) Top side, and (c) Back side of the brain.

Three customised SEFTs have been developed with a centre frequency of 0.5 MHz. The tFUS with a customised 0.5 MHz frequency has been used in other studies [52, 154, 155]. Lower and higher transcranial frequency might cause heating risks and change the size of the focal area. Ye et al. [156] investigated ultrasonic neuromodulation effects in the mouse brain at frequencies below and above 1 MHz. The temperature elevation was less than 0.02 ℃ when the operating frequency was below 1 MHz. In addition, the investigation of the frequency dependence demonstrated that higher frequencies generated a smaller focal spot size and vice versa [156]. In this study, three different sizes of transducers were used and placed at the left, top and back positions, illustrated in Figure 4-1. The geometrically focused transducer in the left position had a curvature radius of 80 mm and an aperture width of 75 mm. The SEFT in the top and back position had a curvature radius of 135 mm, 110 mm and an aperture width of 90 mm and 85mm, respectively. Due to the different distances between the target region and three transducer placements, three customised SEFTs with

different radii and apertures were used to provide focal spots with enough focal lengths to the deep brain target region with a minimum intensity of 100 W/m^2.

4.2.2 Ultrasound governing equations

The ultrasound propagation simulation platform based on the commercial software package Sim4Life [157] was used to construct the LIFU to stimulate the hippocampus. The non-linear variants based on WLE were used to generate ultrasound propagation through the human head models [141, 158]. The WLE (Equation 4-1) was extended with varied tissue density term. This was done to account for the differences in density that occurrs between two adjacent brain tissues of interface voxels when tFUS propagates through human head models. The WLE was also discretized using 3D FDTD method, as this can have a positive effect on assigning material properties (impedance, attenuation coefficient, density, and sound of speed) of brain tissues [159].

$$\rho\nabla\cdot\frac{1}{\rho}\nabla\rho-\frac{1}{c^2}\frac{\partial^2 p}{\partial t^2}+\frac{\delta}{c^4}\frac{\partial^3 p}{\partial t^3}+\frac{\beta}{2\rho c^4}\frac{\partial^2 p^2}{\partial t^2}=0 \qquad \text{Equation 4-1}$$

where ρ is the material density, c is the speed of sound, p is the acoustic pressure, t is time, β is the nonlinearity coefficient, and δ is the sound diffusivity, and $\delta = 2\alpha c^3/\omega^2$, where α is the attenuation coefficient with unit Np/m, and ω is the angular frequency.

4.2.3 Validation simulation in a water tank

As Mueller et al. did in [153], a computational model of tFUS in a water tank at the same operating frequency and transducer size was constructed in the commercial software package platform, COMSOL.

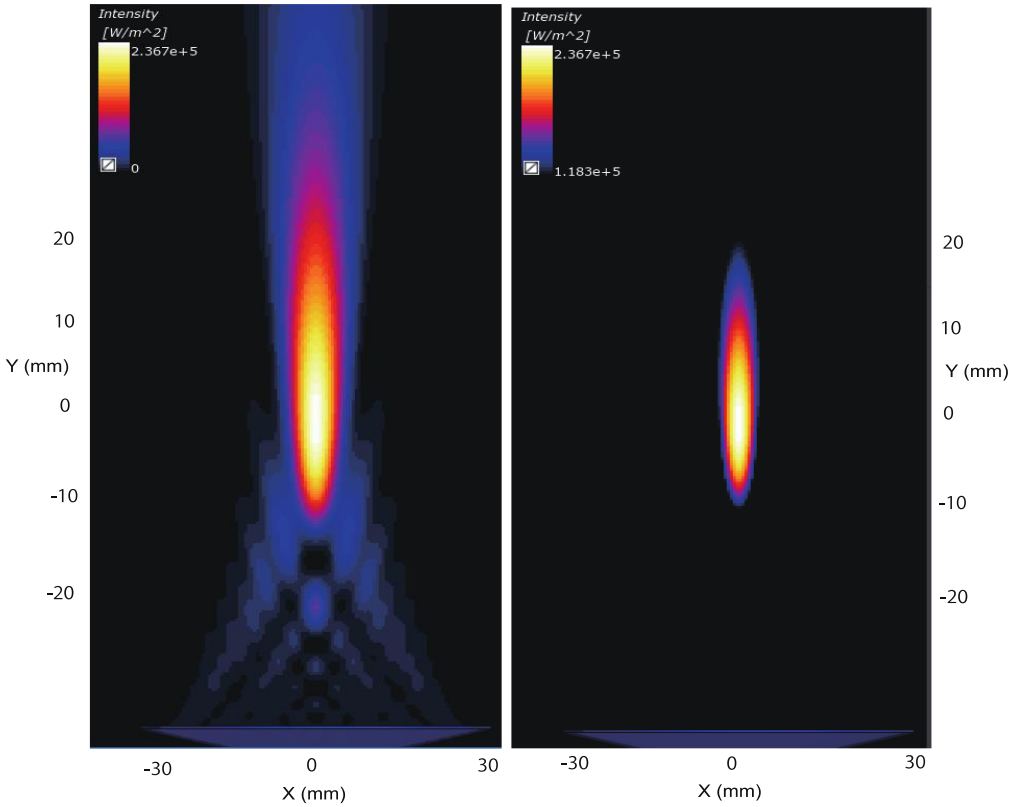

Figure 4-2 Wave propagation in free water. (a) Intensity distribution. (b) Half maximum intensity profile.

The validation simulation was carried out in a water tank using Sim4Life. The customised SEFT was used with the operating frequency of 0.5 MHz, curvature radius at 50 mm, aperture width at 30 mm, and source amplitude at 0.145 MPa. The transducer properties are listed in Table 4-1. The size and frequency of the customized transducer are also used in experiment case [153]. The two-dimensional intensity distribution in the YZ plane is displayed in Figure 4-2 (a), and the FWHM regarded as the focused ultrasound stimulation area is presented in Figure 4-2 (b). In Table 4-2, the origin of the x and z axis was the centroid of the transducer, and the origin of the y axis was set at the central point of FWHM. However, the y axis origin was set at the central point from the maximum intensity of the y direction in the COMOSL model and experiment model [153]. Experimental results had a slight difference from the numerical results, which might have been caused by mounting the transducer in the acoustic tank.

The maximum intensity of focused ultrasound stimulation was 23.67 W/cm^2 and the maximum pressure was 0.83 MPa. The comparison of results between the experiment and computation model is shown in Table 4-2. Comparing the Sim4Life model results with the COMSOL model results, the maximum pressure was the same at 0.83 MPa and the maximum intensity was slightly different at 23.67 W/cm^2 and 23.66 W/cm^2, respectively. Comparing the Sim4Life model results with the experimental model results, the maximum pressure and intensity were 9.6% and 0.84%, respectively.

Table 4-1 SEFT parameters for the free water validation cases

Parameters	Value
Curvature radius	50 mm
Aperture width	30 mm
Operating frequency	0.5 MHz
Medium's speed of sound	1483 m/s
Source amplitude	0.145 MPa
Source phase	0
Boundary conditions	Perfected matched layers (Absorbing boundary conditions)
Cell size ($(< \lambda/10$)	0.29 mm

Table 4-2 Quantification of the half maximum intensity profile in free water for the validation case

	Experiment [153]	Model (COMSOL) [153]	Model (Sim4Life)
Max pressure (MPa)	0.91	0.83	0.83
Max intensity (W/cm^2)	23.87	23.66	23.67
Major axis (mm)	30.81	29.93	29.13
Minor axis (mm)	3.85	4.28	4.08
Centroid x (mm)	-0.14	0.00	0.00
Centroid y (mm)	8.46	6.84	0.00
Major axis vertical offset (℃)	1.23	0.00	0.00

4.2.4 Parameters for the performance of energy deposition

Beam and target overlap parameters were metrics used to quantify the targeting properties between the expected focal spot areas and the targeted structures, which was also used in [160]. The targeting properties were computed as follows: the target overlap parameter estimated the percentage volume of the targeted region encompassed by the ultrasound beam; the case of a 100% value indicated the ultrasound beam encompassed the entire target region volume, with an intensity above half of the maximum peak intensity; the beam overlap parameter estimated the proportion of the ultrasound beam volume, with an intensity above half of the maximum peak intensity that falls inside the targeted structure; and a 100% value demonstrated that the focal spot beam with above half of the maximum peak intensity was in the entire targeted structure with any collateral structures.

4.2.5 Sensitivity analyses

Some studies have measured the acoustic properties of the human skull [161, 162]. However, the measured data demonstrated some variations. Also, the human head models have slight interpersonal differences. Thus, sensitivity research was conducted to investigate the impact of the properties of brain tissues on tFUS. Different acoustic properties of brain tissues, such as skull, muscle, scalp, GM, and WM, were applied to investigate the influence of brain tissue sensitivity. The acoustic properties, such as attenuation, density, and speed of sound, of the scalp, muscle, skull, and brain (GM and WM) varied linearly. The results were used to examine and analyse the pressure, intensity, beam overlap parameter, and target overlap parameter. For the skull, the variation of attenuation was assigned from -70% (25 Np/m) to +70% (140 Np/m). The sound speed and density of the skull varied from -20% (1840 m/s) to +20% (2760 m/s) and from -15% (1594 kg/m^3) to +15% (2156 kg/m^3) respectively. These

parameters were also reported in other studies [163, 164]. Meanwhile, the acoustic properties of attenuation, density, and sound speed coefficient of the scalp, muscle, and brain were extended to a wide range from -15% to +15% to examine the sensitivity effect and to analyse the ultrasound propagation performance that occurred from varying these properties [163-165]. The acoustic property variations were 20% for the skull and 5% for the scalp, muscle, and brain.

According to the studies [166, 167], to quantitatively evaluate the accuracy of the energy deposition at the target region, changes to maximum pressure and maximum intensity can fall within a 5% error criteria. In this study, two other indexes, the target and beam overlap parameters, were used to evaluate the effective volume region between the hippocampus and the generated volume beam above the half-maximum intensity threshold.

4.3 Results and analysis

4.3.1 Results of modelling in a water tank

During the simulation of ultrasound propagation in a water tank using the Sim4life platform, the intensity of ultrasound energy was 100 W/m^2 when the single-element ultrasound transducer with pressure amplitude was 0.839 kPa. Figure 4-3 (a) and (b) show the ultrasound propagation simulations in a water tank at 100 W/m^2 and the corresponding FWHM region, respectively. The same ultrasound input parameters and source amplitude were then used to simulate ultrasound propagation using the constructed 3D highly detailed human head model. Figure 4-4 demonstrates the result of ultrasound propagation in the 3D human head model with intensity distribution. Table 4-3 shows the results of the ultrasound propagation in the water tank and human head model at a different source amplitude.

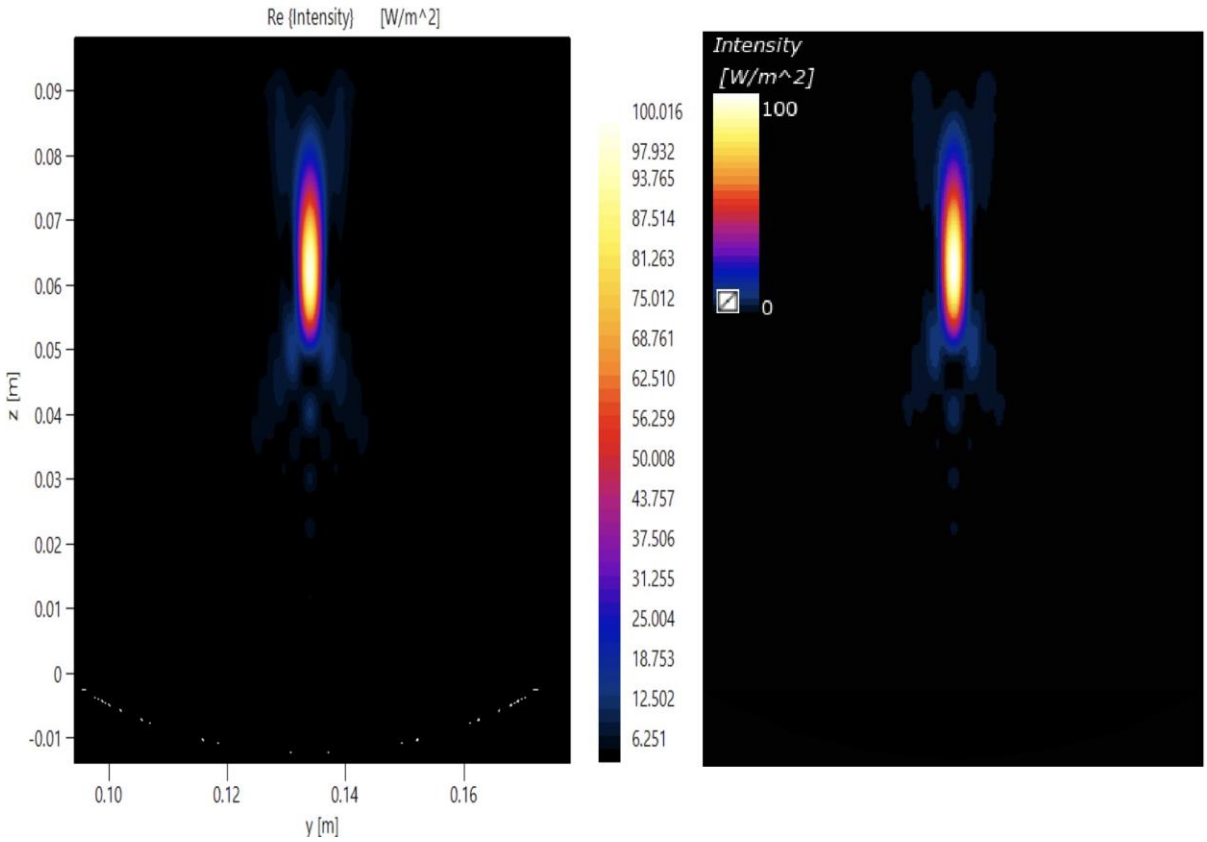

(a) (b)

Figure 4-3 Intensity distribution in a water tank (a) Intensity distribution in 100 W/m^2 in YZ plane. (b) FWHM region in YZ plane.

Specifically, the maximum pressure and intensity decreased by 56.63% and 81.96%, respectively, compared to the human head model and the water tank results. The target overlap parameter was 3.95% (2.67% in the water tank), and the beam overlap parameter was around 80% (85.94 in the water tank) in the human head model. Meanwhile, the peak displacement was around 1 mm along the ultrasound propagation direction.

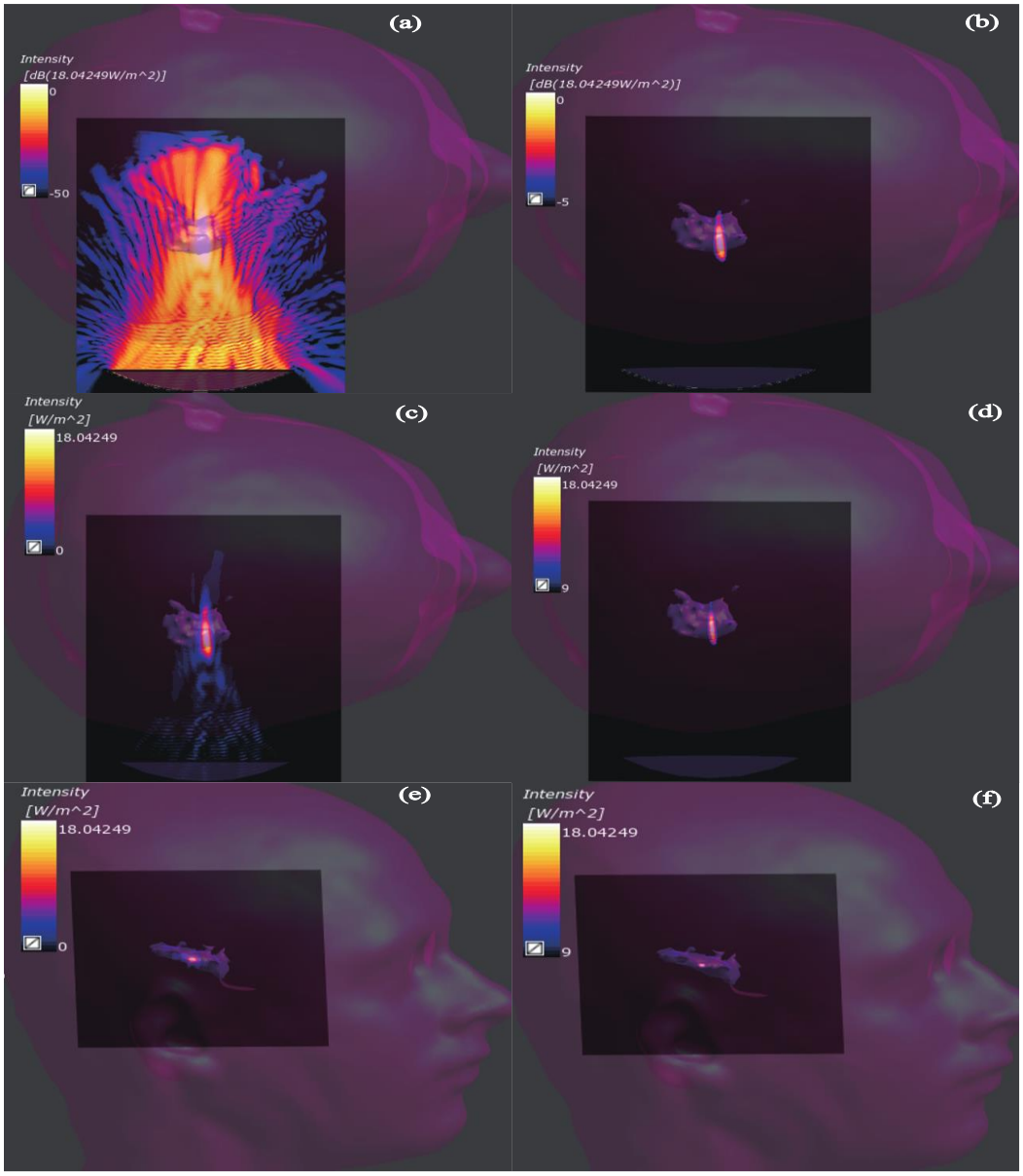

Figure 4-4 Results of ultrasound propagation with intensity distribution and corresponding FWHM region. Intensity distribution in the XY plane in dB reference (18 W/m^2) from 0 to −50 dB (a), from 0 to −5 dB (b). Intensity distribution in the XY plane, from 18 to 0 W/m^2 (c) and from 18 to 9 W/m^2 (d). Intensity distribution in the YZ plane, from 18 to 0 W/m^2 (e) and from 18 to 9 W/m^2 (f).

In order to reach the maximum intensity at 100 W/m^2, the source amplitude was 1.98 kPa (an increase of 136% compared with the source amplitude in a water tank). The major axis and minor axis increased to 22.6 mm and 3.28 mm respectively, and the volume of the focal area was greater than in a water tank.

Table 4-3 Results of the comparison ultrasound propagation in a water tank and 3D human head model

	Free water	Non-adjusted intensity (0.839 kPa)	Adjusted intensity (1.98 kPa)
Max pressure (kPa)	17.13	7.43	17.5
Max intensity (W/m^2)	100.2	18.04	100.5
Peak displacement (mm)	-	1+0.5	1.2+0.6
Major axis (mm)	19.4	20.20	22.6
Minor axis (mm)	2.60	2.76	3.28
Target overlap (%)	2.67	3.95	3.78
Beam overlap (%)	85.94	79.75	77.84

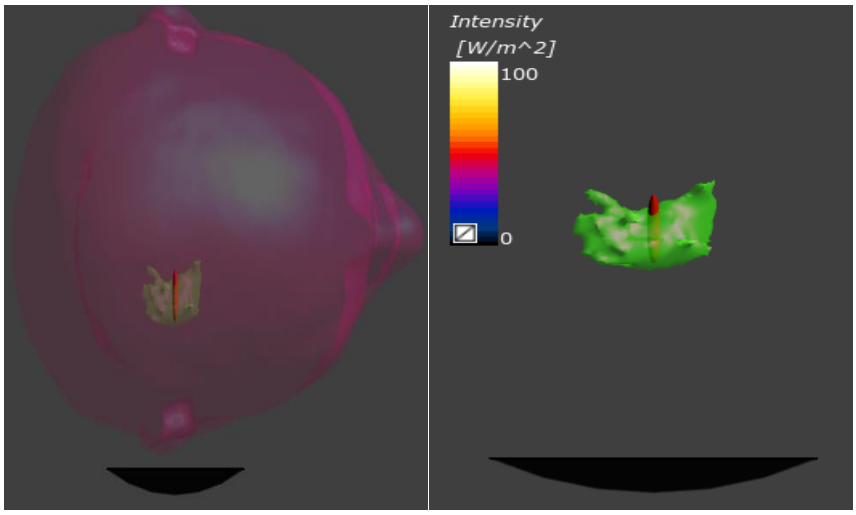

Figure 4-5 Ultrasound propagation with optimisation transducer and volume intersection between beam and hippocampus (red: beam profile, green: hippocampus).

4.3.2 Optimised the transducer

Table 4-3 shows that the beam overlap parameter decreased to 77.84% from 79.75% with ultrasound propagation in the human head model. In order to increase the volume intersection at the FWHM region between the hippocampus and generated ultrasound beam at half the maximum intensity threshold, The ultrasound transducer was optimized to simulate acoustic wave propagation through a three-dimensional human head model. The transducer had a centre frequency of 0.5 MHz, a curvature radius of

85 mm, and an aperture width of 90 mm. The pressure amplitude was adapted to 1.63 kPa, which was used to reach the target intensity at 100 W/m^2 in the hippocampus. The adapted parameters were used to simulate ultrasound wave propagation in a water tank and a 3D human head model. Table 4-4 compares the simulation results using the optimised ultrasound transducer. The results exhibit an increase of 10% in the beam overlap parameter and a decrease of 38% in the target overlap parameter. Figure 4-5 shows the ultrasound propagation with an optimisation transducer, and the target volume intersects with the hippocampus. The adapted ultrasound transducer is used for sensitivity analysis in the following works.

Table 4-4 FWHM quantification of the detailed human head model

	Free water	The highly detailed human head model
Major axis (mm)	15.40	20.40
Minor axis (mm)	2.60	1.83
Target overlap (%)	1.88	2.36
Beam overlap (%)	97.30	85.65

4.3.3 Simulations with different angles

The adapted SEFT was placed over the 3D human head model at the left. Changes to the deflection angles were trialled to examine the change of pressure, intensity, beam overlap parameter, and target overlap parameter. The basic configuration is with maximum intensity, pressure, target overlap parameter and beam overlap parameter of 101 W/m^2, 1.69 kPa, 2.36% and 85.65%, respectively. The deflection angles of ultrasound varied from -30 to +30 degrees, and the direction of deflection was adjusted in two ways, from down to up in the XZ plane and from right to left in the YZ plane (Figure 4-7). In the vertical direction, the maximum intensity varied from around 40 W/m^2 to 120 W/m^2. In the transverse direction, the intensity changed from 70 W/m^2 to 120 W/m^2. Figure 4-6 (a) shows that the angles vary from -5 to +5 degrees, and the error of intensity attenuation is less

than 5%. The pressure changes illustrated in Figure 4-6 (b) are at ±5% when the deflection angles vary between ±5 degrees. The beam overlap parameter and target overlap parameter in Figure 4-6 (c) and (d), do not have different deflection angles. In this figure, the target overlap parameter decreases from around 3.7% to 0.5% in both the vertical and transverse directions. The beam overlap parameters are 60% and 78% in the vertical and transverse directions respectively when deflection angles are at -30 degrees. The beam overlap parameters in two directions have a similar change as deflection angles increase to +30 degrees from -30 degrees. Overall, the errors of both target overlap parameter and beam overlap parameter attenuation are less than 5% when the deflection angles change between -10 and +10 degrees.

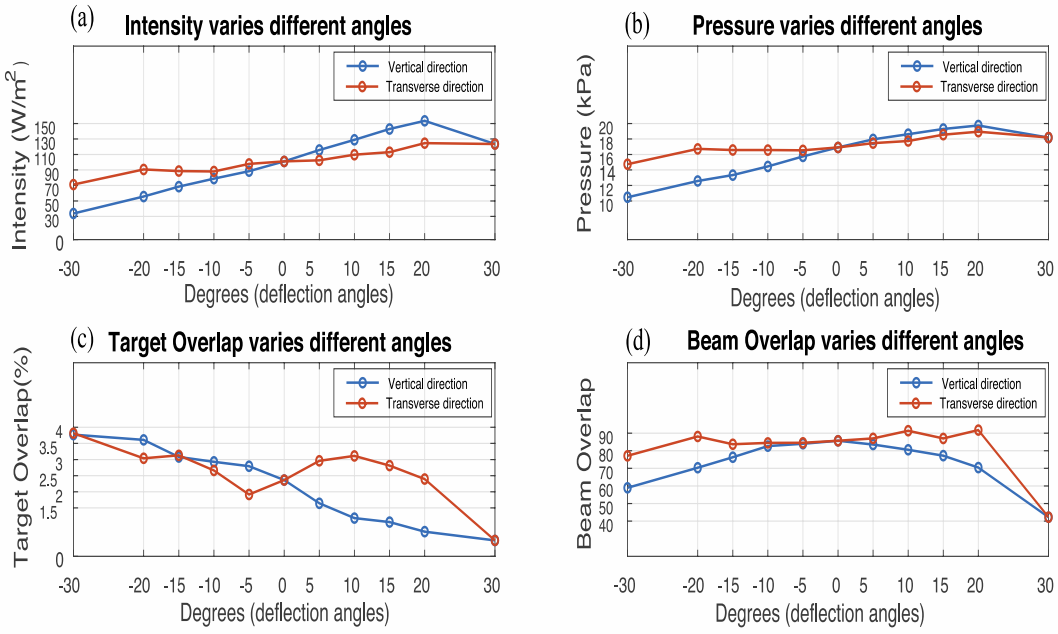

Figure 4-6 Sensitivity effect on changing deflection angles in both vertical and transverse direction for intensity (a), pressure (b), target overlap (c), and beam overlap (d).

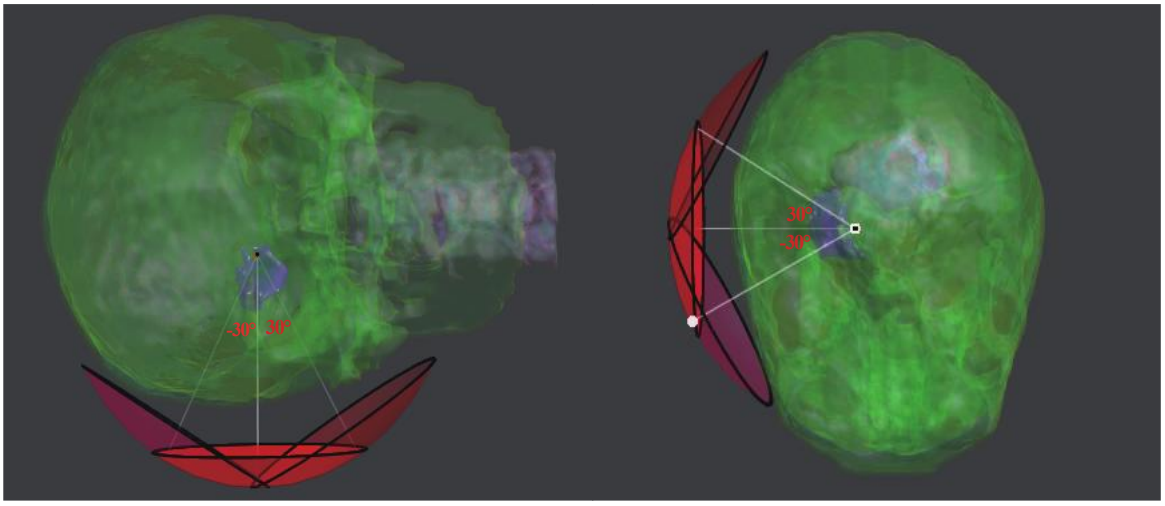

Figure 4-7 Two ways of adjusting deflection angles of transducers ranged from -30° to +30°. (a) Deflection angel changes in YZ plane, (b) Deflection angel changes in XZ plane

4.3.4 SEFT placements

The first placement of SEFT was at the left side of the head (see Figure 4-1 (a)), which is regarded as the acoustic window, the thinnest and weakest part of the skull. Following the identification of the location of the hippocampus in the brain, the next two simulation positions of the SEFT were placed coaxially with the hippocampus, 15 mm from the surface of the scalp. It is common that the distance between the hippocampus and SEFTs is different. In order to ensure the generated beam from the transducer could arrive at the target region through the skull and the maximum intensity could reach 100 W/m^2, the customised three SEFTs with corresponding curvature and aperture were developed (the details are provided in Table 4-5).

From Table 4-5, it can be seen that the maximum pressure changed and increased to 18.02 MPa when the placement of SEFT moved from the left to the back, with a corresponding increase in the size of the customised transducer. Table 4-5 also shows that the beam overlap parameter has a clear change. It is 68.48% and 52.77% at the top and back positions compared with 85.86% at the position of the acoustic window, respectively. It is also apparent that the major axis and minor axis of FWHM increase with the size of SEFT.

Table 4-5 Details of customised SEFT and corresponding results at three placements

	Left (Heterogeneous Brain)	Left (Homogeneous Brain)	Top	Back
Curvature (mm)	85	85	135	130
Aperture (mm)	90	90	100	120
Maximum intensity (W/m^2)	101.0	100.6	100.1	100.3
Maximum pressure (MPa)	16.91	17.00	17.81	18.02
Target overlap (%)	2.36	2.66	2.18	2.88
Beam overlap (%)	85.65	85.86	68.48	52.77
Major axis (mm)	10.35	10.52	11.67	23.81
Minor axis (mm)	1.83	1.83	3.39	2.81

4.3.5 Analysis of acoustic properties of brain tissues

Skull:

In the simulation, the adapted ultrasound transducer has a standard configuration of 81 Np/m attenuation, 2300 m/s sound speed, and 1912 kg/m^3 density. The variation of skull attenuation measured from -70% to +70% (from 25 Np/m to 140 Np/m), the sound speed of the skull varied from -20% to +20% (from 1840 m/s to 2760 m/s), and the density of the skull fell within a range of -15% to +15% (1625 kg/m3 to 2199 kg/m^3). It should be noted that only one parameter was varied each time and the others were assigned with standard configurations as references.

Figure 4-8 demonstrates the relative effect of the sensitivity analysis, which reflects the maximum intensity and pressure changes that occur when there are changes in the skull parameters. For example, to investigate the changes of maximum intensity and pressure in attenuation, velocity and density were set as standard values and the skull attenuation was set from -70% to +70%, as shown in Figure 4-8 (a). In this figure, the first row is the variations in maximum intensity and pressure when corresponding

parameter changes occur. The second row is the target overlap parameter and the beam overlap parameter changes over different variations. The results show that when attenuation changes are greater than 60% and velocity changes are greater than 10%, the beam overlap parameter and target overlap parameter vary over 5%, which means the volume size of the ultrasound beam intersection with the hippocampus area is changed significantly. The maximum intensity changes were 31%, 50% and 3.8% for the attenuation, sound speed, and density, respectively. The maximum pressure variations corresponding to the attenuation, sound speed, and density were 10.5%, 22% and 2%, respectively. In order to satisfy the 5% error metrics, the variations for the attenuation should range from +4% to -4%, the velocity should range from +2.5% to -2.5% and the density should range from +15% to -15%. For the pressure, the corresponding range for attenuation, sound speed, and density were from +7.5% to -7.5%, +5% to -5%, and +15% to -15%, respectively. It must be noted that those values are for heterogeneous brain model simulations and the results are similar to homogeneous brain model simulations.

The results of the beam overlap parameter and target overlap parameter for the heterogeneous and homogeneous brain models did not have significant differences. The changes in the target and beam overlap parameters show that the focal volume above half the maximum threshold did not have a significant change. The maximum target overlap parameter corresponding to attenuation, sound speed, and density were 5.3%, 2.3% and 1.1%, respectively, and for the beam overlap parameter, they were 0.3%, 6% and 0.5%, respectively. In order to make the target overlap parameter less than a 5 % error metric, the range should be from +60% to -70%, and from +5 to -17% for the attenuation and velocity variations. The density change in the whole range did not go beyond 5%. For the beam overlap parameter, the corresponding values were from +70% to -70%, from +12% to -17%, and from +15% to -15% for the attenuation, velocity, and density, respectively.

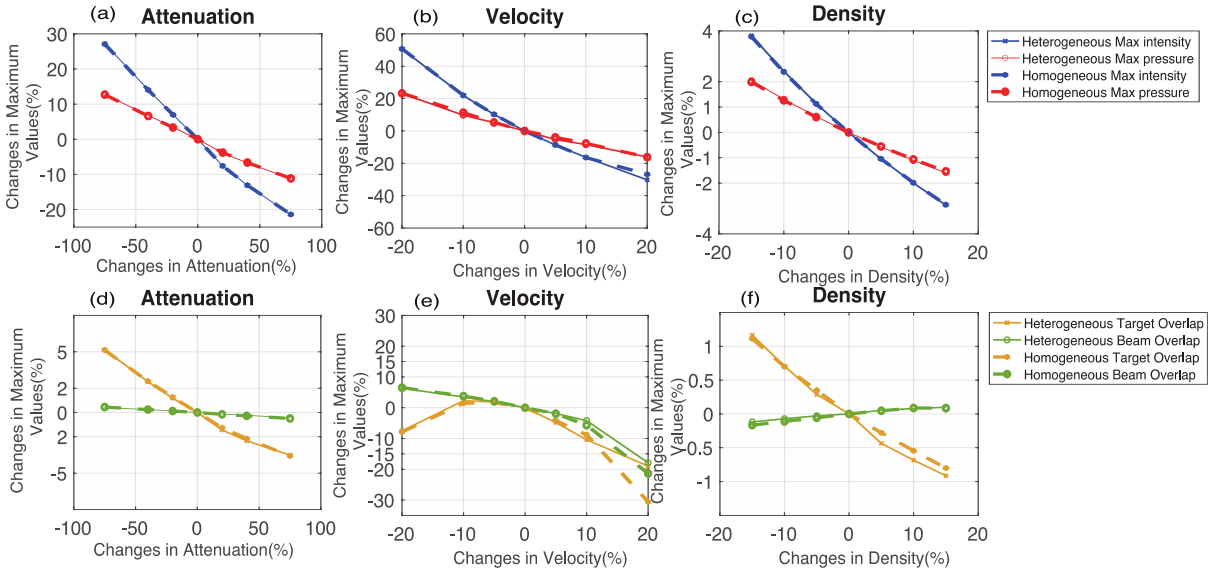

Figure 4-8 Relative change effect in maximum intensity, maximum pressure, target overlap, and beam overlap with different skull parameters.

Brain, Muscle, and Scalp:

With a standard configuration of attenuation at 0.92 Np/m, sound speed at 1550 m/s and density at 1030 kg/m^3, Fig. 10 shows the results of the relative changes in heterogeneous brain tissues (GM and WM) and homogeneous brain tissues when the attenuation, velocity, and density are varied.

Compared with the results of the heterogeneous brain model, the maximum intensity variations of the attenuation, sound speed, and density increased to 3.9%, 18.8% and 20.9% from 0.9%, 9.7% and 18.5%, respectively. Figure 4-9 shows that the maximum intensity and pressure led to a significant change in velocity. When the variation between +15% and -15% was used, the corresponding value for the attenuation did not exceed the 5% error metric. This was also the case for the maximum pressure variations in density for both the heterogeneous and homogeneous brain model simulations. In order to obtain a less 5% error metric, the maximum intensity in density should be at a range of +5% to -5%. The variations for the sound speed in heterogeneous and homogeneous brain models had a

slight difference; the variation of maximum intensity in the homogeneous brain model was greater than the values in the heterogeneous brain model.

The second row in Figure 4-9 demonstrates the changes in the target overlap parameter and beam overlap parameter when the value of attenuation, sound speed and density are varied. For the attenuation and density, the change for both the target overlap parameter and beam overlap parameter was less than 2.5%, and these results are within the 5% error metrics. There was a significant change in the sound speed when the changes in velocity was beyond ±5%, both in the heterogeneous and homogeneous brain models.

Figure 4-10 and Figure 4-11 show the results of the relative changes in maximum intensity, pressure, target overlap parameter, and beam overlap parameter when the value of the attenuation, sound speed, and density are varied, with the standard configuration 3.4 Np/m and 10.6 Np/m, 1558 m/s and 1624 m/s, 1090 kg/m^3 and 1109 kg/m^3 for muscle and scalp, respectively. The variation was from +15% to -15%, based on the standard configurations. It is worth noting that variations in muscle and scalp between heterogeneous and homogeneous brain models do not have obvious changes. For the attenuation and density, the parameter changes resulted in variations that were less than the 5% in error metrics for maximum intensity, maximum pressure, target overlap parameter, and beam overlap parameter. For the muscle of the heterogeneous brain model, to obtain the maximum intensity error of less than 5%, the sound speed variation range should be from +15% to -5%, and the range of the beam overlap parameter and target overlap parameter for the sound speed variation should be from +7.5% to -7.5% and +2% to -2%, respectively. For the scalp of the heterogeneous brain model, the maximum intensity and pressure of the variations were around 16% and 4.8% for the sound speed variation, when the parameters ranged from +6.5% to -3.5% and +15% to -9.5% for the maximum intensity and pressure, respectively. The

parameter changes for target overlap parameter and beam overlap parameter should range from +1% to -1% and +3% to -3%, respectively, in order to obtain variations less than 5%.

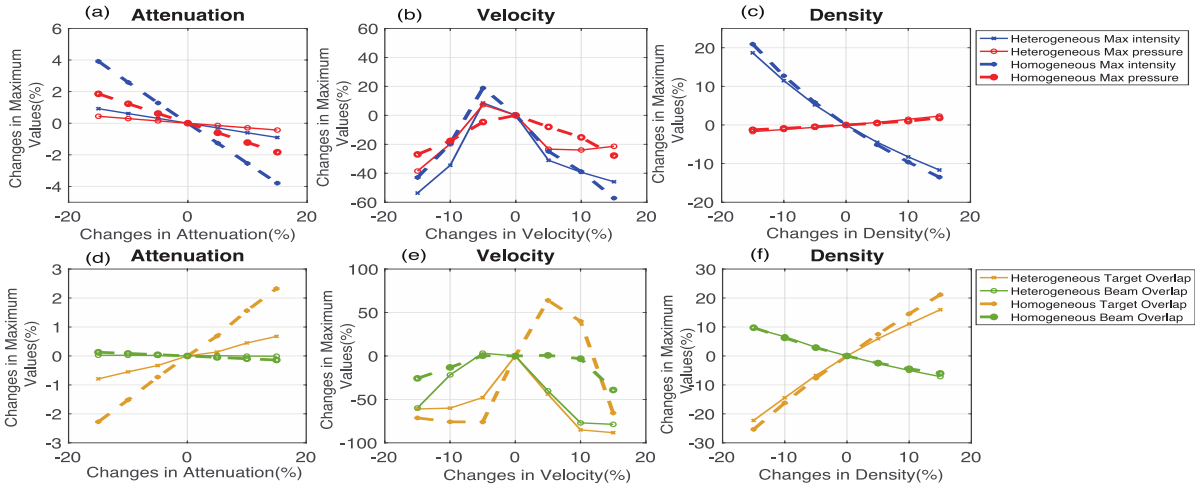

Figure 4-9 Relative change effect in maximum intensity, maximum pressure, target overlap and beam overlap with different brain parameters.

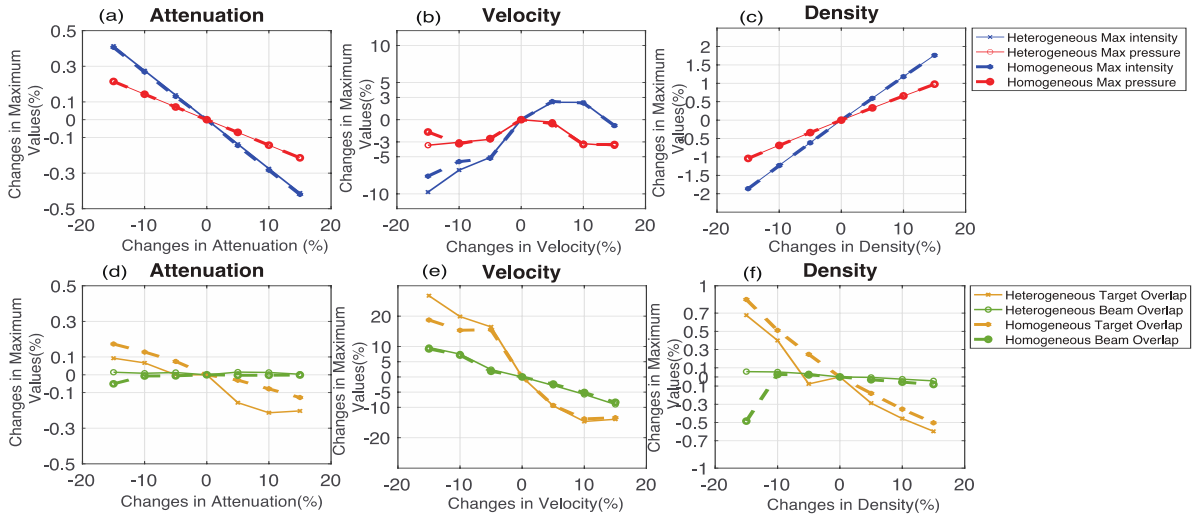

Figure 4-10 Relative change effect in maximum intensity, maximum pressure, target overlap, and beam overlap with different muscle parameters.

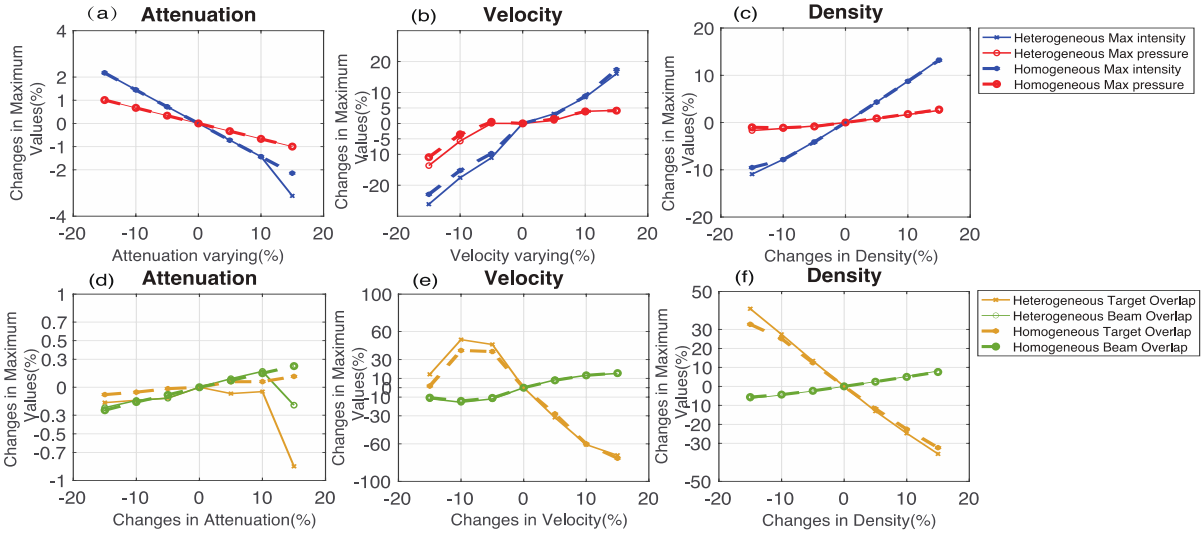

Figure 4-11 Relative change effect in maximum intensity, maximum pressure, target overlap, and beam overlap with different scalp parameters.

4.4 Discussion and evaluation

The transcranial ultrasound wave propagation and ultrasonic transducers are two key factors in the procedures of brain stimulation by tFUS. In this study, a high-resolution 3D human head model was generated, and a set of customised SEFT and WLE acoustic equations were used to simulate ultrasound wave propagation through the skull to deposit the low-intensity energy in the deeper brain structure, the hippocampus. The sensitivity analysis of the skull, scalp, muscle, GM, and WM was conducted by varying the parameters of brain tissues' attenuation, sound speed, and density to investigate the impact of the properties of brain tissues on neuromodulation. In addition, the beam overlap parameter and target overlap parameter describing the volume above the half maximum intensity threshold were calculated to quantify the model response of ultrasound. To validate the accuracy of the numerical model, a water tank-based simulation was first conducted. The results were compared with empirical measurements and computational simulation outcomes [153]. The comparisons demonstrate that while the numerical simulation results in this study are slightly different from empirical measurements (the maximum pressure and intensity changed 9.6% and 0.84%, respectively), they are almost the same as the

computational peer outcomes (the maximum pressure and intensity changed 0% and 0.04%), which has been summarised in Table 4-2.

4.4.1 Skull effect on wave propagation and its heterogeneity

Legon et al. [82] used a calibrated needle-type hydrophone to characterize the acoustic intensity profile of the waveform. Their measurements showed that the spatial-peak pulse-average intensity dropped by approximately fourfold when tFUS was transmitted through the skull. Compared with the simulation results in a water tank, the attenuations of maximum pressure and intensity were 81.96% and 56.63%, respectively. Studies by Mueller et al. and Deffieus and Konofagou [153, 160] found the attenuations of maximum intensity and pressure are 75.2% and 42%-88%, respectively. This study's attenuation of maximum pressure and intensity was also close to the values obtained from these previous studies.

In previous research, Aubry et al. [168] derived bone porosity maps from high-resolution CT images linked to the Hounsfield maps. The skull's acoustic properties (density, speed and absorption coefficient) were deduced from porosity maps. They used the inner of the heterogeneous skull, with a full 3D finite differences code, to achieve a non-invasive adaptive focusing simulation. Marquet et al. [169] used the same method for calculating the acoustic properties of the skull to study the protocol of tFUS.

The individual tissues of the human head model were regarded as homogeneous for ultrasound wave propagation. Thus, the acoustic properties were assigned to corresponding brain structures. However, Kyriakou et al. [170] reported that the skull's heterogeneous nature and acoustic characteristic induced energy attenuation and phase aberrations, which might impact distortion and shift of the focal spot area. Kyriakou et al. [159] used distance-based phase corrections (DPC) and simulation-based phase corrections (SPC) methods to investigate the impact of phase

aberration. In their study, the results from the heterogeneous and homogeneous models indicated that the same shift at 0.5 mm and focal spot volumes at 50 mm^3 were produced by the SPC method. Kyriakou et al. [159] also used a WLE equation discretized by the 3D FDTD method, and this technique was used in our study. It is, therefore, feasible to use the volume discretization method for assigning heterogeneous material properties, including density, speed of sound, and attenuation coefficient. In addition, the feasibility of this type of ultrasound wave propagation has been validated in [159].

4.4.2 Sensitivity effect on brain model

The acoustic medium properties, attenuation, density, and sound speed were used to examine the sensitivity of brain tissues. The thickness of the skull has great interpersonal differences, which might have influenced the ability of penetration, impedance, and absorption of the ultrasound propagation. The maximum intensity of the variations in acoustic properties was more sensitive than the maximum pressure (since the intensity is proportional to the square of the pressure). Also, the trend in sound speed had a more significant change than the attenuation and density when compared to the variation trend of maximum pressure and intensity in different brain tissues. For an accurate brain model stimulation (with a change in the maximum value of less than 5%), attenuation, sound speed, and density change of the skull should be smaller than 1.75%, 1.14% and 15%, respectively. Only the variations in the velocity and density of the scalp influenced the maximum intensity. The change should be between -2.25% and 2.58% for the velocity and less than 6.25% for the density. The muscle variation did not cause a significant change (within the 5% error metric) when ±15% parameter changes were applied to the attenuation, sound speed, and density. For GM and WM, attenuation variation did not have a significant impact on the parameters. The variation change of velocity and density should therefore be within the range of -6.57% and 0.81%, -4.8% and 5.6%, respectively.

The customised transducer was developed to simulate transcranial acoustic wave propagation through homogeneous and heterogeneous brain models. Details of the transducer are listed in Table 4-5. Also, the tissue property of the homogeneous brain was assigned as the brain property in Table 3-1. Based on the sensitivity analysis results of the heterogeneous and homogeneous brain models shown in Figure 4-8 to Figure 4-11, the variations do not have apparent changes in maximum intensity, maximum pressure, target overlap parameter, and beam overlap parameter in the skull, muscle, and scalp. For the brain sensitivity analysis, the variations of intensity, pressure, beam, and target overlap parameter slightly changed in attenuation (within the 5% error metric). Meanwhile, the heterogeneous brain model had the same trend of density variations as the homogeneous brain model, and this means the variation differences between these two models can be disregarded. For the velocity analysis, the maximum intensity variations increased from 8.54% in the heterogeneous brain model to 18.84% in the homogeneous brain model. In contrast, the maximum pressure variations decreased from 7.29% in the heterogeneous brain model to 0% in the homogeneous brain model. Another significant change between the two brain models was the beam overlap parameter. The beam overlap parameter in the heterogeneous brain model increased from around -70% to +60% and then decreased to -60% when the velocity was between -15% to +15%. However, the beam overlap parameter variations in the homogeneous brain model slightly increased from -25% to 0% and decreased to -40%.

4.4.3 Deflection angles and transducer effect

Several MRI-guided brain focused ultrasound applications [171, 172] reported that it was hard to avoid slight shaking during the treatment, and the small displacement may lead to a significant difference in energy deposited and target volume shift. This study applied ±30 degrees of deflection angles in the vertical and transverse directions. As a result, the

maximum intensity change was from around 40 W/m^2 to 120 W/m^2. Within around ±5 degrees change in both transverse and vertical directions, the percentage change of maximum intensity was less than 5% in this study. The maximum pressure change in the vertical direction was faster than in the transverse direction. When the angle changes in the transverse direction were between -20 to +10 degrees, the maximum pressure change was less than 5%, and the variation was from +4 degrees to -4 degrees in the vertical direction. The slight change in ultrasound transducer deflection angles had a significant effect on both the target overlap parameter and beam overlap parameter, which had variations between around ±2% and between around +10% and -60% for the target overlap parameter and beam overlap parameter, respectively. MRI-guided, as a technical auxiliary function, plays an important role in providing accurate location information in the brain. As evidenced by the above numerical sensitivity analyses, choosing and placing the ultrasound transducer at a suitable position over the brain skull is important. Also, the effect of the target overlap parameter and beam overlap parameters cannot be ignored. In this study, target overlap and beam overlap parameters were proposed as two indexes to precisely describe the intersection volume of the generated beam above half threshold intensity value and the target region. The target and beam overlap parameter changed from 3.76% and 77.84% to 2.36% and 85.65% (and 97.3% in a water tank), respectively, after the optimisation transducer was used.

The size of the transducer, operating frequency and the placement of the transducer are considered the main factors affecting the ultrasound beam transmission through the brain. Three customised transducers in different positions were therefore proposed in this study to examine and simulate the process of transcranial focused ultrasound propagation. This study found the beam overlap parameter was 52.77% when the customised SEFT was placed at the back side of the brain (Figure 4-1 (c)), which is smaller than 68.48% and 85.65% when the SEFT was placed at the top (Figure 4-1

(a)) and left side (Figure 4-1 (b)) of the brain, respectively. From these findings, it can be concluded that the customised ultrasound transducers with the proper size and placement are important factors for precise applications of tFUS. If the ultrasound wave propagation is unexpectedly low or high, the energy deposition in the target brain region would be lower or higher than anticipated.

4.4.4 Thermal effect

The temperature induced in tissues is due to the attenuation of ultrasonic energy and absorption of the underlying tissues in ultrasonic wave propagation. Some research [173, 174] investigated and reviewed ultrasound neuromodulation's mechanisms and safety, including thermal effect. Van Rhoon et al. [175] discussed thresholds for thermal damage and safety of the thermal dose and suggested guidelines for the thermal thresholds for human skin, muscle, fat and bone.

Constants et al. [176] investigated the temperature change and thermal doses of ultrasonic neurostimulation based on five studies settings [53, 156, 177-179] in the rodent brain. The maximum temperature elevation was lower than 1 ℃ (thermal rise ranging from 0.002 ℃ to 0.8 ℃) when the studies setting [53, 156, 177, 178] (the operating frequency was between 0.32 MHz and 5 MHz and the total sonication time was from 80 ms to 20 min) was used. However, Kamimura et al [179] used an operating frequency set at 1.9 MHz and the sonication time was 20s. The maximum temperature reached 7 ℃ near the skull and 1.3 ℃ at the focal spot. In some transcranial neurostimulation studies the choice of aggressive acoustic parameters might lead to significant thermal.

In a study by Mueller et al. [153], the authors used an operating frequency of 0.5 MHz for a 4-layers brain model simulation. The skull absorbed most of the heat energy due to the high attenuation coefficient. The temperature

change was only 0.16 ℃. The temperature change in CSF was only 0.03 ℃ and the energy deposition in the brain tissue was 0.00427 ℃. It is noted that in [153], the maximum intensity was around 60 kW/m^2, which is two orders of magnitude higher than in this study. Therefore, in this study, the heat transfer at low-intensity FUS can be considered insignificant and thus can be ignored.

4.5 Conclusion

This Chapter shows that customised SEFT based on the high-resolution 3D human head model has the potential to precisely deliver LIFU stimulation in the hippocampus. Ultrasound transducer characteristics, such as the aperture width, curvature radius, position of the transducer, and operating frequency, should be customised for specific individuals to achieve the best treatment outcome. The sensitivity analyses showed that the maximum pressure was less sensitive than the maximum intensity when the characteristics of brain tissues, sound speed, density, and attenuation coefficient were changed. In addition, the target and beam overlap parameters were most affected by the change in sound speed compared with the variation of density and attenuation.

CHAPTER 5: NUMERICAL INVESTIGATION ON FOCUSED ULTRASOUND-MEDIATED BLOOD-BRAIN BARRIER OPENING CHARACTERISED BY THE MECHANICAL INDEX AND CAVITATION INDEX

Drug delivery to subcortical regions in the brain is affected by the BBB, which prevents molecular and cell exchange between circulating blood and brain parenchyma. tFUS with microbubbles as a non-invasive method has been proven to induce BBB opening in targeted areas and facilitate drug delivery. The objective of this Chapter is to numerically investigate how BBB is affected while ultrasound wave propagates through a 3D highly detailed human head model. The MI and the CI, as two metrics that reflect ultrasound-induced BBB disruption, are used to analyse the intracranial fields change. This study shows the impact of the skull and incidence angles ultrasound beam on tFUS-mediated BBB opening using MI/CI metrics and corresponding to the focal spots.

5.1 Introduction

Despite the increasing number of effective drug actions and neurologically active substances, brain diseases, such as CNS disorders and tumours, are still challenging due to the ability of access through the skull and the BBB for therapeutic agent delivery [180-183]. The microenvironment in the CNS is maintained by BBB, which prevents molecule and cell exchange between the circulating blood and brain parenchyma [184]. It is difficult for the therapeutic agent to penetrate BBB, limiting the potential for treating CNS disorders, such as Parkinson's disease and Alzheimer's disease [185, 186]. Some studies have been conducted to improve the efficiency of drug actions by opening the BBB. LIFU and BBB opening with microbubbles are the

safest methods [187]. FUS is a unique technique for non-invasive brain treatment with tumour ablation [188], BBB opening for therapeutic agent delivery [189], and neuromodulation for brain functions [190]. Caudate and putamen, as two representative regions of interest (ROIs), are widely used in preclinical trials, such as rodent and non-human-primate (NHP) experiments [160, 189]. These two ROIs involve brain motor cortex functions related to the application of Parkinson's and Alzheimer's disease treatment [191, 192].

Ultrasound-induced BBB opening in large animals, such as non-human primates (NHP), was performed using a phased-array transducer, mainly at a frequency under 500 kHz [187]. However, phased-array transducers were controlled by complicated electrical drivers, and it was difficult to operate and not portable. Compared with a phased-array transducer, a SEFT was less costly, easy operation and portable for usage, though the skull's penetration efficiency was relatively less. Several studies discussed the feasibility of a SEFT in large animal experiments [160, 189]. Marquet et al. [193] first investigated the feasibility of BBB opening with microbubbles, targeting the visual cortex (V3), the caudate, and the hippocampus in NPH using SEFT when the frequency was 500 kHz. A series of studies, including the safety assessment of BBB opening efficiency, used SEFT with 500 kHz frequency to investigate BBB with microbubble control in NHP [194].

Most studies on BBB opening are currently performed using numerical simulation methods and small animals, such as rats or mice, in vivo before clinical operations [195, 196]. However, the experimental conditions and results are not easily applied directly to clinical trials because of the ultrasonic transmission through the human skull. When the ultrasound wave propagation through a human skull, the attenuation is affected by wave reflection, scattering and energy conversion. Also, the heating of the thermal effect caused by energy deposition was concentrated at the

transmission edge of the skull, and wave reflection and resonance caused by pressure change led to increased trabeculae [197]. Furthermore, skull thickness was a factor that affected the change of ultrasound focal spots by increasing the centre frequency of the transducers [112]. Thus, the skull effect and the difference between small animals and humans are the main reasons it is difficult to propose optimal ultrasonic energy and corresponding focal spot for clinical trials.

Several preclinical studies have investigated the effect of different FUS parameters on FUS-induced BBB opening, such as ultrasonic pressure, central frequency, burst length, pulse repetition frequency, duration and microbubble dose [116, 122, 198]. Furthermore, both the mechanical index (defined as the peak negative acoustic pressure over the square root of the frequency, i.e., MI = $P/\sqrt{f}$, P in MPa and f in MHz) and cavitation index (defined as the acoustic pressure over the frequency, i.e., CI = P/f) have been proposed to evaluate the performance of the BBB opening volume and drug delivery efficiency. McDannold et al. studied the relationship between MI and FUS-induced BBB opening by comparing the change of signal intensity in contrast-enhanced MRI [118]. They found that the thresholds related to MI indicate the FUS-induced BBB opening. Chu et al. reported a high correlation between drug delivery efficiency and both MI and CI index, and MI had a higher correlation than CI [199].

5.2 Methods

The work in this chapter was based on a highly detailed 3D human head model. Two SEFTs were customised to deliver focused ultrasound to the ROIs, including putamen and caudate, in the deep region of the brain. After that, the density, attenuation and sound speed were changed to evaluate the influence of the skull parameters on the MI and CI. In addition, the incidence angles were changed to simulate the ultrasonic wave propagations through the interface between extracranial and intracranial

and investigate the relationship between the MI, CI and incidence angles. A highly detailed human head model with 134 geometries was constructed first (details see Section 3.1.2). Also, custom-designed transducer configurations were proposed to simulate ultrasonic wave propagation through the 3D human head model and target the desired regions. Then, the effects of different frequencies, skulls, and incidence angles on MI and CI were tested and analysed.

5.2.1 Transducer design and target brain regions

A customized transducer with a curvature radius of 100 mm was proposed in the putamen study. An f-number of 1.5 (aperture radius of 65 mm) was chosen at centre frequencies of 350 kHz and 500 kHz. In the other target brain region, the caudate nucleus, the transducer was developed with a curvature radius of 95 mm and an aperture radius of 80 mm (f-number of 1.2). Further details of the transducers are provided in Table 5-1. Due to the position displacement between the target brain regions and two transducers, the properties of the transducers were customized to provide focal spots with enough focal area for the desired regions. Additionally, ultrasonic wave propagation could have enough pressure at the target regions to open the BBB.

The proposed SEFTs are applied to focus on putamen and caudate (in Figure 5-1 (b) and (c), and the dimensions of these two target regions are listed in Table 5-2), which are clinically relevant targets involved in Alzheimer's and Parkinson's disease [185, 191, 192]. Also, these two regions have been widely used in preclinical non-human primates and rodent BBB experiments [160, 189, 200].

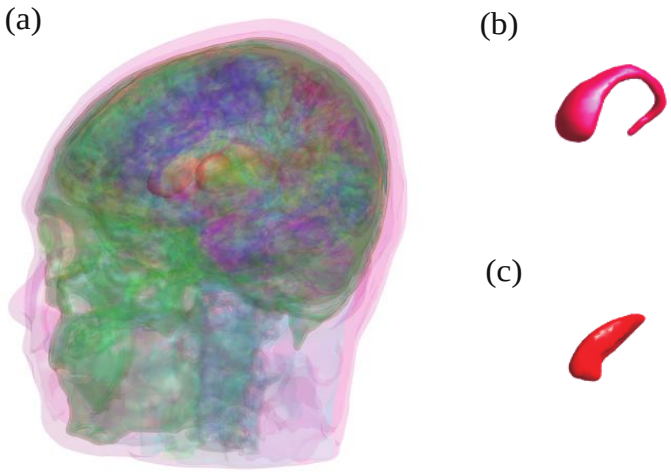

Figure 5-1 (a) 3D detailed human head model contains 134 geometries. (b) Left caudate nucleus. (c) Left putamen

Table 5-1 Transducer parameters

	Putamen study	Caudate nucleus study
Curvature radius (mm)	100	95
Aperture width (mm)	65	80
Source amplitude (kPa)	85	60

Table 5-2 Dimension of the target regions

	Left Putamen	Left Caudate nucleus
Length (mm)	42.1	62.5
Height (mm)	23.5	37.5
Width (mm)	17.0	31.3
Total Volume (mm^3)	4422.9	7742.2

5.2.2 Governing equation and validation

Numerical simulation of ultrasound wave propagation through the 3D detailed brain model was conducted by the commercial software package Sim4Life [201]. Non-linear variants based on the WLE were used to generate full-wave ultrasound propagation [141, 158]. The WLE was discretised using 3D FDTD method (see [159] for more details), as this can have a positive effect on assigning heterogeneous material properties

(density, sound of speed, attenuation coefficient and impedance). A validation experiment in a water tank was based on a previous SEFT model, and it was regarded as a point of reference [153, 166]. Muller et al. used customised SEFT with a diameter and a focal length of 30 mm, and a centre frequency of 0.5 MHz. The transducer used in Sim4Life had the same centre frequency, curvature radius at 50 mm, aperture width at 30 mm, and source amplitude at 0.145 MPa. Further detail on transducer geometry and validation experiment results can be found in our previous study [202].

5.2.3 Parameters for the performance of BBB opening

Holland et al. demonstrated that the minimum amplitude of acoustic pressure for bubble growth was determined by the initial size of the nucleus [203]. Then, Apfel and Holland developed MI, defined as peak negative acoustic pressure (in MPa) over the square root of the frequency (in MHz), to gauge ultrasound-induced inertial cavitation of bubbles [204]. Also, CI is defined as peak negative acoustic pressure (in MPa) over frequency (in MHz) to gauge the likelihood of subharmonic emissions as the scale of stable cavitation [205]. McDannold et al. found a correlation between MI and FUS-induced BBB opening and reported that the threshold of BBB opening was constantly described by MI [118]. In addition, the beam and target overlap parameters were used to evaluate the spatial resolutions of the ultrasound beam profiles in the deeper brain regions. The two parameters quantitatively describe the relationships between the expected focal spot areas and the targeted structures.

5.2.4 Skull effect on the MI and CI

Some studies have measured the acoustic properties of the human skull, but the measured properties demonstrated some variations [161, 162]. Also, the geometry of the anatomical human head model has slight interpersonal differences. As the domain barrier to acoustic propagation due to its high attenuation, refraction, and dispersion, the skull determines the intracranial pressure. Thus, sensitivity research was conducted to

investigate the impact of skull properties on MI and CI. The skull's acoustic properties, such as density, speed of sound, and attenuation coefficient, varied linearly based on the baseline's skull properties in Table 3-1.

5.2.5 Incidence beam angles

Incidence angles of ultrasound wave propagation through the skull may affect neighbouring areas and vascularised regions around the target regions because of the complexity of the human head model and interpersonal differences. Thus, the accuracy of targeting desired regions and MI and CI variations related to the BBB opening have to be optimised and customised before clinical trials. Figure 5-2 demonstrates an example of the deflection angles of the transducer changed when ultrasound wave propagation through the head model.

The ultrasound wave propagation through the human head model at 0.5 MHz targeting putamen and caudate was employed as the default configurations to compare the results with varied deflection angles at 3°, 5°, 7° and 10°. Eight cases were studied at each deflection angle, and the direction was adjusted randomly in eight ways in a three-dimension coordinate.

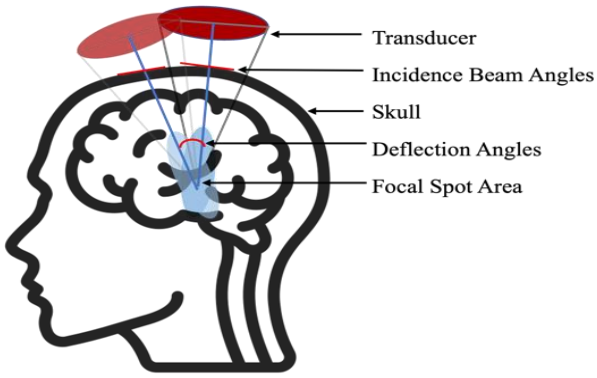

Figure 5-2 Deflection angles of transducer changed when ultrasound wave propagation through the head model

5.3 Results and analysis

5.3.1 tFUS propagation in a 3D detailed human head model

Table 5-3 tFUS propagation in human head model

	Putamen Study	Caudate Study
Centre Frequency (MHz)	0.50	0.50
Source Amplitude (kPa)	85.0	60.0
Peak Intensity (W/cm^2)	7.55	6.57
Peak Pressure (MPa)	0.48	0.46
MI	0.68	0.65
CI	0.96	0.92
Major Axis (mm)	31.3	20.8
Minor Axis (mm)	3.42	2.98
FWHM (mm^3)	308	127
Target Overlap (%)	5.53	1.51
Beam Overlap (%)	79.4	91.87

In order to generate an FWHM beam profile in the brain's target sub-cortical regions (putamen and caudate) and the suitable range of intracranial peak pressure to open BBB, the customised ultrasound transducers were developed to simulate focused ultrasound wave propagation through a 3D human head model. In the putamen study, the transducer had a centre frequency of 0.5 MHz with a curvature radius of 100 mm and an aperture width of 65 mm. The source amplitude was adapted to 85 kPa, which was used to have peak pressure at 0.48 MPa at the putamen BBB opening. The customised transducer with a centre frequency of 0.5 MHz, a curvature radius of 95 mm and an aperture width of 80 mm was used in the caudate study. In order to have a similar peak pressure at the desired region, the source amplitude was adapted to 60 kPa. The details of transducers were provided in Table 5-1, and beam profiles with corresponding MI and CI were listed in Table 5-3. The transducers with centre frequencies at 0.35 MHz and 0.5 MHz were used to compare the frequency effect on beam profiles, MI and CI. The adapted ultrasound transducer at 0.5 MHz in the putamen

and caudate study is the standard case of configurations in the following works.

5.3.2 *Different frequencies effect on MI, CI, and FWHM*

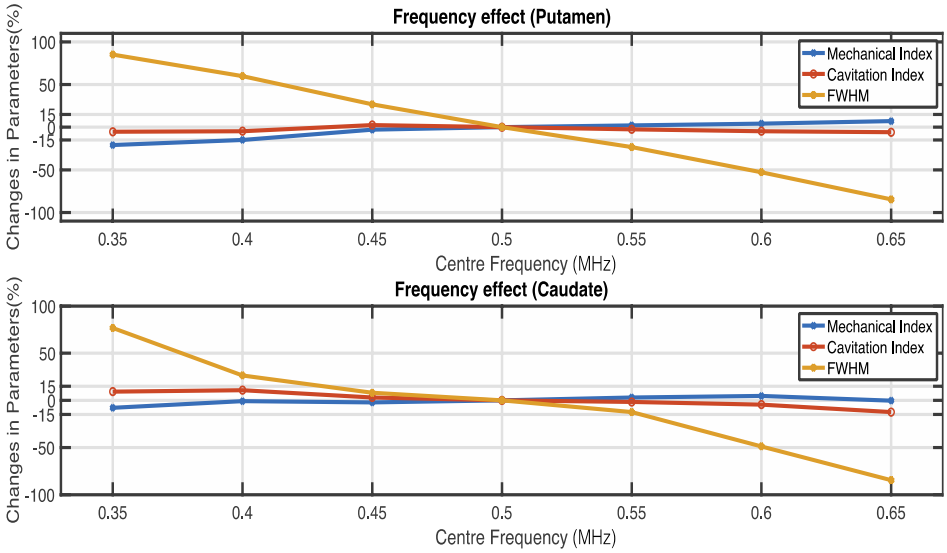

Figure 5-3 Frequency effect on MI, CI and FWHM

The customised SEFT at 0.5 MHz as standard configuration was used to compare the frequency effect on MI, CI, and FWHM. The standard configurations, including putamen and caudate, were provided in Table 5-3, and the centre frequency of ultrasound varied from 0.35 MHz to 0.65 MHz in Figure 5-3. In the putamen study, the percentage change of MI was from -21% (at 0.35 MHz) to +7% (at 0.65 MHz), compared with the MI was 0.65 (at 0.5 MHz). However, the overall trend for CI increased slowly, and it increased from -5.4% (at 0.35 MHz) to 0 (at 0.5 MHz), then decreased to -6% (at 0.65 MHz). Compared with MI changes in the putamen, the percentage change of MI did not have a significant change in the caudate study, and it was increased from -7.8% (at 0.35 MHz) to -0.3% (at 0.65 MHz). Meanwhile, the CI had the opposite trend, which decreased from +9.3% (at 0.35MHz) to -12.4% (at 0.65 MHz). The numerical results by SEFT showed that a higher frequency (0.65 MHz) has a better spatial resolution than relatively lower frequencies (0.35 MHz) in axial, later directions, and volume of FWHM. The spatial resolution in axial and lateral directions increased by around 73.5% and 37.6%, and the volume of FWHM

decreased from 570 mm^3 to 47.3 mm^3. Meanwhile, the axial and lateral resolution increased by 84% and 47%, and the volume of FWHM decreased from 225 mm^3 to 19.6 mm^3.

5.3.3 Skull effect on MI, CI, and focusing area

a. Targeting of the Putamen at 0.35 MHz and 0.5 MHz

The customised SEFT was used with a standard skull configuration (attenuation, sound speed and attenuation provided in Table 5-1). The variation of skull attenuation measured from -70% to +70%, the sound speed of the skull varied from -15% to +15%, and the density of the skull varied from -15% to +15%. One parameter was changed, and the others were assigned as default configurations in these works.

The centre frequencies at 0.35 MHz and 0.5 MHz were investigated using the same transducer parameters in Table 5-2. The results of the simulations are compared in Figure 5-4. To investigate the effect of skull attenuation on MI and CI when targeting the putamen, sound speed and density were set as default values, and the skull attenuation was set from -70% to +70% varied, as shown in Figure 5-4 (a). MI and CI had a similar change in varied attenuation compared with two different centre frequencies. Meanwhile, the relationship between the focused volume and the target region was also studied, including target overlap and beam overlap. Both target and beam overlap did not significantly change (within $\pm$5%) at 0.35 MHz and 0.5 MHz in Figure 5-4 (b). The changes of MI and CI while the sound speed of skull parameters was changed had a similar trend. The MI and CI decreased with increasing velocity and density (Figure 5-4 (c) and Figure 5-4 (e)) at both 0.35 MHz and 0.5 MHz. When the centre frequency was at 0.5 MHz, the maximum relative variations for the MI and CI were equal to 19.4%, 17.9% and 4.8% for the attenuation, sound speed and density, respectively. For the frequency at 0.35 MHz, these values became 15.72%, 18.25% and 5.0%, respectively. In addition, the percentage of target overlap and beam overlap did not change significantly within $\pm$10% of the range of the skull

parameters, such as sound speed and density (Figure 5-4 (d) and Figure 5-4 (f)). When the centre frequency was at 0.5 MHz, the maximum relative variations for the target overlap and beam overlap were equal to -0.36% and -0.78%, +6.7% and -22%, -0.2% and -0.03% for the attenuation, sound speed and the density, respectively. For the frequency at 0.35 MHz, these values changed to -0.7% and -0.7%, -7.8% and -17.7%, -0.12% and -0.4%, respectively.

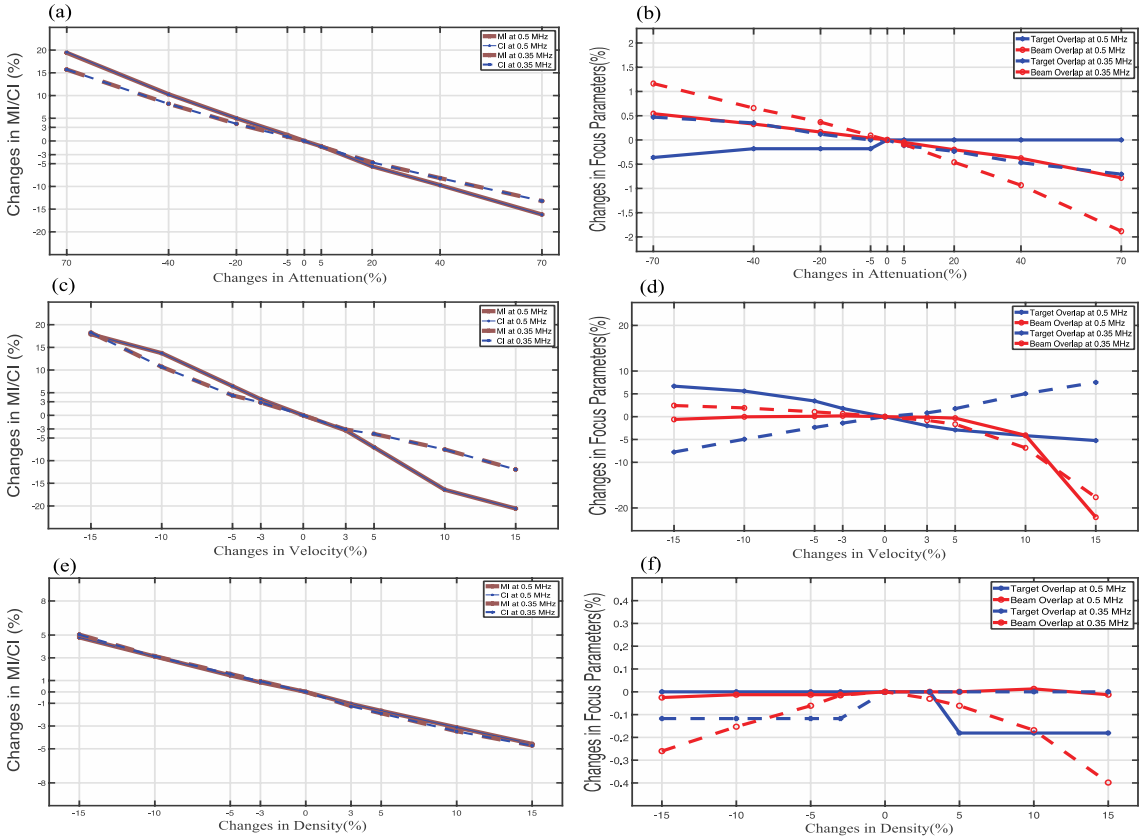

Figure 5-4 The skull effect on focusing area (target and beam overlap) and MI/CI when varying the skull acoustic properties based on standard configurations in the putamen study

b. Targeting of the Caudate at 0.35 MHz and 0.5 MHz

Figure 5-5 demonstrates the relative effect in the sensitivity analysis, which reflects the MI and CI changes that occur targeting the caudate at 0.35 MHz and 0.5 MHz when there are changes in the skull parameters. Also, when targeting the caudate at 0.5 MHz, the volume of the focal spot was decreased by 58.8% compared with the focal spot in the putamen.

The percentage change of MI and CI had almost the same trend as the variations of the attenuation and density both at 0.35 MHz and 0.5 MHz in Figure 5-5 (a), (c), and (e). Compared with the variations of attenuation and velocity, the percentage change of MI and CI was within ±5%. When the centre frequency was at 0.5 MHz, the maximum relative variations for the MI and CI were equal to 20.3%, 25.5%, and 4.6% for the attenuation, sound speed, and density, respectively. For the frequency at 0.35 MHz, these values became 20.4%, 9.9%, and 4.5%. For target overlap and beam overlap in the caudate study, the percentage change in volume parameters had a similar variation when attenuation and density changes (in Figure 5-5 (b) and (f)). The relative variations for the target overlap and beam overlap were equal to be within ±3% and ±1%, both at 0.35 MHz and 0.5 MHz for the attenuation and density, respectively. Meanwhile, in Figure 5-5 (d), the sound speed variations had a strong effect on target overlap when the frequency was at 0.5 MHz.

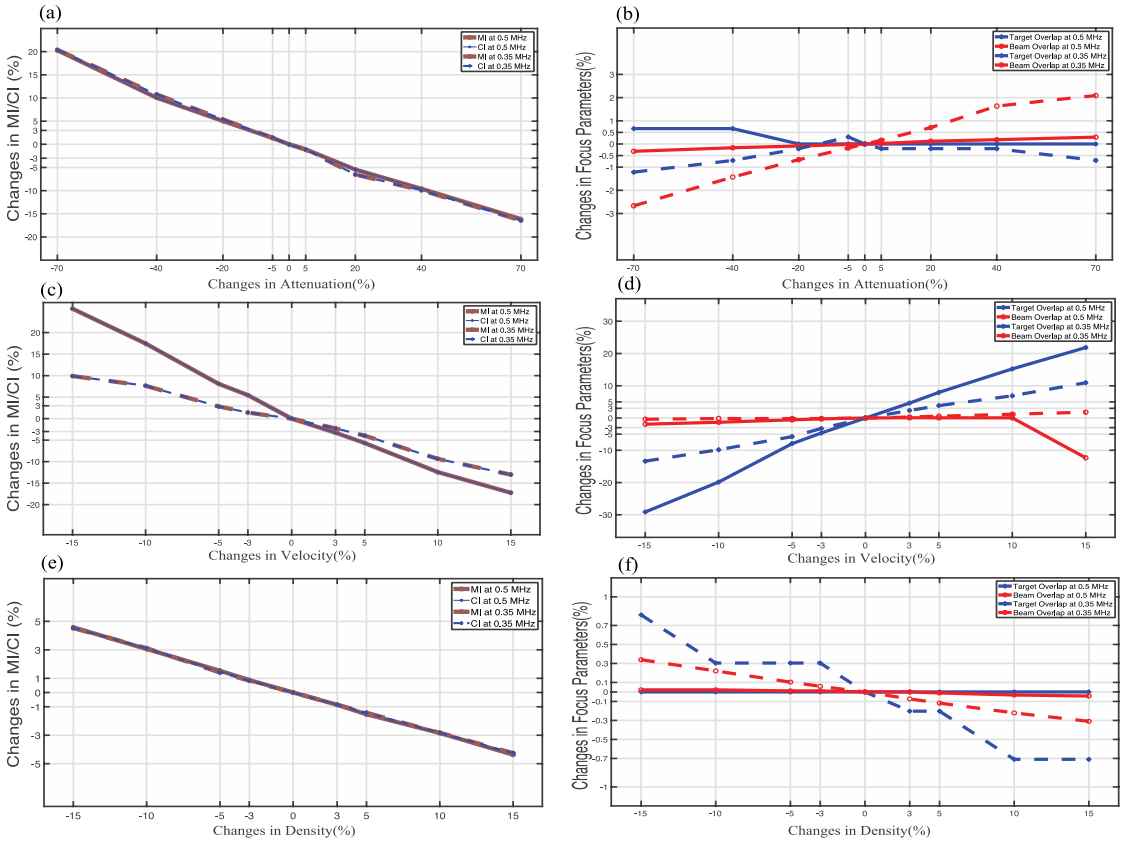

Figure 5-5 The skull effect on focusing area (target and beam overlap) and MI/CI when varying the skull acoustic properties based on standard configurations in the caudate study

5.3.4 Incidence angles effect on MI, CI and focal spot

The positions and parameters of targeting the putamen and caudate at 0.5 MHz as the default configurations were applied to investigate the effect of different incidence beam angles at 0.5 MHz on MI, CI and focal spot displacement. Based on the default incidence beam angle, the deflection angles of SEFT were changed from 3° to 10°. In each deflection angle, eight cases were studied, which means the direction of deflection was adjusted in eight ways with the same angles in the three-dimension coordinate, and results were demonstrated in Figure 5-6 and Figure 5-7.

a. Incidence angles change at 0.5 MHz targeting the putamen

The median values of MI and CI do not have a significant change when deflection angles vary from 3° to 10°. Compared with default configurations targeting the putamen in Table 5-3, the percentage changes of median values of MI and CI at deflection angles at 3°, 5°, and 7° are within 1%, and the values at 10° were around 3% in Figure 5-6 (a) and (b). However, the distance between the lower quartile (Q1) and the upper quartile (Q3) increases as the deflection angles increase from 3° to 10° for both MI and CI. When the deflection angles are at 10°, the differences between the maximum and minimum values of MI and CI are 0.25 and 0.35, respectively.

The results of focal spot volume, target overlap, and beam overlap at each deflection angle are provided in Figure 5-6 (c), (d) and (e). The median values of FWHM in the below box plots, percentage of target overlap and beam overlap change within 10%, as deflection angles varied from 3° to 10°. However, the maximum values in the below box plot have a significant change as deflection angles at 10°. Especially the difference between the two maximum values of FWHM volume is around 380 mm^3 (the default FWHM volume is 307.9 mm^3 at 0.5 MHz).

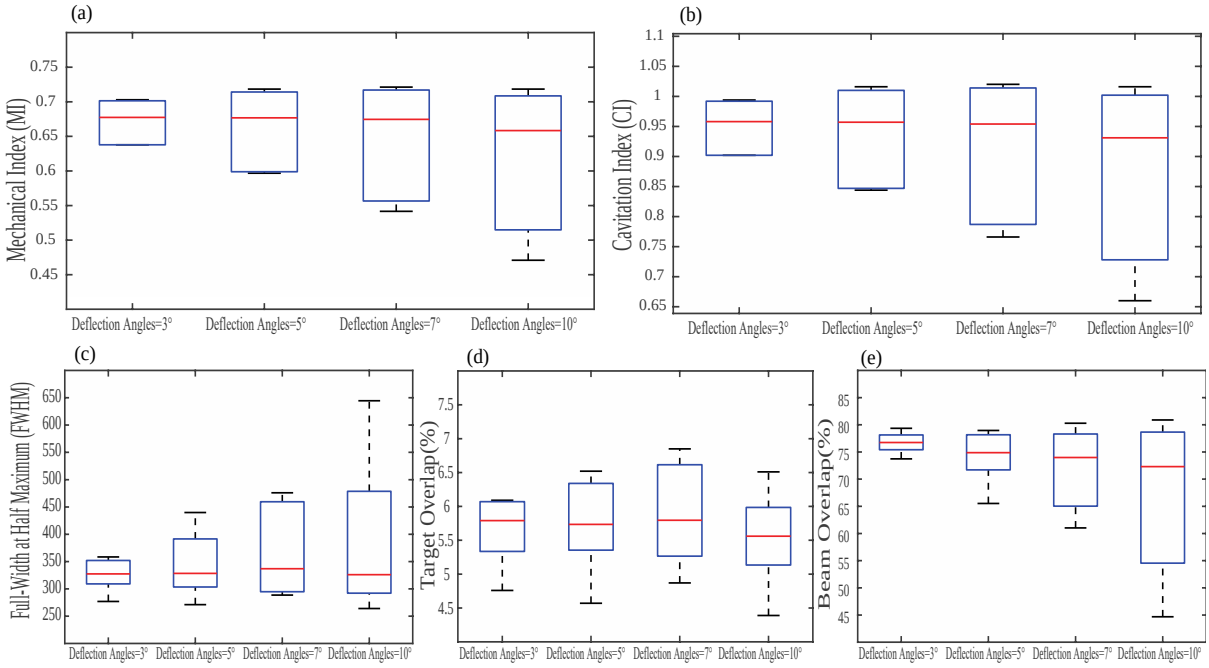

Figure 5-6 The incidence beam angles affect (a) MI, (b) CI, (c) FWHM, (d) Target overlap, and (e) Beam overlap when changing deflection angles in the putamen study

b. Incidence angles change at 0.5 MHz targeting the caudate

Compared with the MI of 0.65 in default configuration at 0.5 MHz targeting the caudate, the median value of MI changes 0.34%, 0.43%, 0.54%, and 3.81%, while angles at 3°, 5°, 7° and 10° deflection angles, respectively. The biggest difference between the maximum and minimum values were 0.136 and 0.192 at deflection angles of 7° for MI and CI in Figure 5-7 (a) and (b). In addition, the greatest values of Q3 and the smallest values of Q1 were at 10° deflection angles both for MI and CI.

The volume of FWHM is 127 mm^3 as a default value at 0.5 MHz, and the percentage change of the median value of FWHM volume is around 5% when deflection angles are 3°, 5°, and 7°, as the value is 17.2% at 10° of deflection angles. Also, the distance between the lower quartile (Q1) and the upper quartile (Q3) increased as the deflection angles increased from 3° to 10° in FWHM volume.

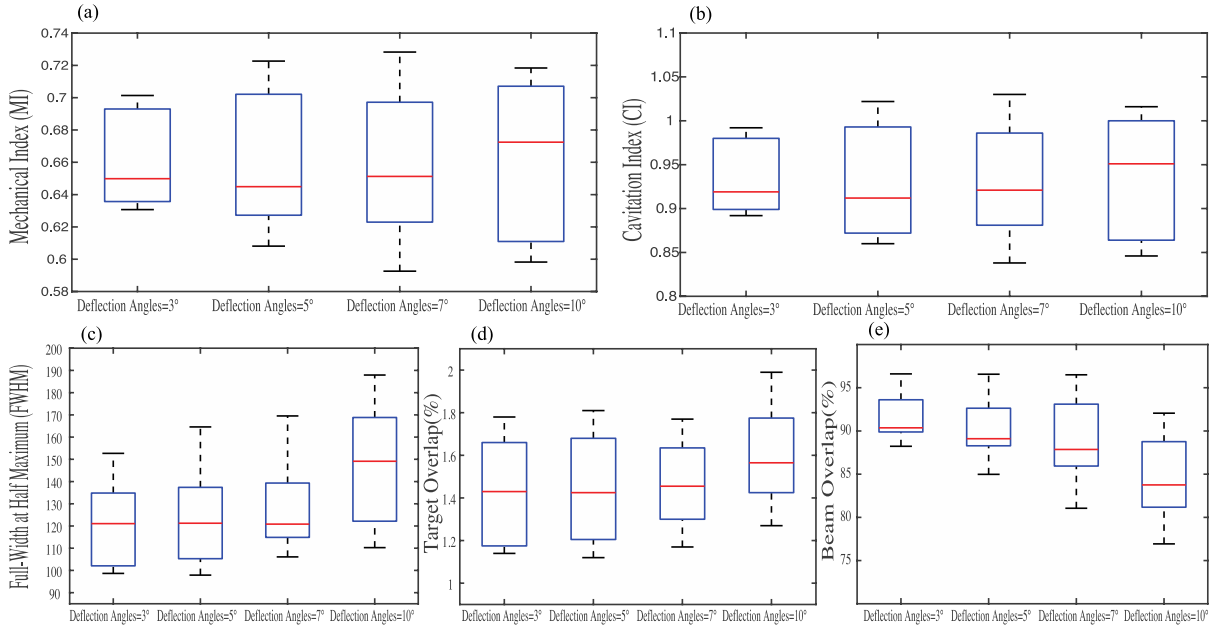

Figure 5-7 The incidence beam angles affect (a) MI, (b) CI, (c) FWHM, (d) Target overlap, and (e) Beam overlap when changing deflection angles in the caudate study

5.4 Discussion

This chapter presented a quantitative investigation of the intracranial change of focal spot areas, MI, and CI when ultrasound wave propagation through the skull at two representative ROIs (Putamen and Caudate) in the human head model. These two regions are widely used in preclinical experiments, as the ROIs in the dopamine pathway were altered in Parkinson's disease treatment. In addition, the MI and CI, as two parameters that indicated the inertial cavitation of microbubbles in BBB opening, were used to study how MI, CI, and corresponding focused areas change in the brain. The ultrasound energy must be focused through the skull in the application of BBB opening. The skull, as the primary barrier to ultrasound due to its attenuation, refraction, and dispersion of ultrasound wave propagation, varies in shape, thickness, and size among individuals. In clinical trials, determining the parameters of focal spot areas and interactions with the skull is difficult before treatment. Therefore, it is necessary to characterise the skull effect, including sensitivity analysis and incidence angles of beam propagation, on MI, CI, and the focal spot to

evaluate and precisely control transcranial ultrasound transmission through the human head model.

A high-resolution 3D human head model was developed, and two customised SEFTs and WLE acoustic equations were used to simulate ultrasound wave propagation through the skull to investigate MI, CI, and focal spot changes related to microbubble cavitation in BBB opening. The sensitivity analysis of the skull was conducted by varying the parameters of brain tissues' attenuation, sound speed, and density to investigate the impact of the properties of the skull on ultrasound wave propagation. Changing the deflection angles of transducers was also conducted to study the impact of incidence angles on MI and CI. In addition, the beam overlap parameter and target overlap parameter describing the volume above the half-maximum intensity threshold were calculated to quantify the volume interaction between the target region and the volume of FWHM.

5.4.1 Skull effect

The presence of the skull as one major difficulty in the application of the FUS-mediated BBB disruption affects the BBB opening. In this study, the individual tissues of the human head model were regarded as homogeneous for ultrasound wave propagation. A higher percentage change than default configurations of the sound speed, density and absorption of the skull leads to a decrease in the pressure change in the brain, decreasing corresponding MI and CI values. Compared to the results in Figure 5-4 and Figure 5-5, the MI and CI were relatively less sensitive to variations at the lower centre frequency (0.35 MHz) than those at the higher frequency (0.5 MHz). In addition, in the putamen and caudate study, MI and CI are most significantly affected by changes in attenuation and sound speed, while only a minor effect on MI and CI (within $\pm$5%) is caused by changes in density. Meanwhile, the percentage of the beam overlap and target overlap is minorly affected by changes in attenuation and density (less than $\pm$3% in putamen and caudate study of centre frequency at 0.35 MHz and 0.5 MHz),

while changes in velocity have a greater effect on the volume interaction between target regions and focal spots.

In most of the FUS-mediate BBB disruption studies, the personalised ultrasound transducers, such as phased array transducers and SEFT, including the number of elements, diameter, and focal length of the transducers, might be used to operate optimal ultrasound wave transmission. These optimal parameters were adjusted to the corresponding structure of the skull because the head model of human, non-human primates and rodents used in some experiments differ in skull density, thickness, and geometry. Kong et al. used a SEFT and sixteen 3D -printed skull models to investigate the effect of the skull thickness, density, and proportion of the trabecular bone [206]. They showed that the attenuation of ultrasound energy increased with the thickness of the skull and the trabecular bone volume ratio is an important factor related to the intensity of BBB opening.

5.4.2 Incidence beam effect

It is hard to avoid slight movement of transducers or subjects all the time, and the displacement might lead to unwanted intracranial field changes, such as pressure, energy, and focal spot shift [172]. This chapter also investigated the effect of different incidence angles on intracranial changes, including MI and CI and focal spot areas. The box plots in Figure 5-6 and Figure 5-7 show the results when the deflection angles were at 3°, 5°, 7° and 10°, and there were eight cases studied at each deflection angle. Compared with the deflection angles at 3°, 5° and 7°, the median values of MI and CI at 10° of deflection angles have an obvious change based on the default configurations. In addition, MI and CI at the cases of 10° have the largest interquartile range (IQR, IQR=Q3-Q1), and also for the FWHM changes in both putamen and caudate studies.

The deflection angles had an obvious effect on the volume of FWHM and the volume of target regions in Figure 5-6 and Figure 5-7 (c), (d), (e). The

median values of percentage target overlap in the box plots do not have a significant change in both putamen and caudate studies. However, the percentage beam overlap changes a lot in the caudate study and in the putamen. Also, the distances between two extreme values in the box plots in the caudate study were greater than those in the putamen. In the application of FUS-mediated BBB disruption, MRI-guided, as a technical auxiliary function, plays an important role in providing accurate location information of brain tissues. As evidenced by the above numerical sensitivity analyses, choosing and placing the ultrasound transducer at a suitable position over the brain skull is important. Also, the effect of the target and beam overlap parameters cannot be ignored.

To place the effect of deflection angles in context, Park et al. investigated the optimal placement of SEFT to deposit acoustic energy at desired brain targets using the average reflection coefficient method [207]. Based on their simulations, it was concluded that there is an inverse relationship between the average reflection coefficient and peak pressure. They also found that the optimal transducer placement was where the average reflection coefficient was the lowest. However, they only chose the brain's cortex region as a target area. In [126], the authors showed the impact of ultrasound's incidence angles on the BBB permeability using a fixed acoustic power corresponding to 0.65 MPa at the caudate-putamen and thalamus of the rat brain. Similar to our study, the paper emphasises the importance of intracranial pressure changes related to the permeability of BBB opening. Karakatsani et al. [189] also studied the targeting effect on the volume of BBB opening with incidence angles of the propagation wave. They kept the intracranial pressure field constant and observed the strong dependence of increasing the volume of BBB opening with the beam incidence angles. They emphasised that a normal angle is preferred for the large volume of BBB opening because the path of wave propagation through the skull is shorter when the curvature of the transducer is aligned to the skull geometry, as a similar result also pointed out in [207].

5.5 Conclusion

This study shows that customised SEFT based on the high-resolution 3D human head model has the potential to deliver precise energy and pressure at the deeper subcortical brain structure, putamen and caudate. MI and CI, as two metrics that reflected ultrasound-induced BBB disruption, were used to analyse the impact of the skull and incidence angles. Sensitivity analyses on the skull indicated that the MI and CI were relatively less sensitive to variations at the lower centre frequency (0.35 MHz) than those at the higher frequency (0.5 MHz). In addition, in the putamen and caudate study, MI and CI are most dramatically affected by attenuation and sound speed changes. Additionally, large deflection angles (at 7° and 10°) are more sensitive to MI and CI changes and correspond to the volume of focal spots than small deflection angles change. Finally, the numerical study was proven accurate in targeting deeper brain tissues through tFUS techniques, and the findings will support researchers and clinical doctors to deliver neuromodulation with higher precision.

CHAPTER 6: SPATIAL RESOLUTION INVESTIGATION IN TRANSCRANIAL FOCUSED ULTRASOUND STIMULATION

LIFU as a non-invasive brain stimulation modulates brain activity. However, achieving a high spatial resolution in the small brain region is still challenging. This Chapter aims to study the ultrasonic wave propagation through a 3D highly detailed human head model and computationally investigate the effect of LIFU with DSET in beam profiles, including ultrasonic energy change, the volume of FWHM, axial and lateral directions of the focal area. This study focuses on investigating whether customised dual transducers are able to deliver precise energy to the deeper brain structure and their spatial resolutions.

6.1 Introduction

Transcranial focused ultrasound stimulation has superior advantages over the others, such as TES [208], DBS [209] and TMS [210]. DBS, for example, requires electrodes implanted in the brain, which makes patients suffer from moving disorders and may increase the risk of bleeding [211]. Furthermore, both TES and TMS are limited by spatial specificity and target depth in the brain [1]. Meanwhile, several tFUS neuromodulation studies on animals [56, 212] and human trials [85, 154] demonstrated the non-invasive capability of tFUS in delivering ultrasonic energy at deep brain structures with high spatial resolution [213]. Also, the technological development of ultrasound transducers makes it possible to produce a highly focused region of interest through the intact skull and reversibly modulate the functions of specific brain regions [90].

The operating frequency used in most ultrasonic neuromodulation studies was lower than 690 kHz [56, 154, 214]. Such a kilohertz range of transducer frequency has been reported to have a better ability of ultrasonic wave propagation through the skull and modulation efficiency [215]. However, tFUS with lower frequencies might have problems targeting specific regions as beamforming focal spots become larger. The single-element piezoelectric ultrasound transducer with elliptical focal spots used in tFUS causes the long focal volume in the axis direction, and the focal volume might span multiple brain sub-regions.

Multi-element arrays with hundreds of individual transducers can reduce the focal size by compensating for the aberration [150, 151]. However, the hardware demand is relatively high, and the cost is much more than SEFT. Another method to reduce the focal area is to use higher-frequency ultrasound transducers, but the focal area in the axial direction remains unchanged (only changes in the lateral direction) [177]. Furthermore, a ring-shaped ultrasound transducer based on capacitive micromachined techniques [216] has been developed for the purpose of neuromodulation but also suffers from relatively low resolution in the axial direction.

The axial resolution in tFUS is mainly determined by the transducer's operating frequency, curvature radius (focal length), and aperture width. A larger aperture width SEFT could reduce the focal area and achieve higher resolution using the same frequency and curvature radius [154]. Also, hemispherical phased array element transducers used in [159, 217] can achieve higher spatial resolution in the axial direction by circuitry design and signal processing. This transducer is relatively operating complex, high-cost, and bulkier than SEFT. Jiang et al. [218] proposed an optoacoustic neural stimulation method based on the Fibre-Optoacoustic Converter technique, which achieved superior spatial resolution than conventional piezo-based tFUS transducers. However, this modality is an invasive method that implants a firer tip into the brain to activate neurons

[218]. It is still challenging to explore the non-invasive ultrasonic neuromodulation with low cost, accessibility, and higher spatial resolution in axial direction advantages.

Inspired by the multi-element array transducers, the DSET were proposed to achieve high spatial resolution in the focal area and corresponding FWHM focal volume. There is no precise numerical research investigating the influence of DSET on spatial resolution in axial and lateral directions for low-intensity ultrasound neuromodulation. This study was proposed to fill this gap. A 3D highly detailed human head model was constructed based on MRI images. Then, a customised transducer was developed to deliver LIFU (10 W/cm^2) at subcortical structures (thalamus). After that, the crossing angles between dual transducers were set from 40° to 80° to evaluate the effect of spatial resolutions and the maximum intensity in the target area. Then, the phase difference of dual transducers was changed to simulate misalignment ultrasound wave propagation through brain tissues.

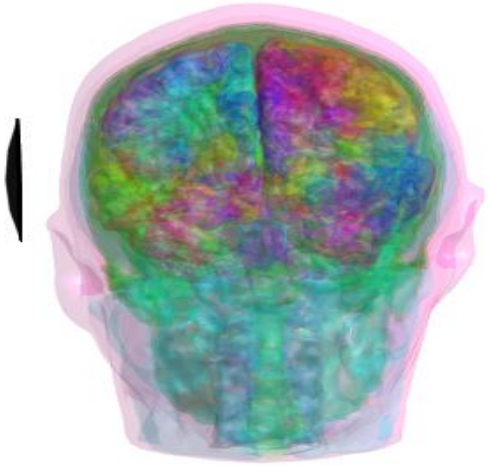

Figure 6-1 A highly detailed 3D human head model configured with SEFT, including the scalp, fat, skull, CSF, GM, and WM as the main tissues

6.2 Methods

The application of image-guided tFUS based on the MRI technique was employed to target the focused ultrasound in the brain structures due to

the interpersonal difference of cranial structures [82, 219]. Also, co-registration from CT and MRI techniques was applied to investigate the skull's effect on neuromodulation, which has a positive effect on simplifying the workflow of image-guided tFUS [155]. In this Chapter, the detailed human head model (details in Section 3.1.2) based on MRI images with two SEFTs was used to investigate the spatial resolution of tFUS.

6.2.1 Customised dual transducers

Two customised SEFTs have been proposed with the central frequency at 0.35 MHz, 0.5 MHz, and 0.65 MHz, respectively. Such frequencies were used to be generally necessary for neuromodulation because the attenuation of skull and brain tissues increases while using higher frequencies. The position of the SEFT placement was demonstrated in Figure 6-1, and the corresponding region of the skull was regarded as the temporal bone, called the 'acoustic window', since it is recognised as the thinnest part of the human skull [153]. The geometrically focused ultrasound transducer placed at the acoustic window has a curvature radius of 95 mm and an aperture width of 60 mm. In the DSET system, the identically manufactured transducers were used as SEFT. The customsied transducer aimed to deliver a focal spot to the target region in the brain structure with enough focal length and intensity of 10 W/cm^2.

6.2.2 Governing equation and simulation

The WLE equation (details in Section 3.2.1) captures ultrasonic wave reflections at interfaces between air-brain tissue and bone-brain tissue. Also, the 3D FDTD method (details in Section 3.2.2) was used to discretise nonuniform rectilinear grids, which has a positive effect on flexible gridding and assigning brain tissue properties (impedance, attenuation coefficient, density, and sound of speed) [159].

The validation experiments were conducted and compared with peers' studies, including practical experiments and numerical modelling. It is

noted that the experiment results in the major axis and minor axis of FWHM slightly differ from computational models (less than 2 mm), which might be caused by the transducer mounting positions. The comparison results of the experimental and computational modelling are provided in Section 4.2.3 with Table 4-1 and Table 4-2.

The DSETs consist of two single-element transducers with the same central frequency and manufacture size. For precise positioning of the focal spot of DSETs during the numerical 3D head model stimulation, the beam simulations of DSETs were conducted based on the SEFT neuromodulation on the target region. After simulating the beam profile at the target region using the single transducer, the DSETs were positioned, and beam profiles crossed at the focal spot. The crossed angles between two transducers were set from $40°$ to $80°$, and the increment as $10°$. The maximum intensity at the focal spot was obtained after wave propagation simulation through the head model. Then, the axial and lateral resolutions of the FWHM area in these two directions were measured. Figure 6-2 demonstrates the beam profile simulation of dual transducers with different crossing angles.

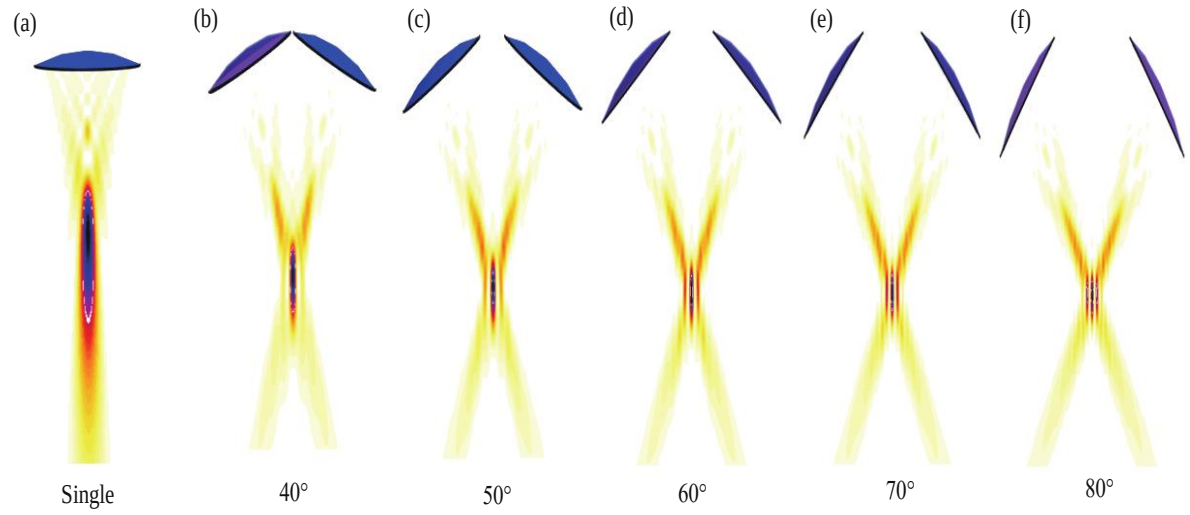

Figure 6-2 A single transducer (a) and DSETs with crossing angles of (b) 40°, (c) 50°, (d) 60°, (e) 70°, and (f) 80° are used to simulate ultrasonic wave propagation in a water tank. The corresponding beam profiles in the 2D plane are provided as well.

6.3 Simulation results

6.3.1 Computational results in a water tank

The intensity of focused ultrasound energy was 23.67 W/cm^2, and the pressure amplitude was 0.83 MPa when simulating the ultrasonic wave propagation using SEFT in a water tank. Figure 6-3 a(i) shows the beam profile of FWHM at the maximum intensity of 23.67 W/cm^2 in a water tank, and Figure 6-3a (ii)-(vi) represent the FWHM beam profiles of dual transducers using the same input parameters and source amplitude with SEFT by changing crossing angles from 40° to 80°. Figure 6-3 b-e demonstrate the comparison results of beam profiles between SEFT and crossing angles of dual transducers. These results, axial distance, lateral distance, maximum intensity, and FWHM volume, were normalized to that of the SEFT beam profile.

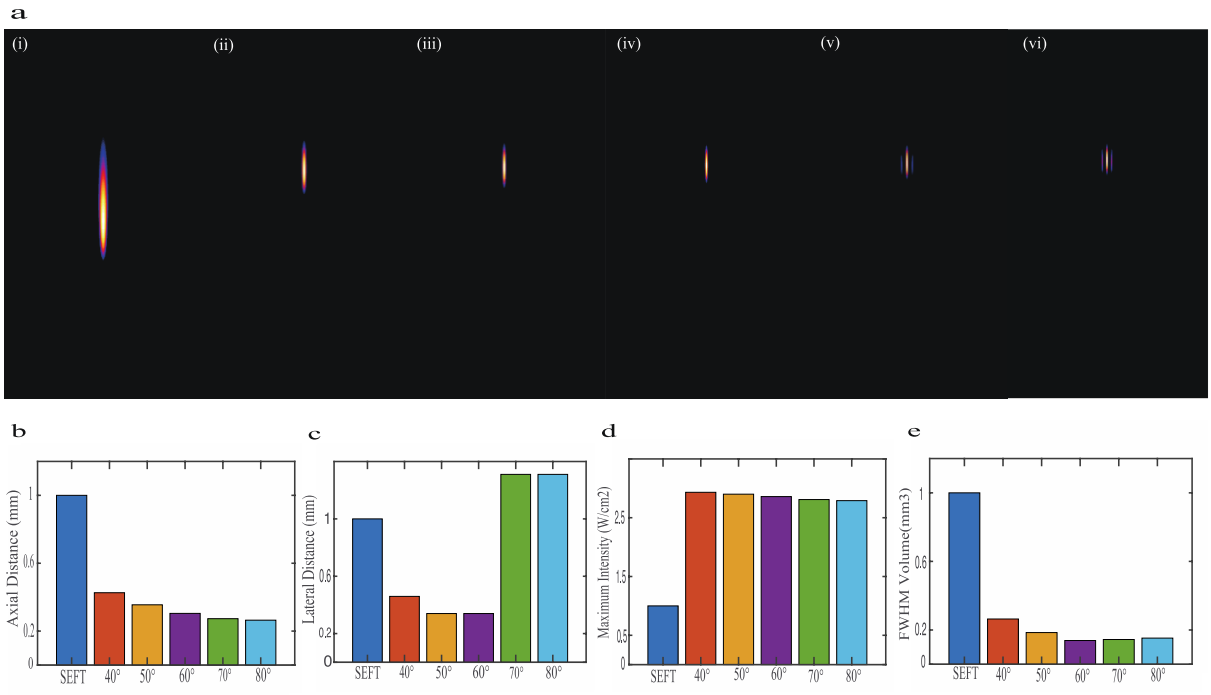

Figure 6-3 Beam profile simulation in a water tank. (a) FWHM area in the 2D plane with (i) single-element transducer and dual transducers with (ii – vi) crossing angles from 40° to 80°. Comparison of the beam profile of FWHM after normalized in (b) axial distance, (c) lateral distance, (d) maximum intensity, and (e) volume of FWHM in 3D simulation results.

The axial focal spot area and axial distance were significantly reduced when using the DSET with all crossing angles in Figure 6-3 a. In addition, DSET

with 80° crossing angle has the highest axial resolutions and tripled intensity, which are about 5 times and 2.8 times greater than the values in SEFT, respectively (Figure 6-3 b and d). The volume of FWHM is 6.5 times smaller than that of the SEFT (Figure 6-3 e)

6.3.2 Adapted transducers with human head model

Table 6-1 SEFTs parameters and beam profiles for the free water and human head model

Parameters	Value (Water Tank)	Value (Human Head Model)
Curvature radius (mm)	50	95
Aperture width (mm)	30	60
Source Amplitude (kPa)	145	95
frequency (MHz)	0.5	0.5
Max pressure (MPa)	0.83	0.55
Max intensity (W/cm^2)	23.67	10.1

In order to generate an FWHM beam profile in the subcortical region (thalamus) of the brain, a specific ultrasound transducer was customised to simulate tFUS wave propagation with a 3D human head model. The properties of SEFT and beam profiles in the water tank and the human head model are provided in Table 6-1. The transducer has a central frequency of 0.5 MHz with a curvature radius of 95 mm and an aperture width of 60 mm. The source amplitude was adapted to 95 kPa, which was used to reach the target intensity at 10 W/cm^2 in the thalamus for neuromodulation. The adapted ultrasound transducer was used for customising DSETs and analysing the human head model in the following works.

6.3.3 Beam profile measurement of DSET

Firstly, the beam profile measurement of SEFT with 0.5 MHz was conducted

to characterize the intensity distribution, focal spot area, and FWHM in the 3D human head model, as shown in Figure 6-4. The distance in axial and lateral directions defined by FWHM was measured at around 38.7 mm and 4.3 mm, respectively. Then, the adapted DSET consisting of two identical single transducers with 0.5 MHz central frequency was used to simulate the ultrasonic wave propagation through the human head model. The performance of DSET at crossing angles from $40°$ to $80°$ was simulated. The maximum intensity of the focal spot region decreased while the crossing angles increased to $80°$. However, the focal lobe was split into two focal lobes at $60°$ and $70°$ crossing angles (Figure 6-5 a(iv) and (v)). In addition, for the crossing angle of $80°$, there were two secondary lobes on two sides of the primary focal spot area (Figure 6-5 a(vi)).

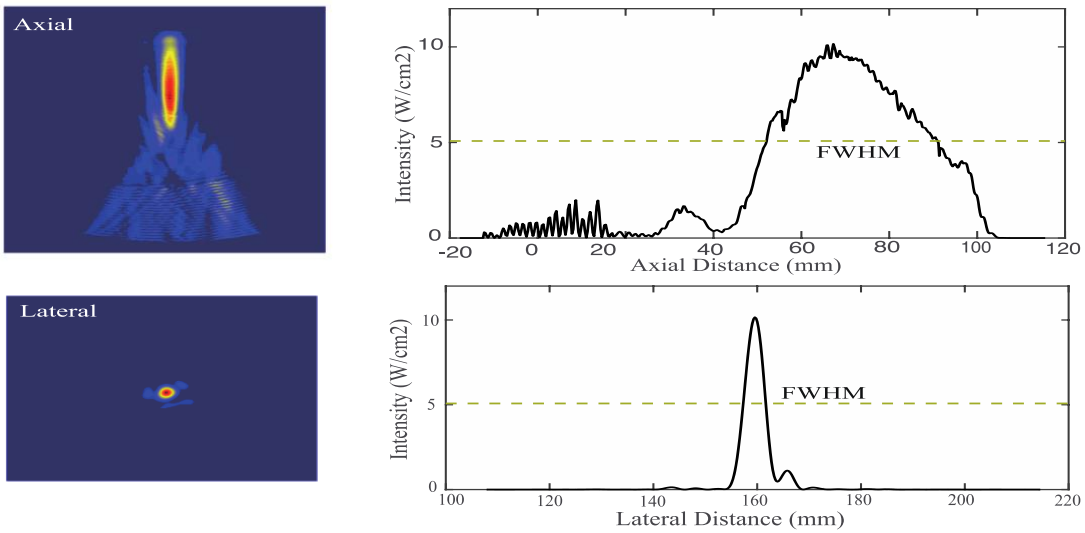

Figure 6-4 SEFT beam profile of focal length and FWHM in axial and lateral directions

The DSET had a superior axial resolution over SEFT. The axial distance decreased to around 7.2 mm at $80°$ crossing angle, which was improved around 5.5 times in the axial resolution (Figure 6-5 b). In addition, the focal spot at the target region of FWHM volume changed significantly, which decreased around $60\ mm^3$ compared to the SEFT beam profile (Figure 6-5 c). In contrast, the $80°$ crossing angle had a poor lateral resolution than SEFT due to the presence of side lobes. Similar beam profiles with side

lobes were observed at 60° and 70° angles. Compared to the lateral resolution from 40° to 80° crossing angles, the best resolution case was observed in 50° angle case (Figure 6-5 c). The maximum intensity measured using DSET was around 30 W/cm^2, approximately a three-fold increase than SEFT. It is noted that the intensity distribution at the focal spot increased due to the beam overlap from dual transducers. As a result, the intensity of each transducer for deep region neuromodulation in the brain was less than SEFT, which has a positive effect on reducing the energy distribution in the adjacent target regions.

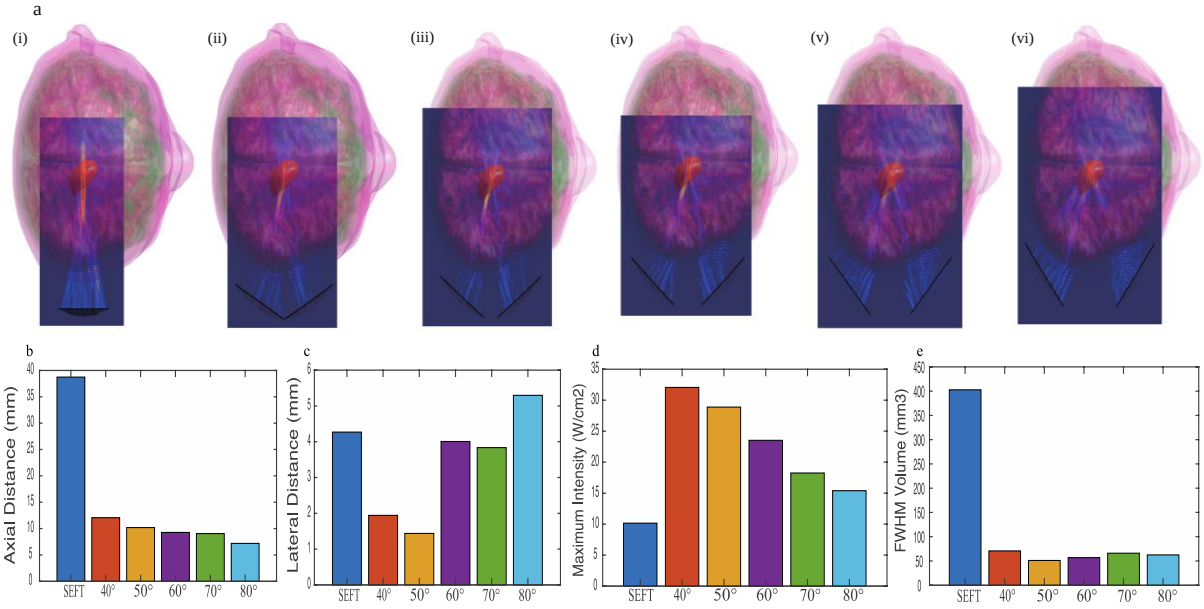

Figure 6-5 Beam profile simulation in a 3D human head model. (a) FWHM area in the 2D plane with (i) single-element transducer and dual transducers with (ii – vi) crossing angles from 40° to 80°. Comparison of the beam profile of FWHM after normalized in (b) axial distance, (c) lateral distance, (d) maximum intensity, and (e) volume of FWHM in 3D simulation results.

The DSET had a better performance in high spatial resolution. However, DSET with crossing angles at 60°, 70°, and 80° caused unwanted side focal spot regions. The maximum intensity of the main and side lobes was measured, and the corresponding intensity of these two regions decreased when crossing angles increased from 60° to 80°. Figure 6-6 provided the comparison results of main and side focal spot areas. The maximum

intensity of SEFT in 40° and 50° cases did not have side lobes when measuring the beam profile of FWHM.

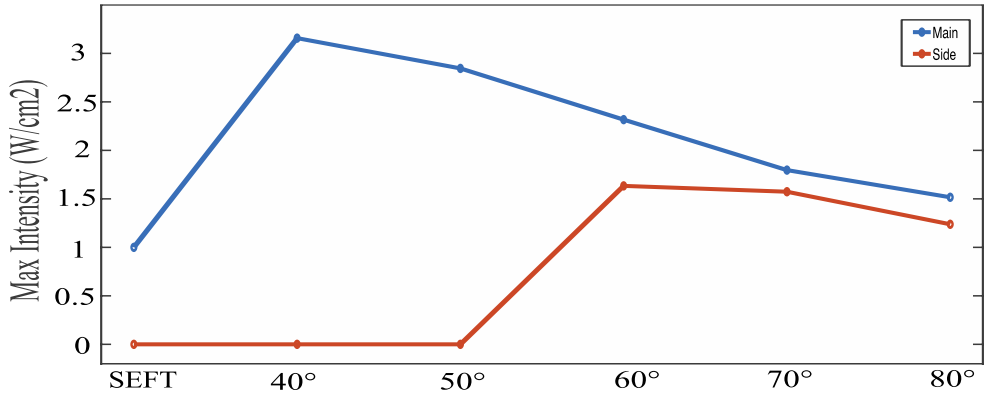

Figure 6-6 Comparison maximum intensity of main and side focal spot areas

6.3.4 Effect of the phase difference

In the numerical simulation, achieving the perfect alignment of two transducers in three dimensions is possible. However, in practice, placing the transducers and aligning them is very challenging. Thus, it is necessary to investigate the effect of phase difference on the intensity distribution and spatial resolution of FWHM volume, computational simulation of crossing angles from 40°to 80°using DSET at varying phases in Figure 6-7.

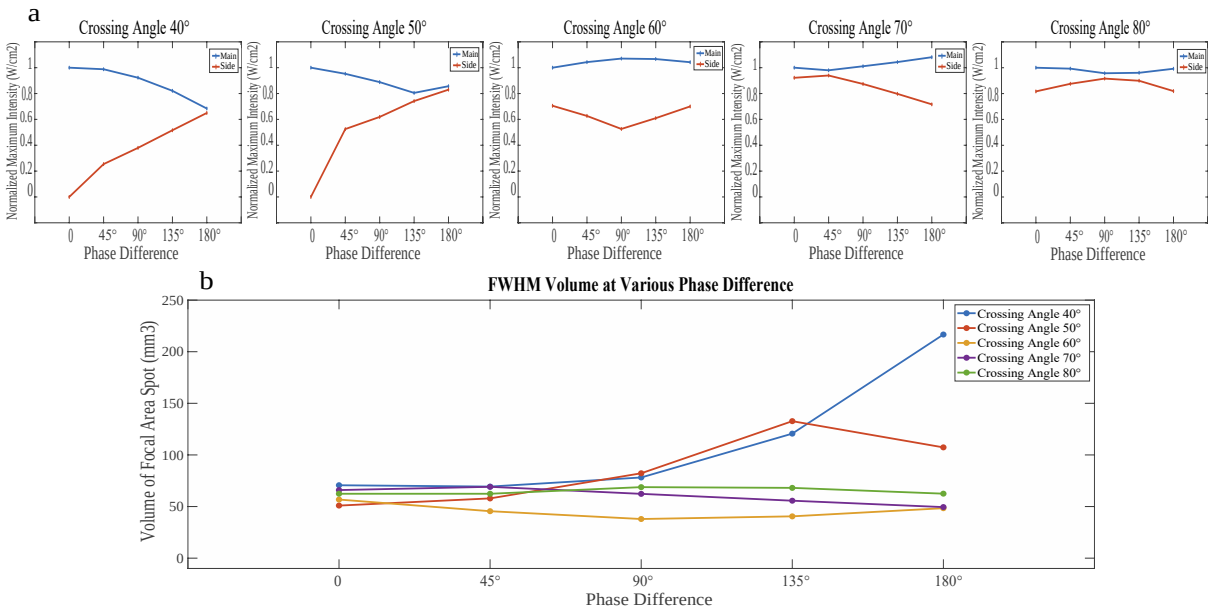

Figure 6-7 Results of phase difference. (a) Comparison maximum intensity of main and side focal spot areas at varying phases. (b) Comparison FWHM volume at varying phase.

The phase difference was set from $\frac{\lambda}{8}$ to $\frac{\lambda}{2}$ (45°, 90°, 135°, and 180°). For the crossing angles of 40° and 50°, there was only the main focal lobe when

the phase difference was 0. The maximum normalized intensity in the main lobe decreased when the phase difference increased to $\frac{\lambda}{2}$. The main lobe is split into two focal lobes. Furthermore, the normalized maximum intensity in the side lobe changed significantly when the phases varied. In contrast, the side lobes existed on the two sides of the main lobe for the crossing angles of 60°, 70°, and 80°. However, the maximum intensity in both the main and side lobes did not change that much. The percentage changes of side lobes' maximum intensity for crossing angles of 60°, 70°, and 80° were around 25%, 24%, and 11%, respectively. Meanwhile, the phases vary, causing a slight change in the maximum intensity of the main lobe around 7%, 9%, and 4%, respectively. In addition, the FWHM volume, including main and side lobes, was not affected by the phase increasing for crossing angles of 60°, 70°, and 80°. Thus, while the lateral resolution of cases for crossing angles at 60°, 70°, and 80° was poorer than smaller crossing angles at 40° and 50° due to the caused side lobes, the case of crossing angle at 80° had the highest axial resolution and robustness to phase difference in terms of FWHM volume and maximum intensity of side lobes.

6.4 Evaluation and comparison

In this Chapter, a high-resolution 3D human head model was constructed, and customised dual transducers and WLE equation were used to simulate ultrasonic wave propagation through the skull to investigate the spatial resolution in the deeper brain structure thalamus. The beam profiles of DSET, such as axial distance, lateral distance, maximum intensity, and volume of FWHM, were measured while DSET varied at different crossing angles. Furthermore, phases difference between $\frac{\lambda}{8}$ and $\frac{\lambda}{2}$ were applied to assess the tolerance of dual transducers system with the maximum intensity of main and side lobes and quantify the spatial resolution by volume of FWHM.

Compared with SEFT, the beam profiles of dual transducers crossed at 40°, 50°, and 60° in a water tank have a higher axial resolution with smaller FWHM volume and a more focused intensity distribution. However, 70°and 80°crossing angle configurations have a poor resolution in the lateral direction, which results in two side foci. Similar cases in which secondary lobes exist on both sides of the primary lobe are shown in dual transducers beam simulation through the skull.

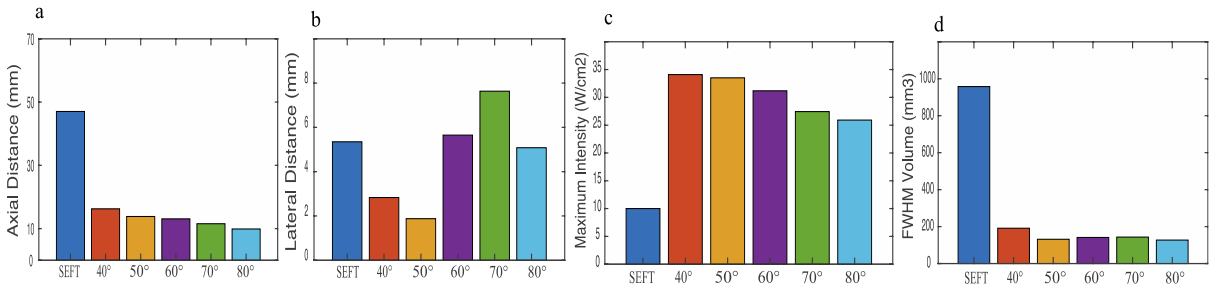

Figure 6-8 Beam profile simulation with the 3D human head model at the frequency of 0.35 MHz. (a) Axial distance, (b) lateral distance, (c) maximum intensity, and (d) volume of FWHM in 3D simulation comparison results.

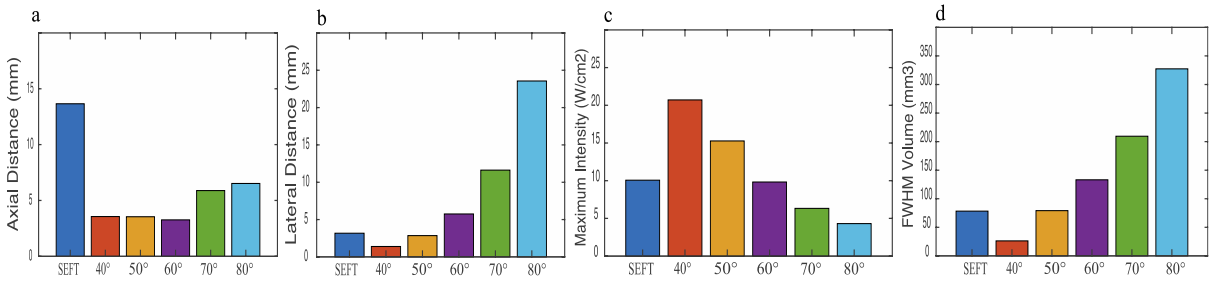

Figure 6-9 Beam profile simulation with the 3D human head model at the frequency of 0.65 MHz. (a) Axial distance, (b) lateral distance, (c) maximum intensity, and (d) volume of FWHM in 3D simulation comparison results.

The beam profile measurement in the human head model when the frequency was 0.5 MHz demonstrated that the axial diameter and focal area of FWHM were greatly reduced for all crossing angles. A crossing angle of 80° showed spatial resolution of the highest axial resolution, and the volume of FWHM increased around 5.5 times and 6.5 times greater than that of the single transducer, respectively. Pouliopoulos et al. [220] showed that the width and length of the focal area were decreased to 2.7 $\pm$ 2.4% and 8.4 $\pm$ 4.8% in the lateral and axial directions, respectively. To study the frequency impact on the ultrasound beam transmission through the brain, we also investigated the beam profiles at frequencies of 0.35 MHz, 0.5 MHz, and 0.65 MHz, using DSET on the 3D detailed human head model.

Firstly, the maximum intensity at the focal spot was 10 W/cm^2 using SEFT when the frequency was 0.35, 0.5, and 0.65 MHZ. The numerical results of SEFT showed that higher frequency (0.65 MHz) had a better spatial resolution than lower frequencies (0.35 MHz and 0.5 MHZ) in axial and later directions. The axial and lateral resolution increased to around 70% and 40%, 65% and 25%, from 0.35 MHz (in Figure 6-8 and Figure 6-10) and 0.5 MHz (Figure 6-5) to 0.65 MHz (in and Figure 6-9 Figure 6-11), respectively. Secondly, the results by DSET demonstrated that dual transducers have a superior spatial resolution in axial diameters than SEFT. However, the poor spatial resolution cases in lateral diameters caused by side foci existed at crossed angles 60°, 70°, and 80°. Thirdly, the maximum intensity from dual transducers is around 3.4, 3.2, and 2.1 times bigger than SEFT. With increasing the crossing angles of dual transducers, the maximum intensity decreased from the highest (angle-40°) to the lowest (angle-80°) in all three frequencies. Fourthly, the volume of FWHM, including side foci, was reduced dramatically by dual transducers than SEFT when frequencies were 0.35 MHz and 0.5 MHz. In contrast, the volume of FWHM increased around 5 times than SEFT when the frequency was 0.65 MHz, which results in more unwanted lateral side foci than lower frequencies. Fifthly, the maximum intensity comparison between the main and side focal spot areas was also investigated, and the maximum intensity in the main lobe decreased with greater crossing angles. At the same time, a similar trend was observed in the side lobe.

In practice, it is difficult to achieve perfect wave propagation alignment when using dual transducers. Various phases from $\frac{\lambda}{8}$ to $\frac{\lambda}{2}$ (45°, 90°, 135°, and 180°) were set to quantitatively investigate the phase effect on the maximum intensity of the main and side lobes and the corresponding FWHM volume for all crossing angles (40°, 50°, 60°, 70°and 80°). From Figure 6-7, the maximum intensity in the side lobe changes dramatically for both crossing angles 40° and 50°, and the maximum intensity in the main lobe

also has a noticeable change compared with higher crossing angles. Meanwhile, the volume of FWHM increases significantly for both crossing angles 40°and 50°when phases increase from $\frac{\lambda}{4}$ to $\frac{\lambda}{2}$. In contrast, for the crossing angle of 80°, maximum intensity in both main and side lobes does not have a significant change and corresponding volume of FWHM. While the lateral resolutions of higher crossing angle cases (60°, 70°, and 80°-angles) are poorer compared to lower crossing angle cases (40°and 50°-angles) due to the side lobes, higher crossing angle cases have relative better axial resolution and robustness to phase difference effect.

It is worth noting that, in this study, the maximum intensity using SEFT was 10 W/cm^2 , and the maximum intensity from the dual transducers was around 3.5 times bigger (below the 190 maximum recommended limitation [221]). Thus, in a dual transducers system, a lower amplitude pressure is needed for each transducer to reach the same intensity as SEFT. As a result, the adjacent brain tissues of the target area absorb less ultrasonic energy.

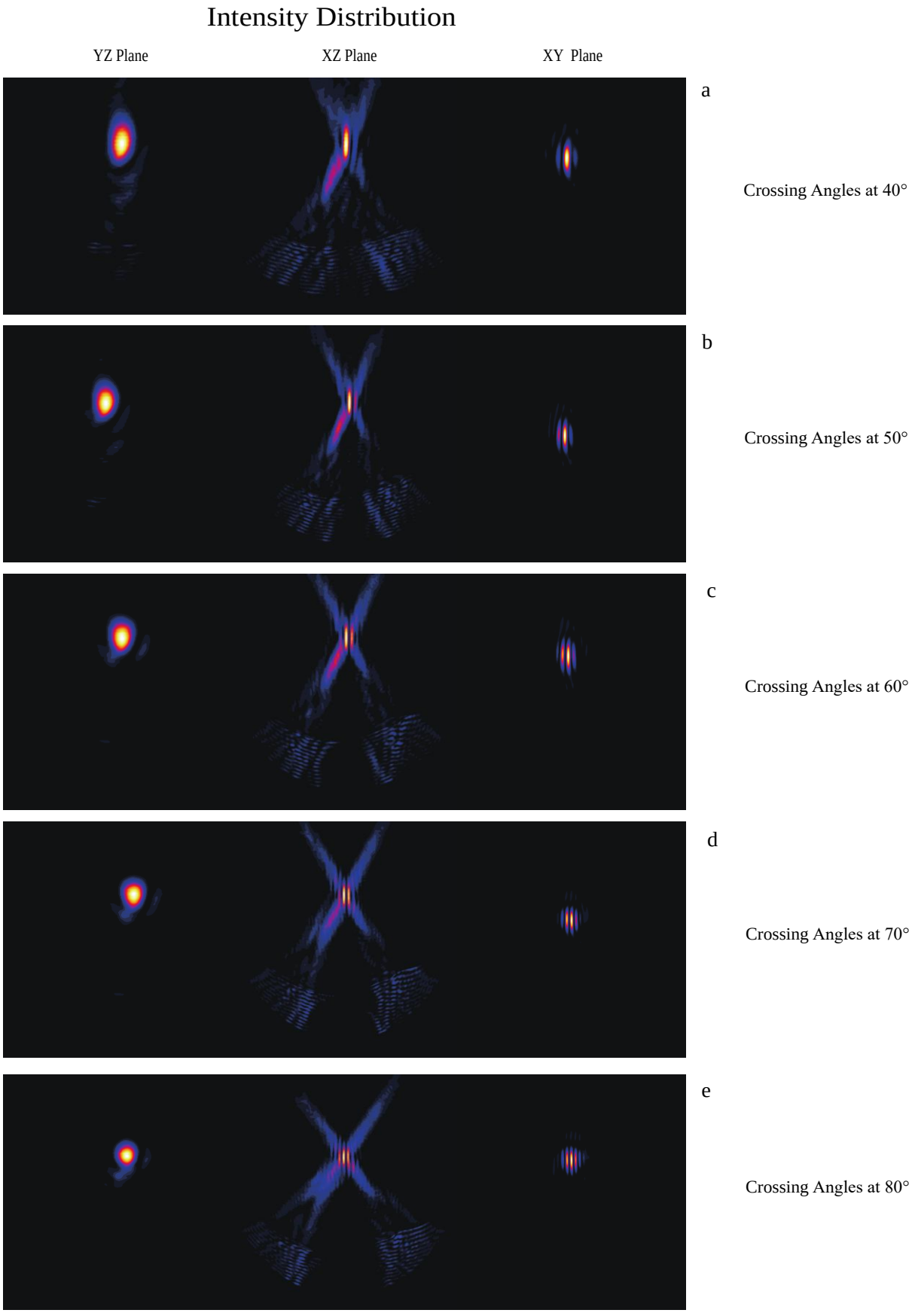

Figure 6-10 Intensity distribution in three dimensions when the frequency was 0.35 MHz. (a) Crossing angle at 40°, (b) crossing angle at 50°, (c) crossing angle at 60°, (d) crossing angle at 70°, and (e) crossing angle at 80°.

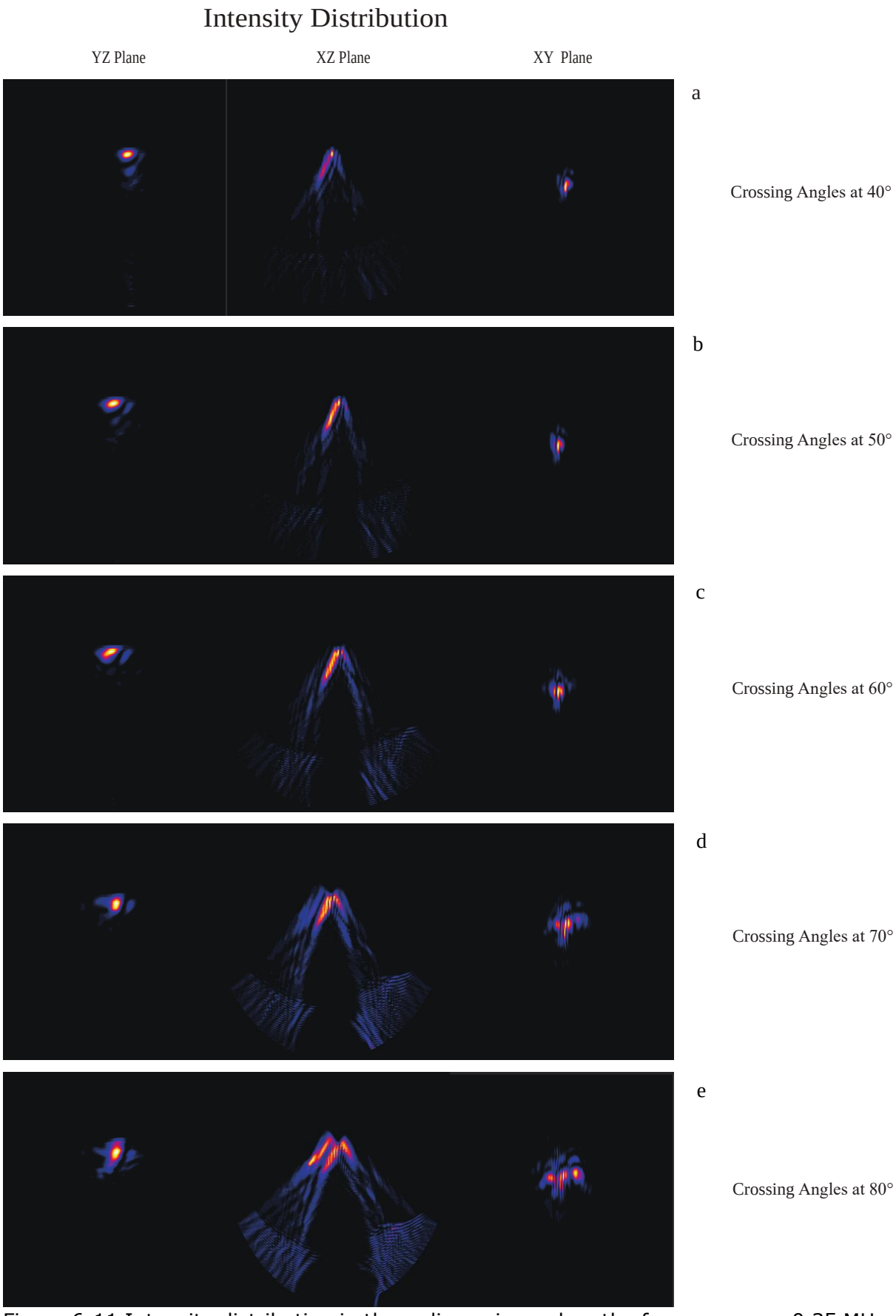

Figure 6-11 Intensity distribution in three dimensions when the frequency was 0.35 MHz. (a) Crossing angle at 40°, (b) crossing angle at 50°, (c) crossing angle at 60°, (d) crossing angle at 70°, and (e) crossing angle at 80°.

6.5 Conclusion

In this Chapter, the DSET with LIFU was numerically examined to improve the capability of SEFT and spatial resolution analysis. Custom-designed transducer arrangements and intensity at focus spots were investigated to determine the spatial resolution of target treatment regions.

The study in this Chapter demonstrates that coupled dual transducers with a 3D human head model are able to deliver precise energy to the deeper subcortical brain structure, and dual transducers systems have a higher spatial resolution than conventional SEFT. According to the findings, the following specific conclusions are drawn:

1) Compared with SEFT, the focal diameter in the axial direction is around 7 mm at 80° crossing angle using DSET, which is around 5.5 times the improvement when the frequency is at 0.5 MHz.
2) The case with a crossing angle of 80° has the highest axial resolution and robustness to phase difference in terms of FWHM volume and maximum intensity of side lobes when the frequency is 0.5 MHz.
3) Increasing the frequency has a direct influence on the spatial resolution level in the axial direction (i.e., increasing of frequency from 0.35 MHz and 0.5 MHz to 0.65 MHz, enhancing the spatial resolution in the axial direction by 67% and 55%, respectively)
4) A suitable combination of transducer size, location, and power level can be selected to achieve the best treatment based on the target location in the brain.

This work in this study presents a valuable method for highly detailed and specific, non-invasive brain stimulation using tFUS, which could be further explored and utilized in future research and clinical practices.

CHAPTER 7: NUMERICAL EVALUATION OF THE HUMAN SKULL WITH FOCUSED ULTRASOUND STIMULATION

In this chapter, the skull as the primary barrier to the delivery of ultrasound to the deep brain region was investigated using different transducer modalities, including multiple transducers and single-element transducers. Also, two highly detailed skull models are constructed using CT images from the Visible Human Project. The two different transducer placements are investigated, including the temporal window and top over the skull. The simulations of acoustic wave propagation were carried out based on FDTD methods, and the results were analysed.

7.1 Introduction

The acoustic wave propagation through the human cranial bone is essential for non-invasive transcranial therapeutic applications, such as brain tumour ablation and brain thrombosis ablation angioplasty [222]. The technique of tFUS was recently utilized as an alternative for neuromodulation, as the acoustic energy can be non-invasively delivered to deep targeted brain circuits [173, 223]. However, the skull with irregular geometrical shapes is treated as the primary barrier to ultrasound due to its high frequency-dependent attenuation and refraction of acoustic waves, which might induce energy loss and inevitable distortion in acoustic waves, such as deflection and phase aberration [170, 224].

Over the years, diverse skull models have been developed for studying transcranial ultrasound stimulation. For example, Hatakeyama et al. treated the skull as a spherical shell, which made it easier to measure the thickness and sound speed of the skull [225]. Clement et al. Investigated the acoustic shear wave transmission using spectral decomposition, as the

skull was regarded as a shell with non-parallel boundaries [226]. A simplified skull geometry change from flat to curve induced the maximum intensity reducing about 40% in [153]. Thus, detailed skull geometry is desired in tFUS applications, which determines the accurate intracranial pressure assessment.

This chapter focuses on modelling the skull and treating the other brain tissues as water, as we have already discussed how other brain soft tissues affect acoustic wave propagation in chapter 4. Numerical modelling of tFUS using the detailed models of the skull has been studied previously in HIFU for thermal ablation and microbubble-enhanced applications [169, 227]. In this study, we developed a detailed model of the skull based on medical images to evaluate linear and non-linear simulations and compare the influence of the different types of transducers in intracranial intensity maps.

7.2 Methods

7.2.1 CT imaging of the skull

The Visible Human Project (VHP) has proposed three-dimension anatomically detailed human bodies, including a human male and a human female, for publicly available research [228]. Especially the VHP provides a public-domain library of cross-sectional cryosection, MIR, and CT images. In this study, the CT images of the anatomical head model from the VHP data set were used to construct the human head model with detailed skull tissue. The CT data consist of axial CT scans of the entire body taken at 1 mm intervals at a pixel resolution, each pixel making up 12 bits of grey tone. The approximately 7.5-megabyte axial anatomical images are 2048 pixels by 1216 pixels, each 0.33 mm in size and defined by 24 bits of colour. However, the axial anatomical images were obtained at 0.33 mm intervals. Spacing in the "Z" dimension was reduced to 0.33 mm to match the 0.33 mm pixel sizing in the "X-Y" plane. As a result, three-dimensional reconstructions can work with cubic voxels. There are 234 anatomical

images in the Head dataset from the Visible Human Female data set. The Visible Human Project DICOM CT datasets are from the University of Iowa Magnetic Resonance Research Facility [229]. The anatomical skull model was segmented from whole brain tissues using the threshold method in the iSeg toolkit, a medical image segmentation toolset developed by IT'IS [230]. The CT scans of anatomical skull models, including one female and one male model, and the segmentation results are shown in Figure 7-1. Also, the geometry of these two skull models is shown in Table 7-1.

Table 7-1 The geometry of the skull models

Skull Model	Length (mm)	Width (mm)	Height (mm)
Female	176.82	203.17	184.15
Male	138.74	198.14	195.11

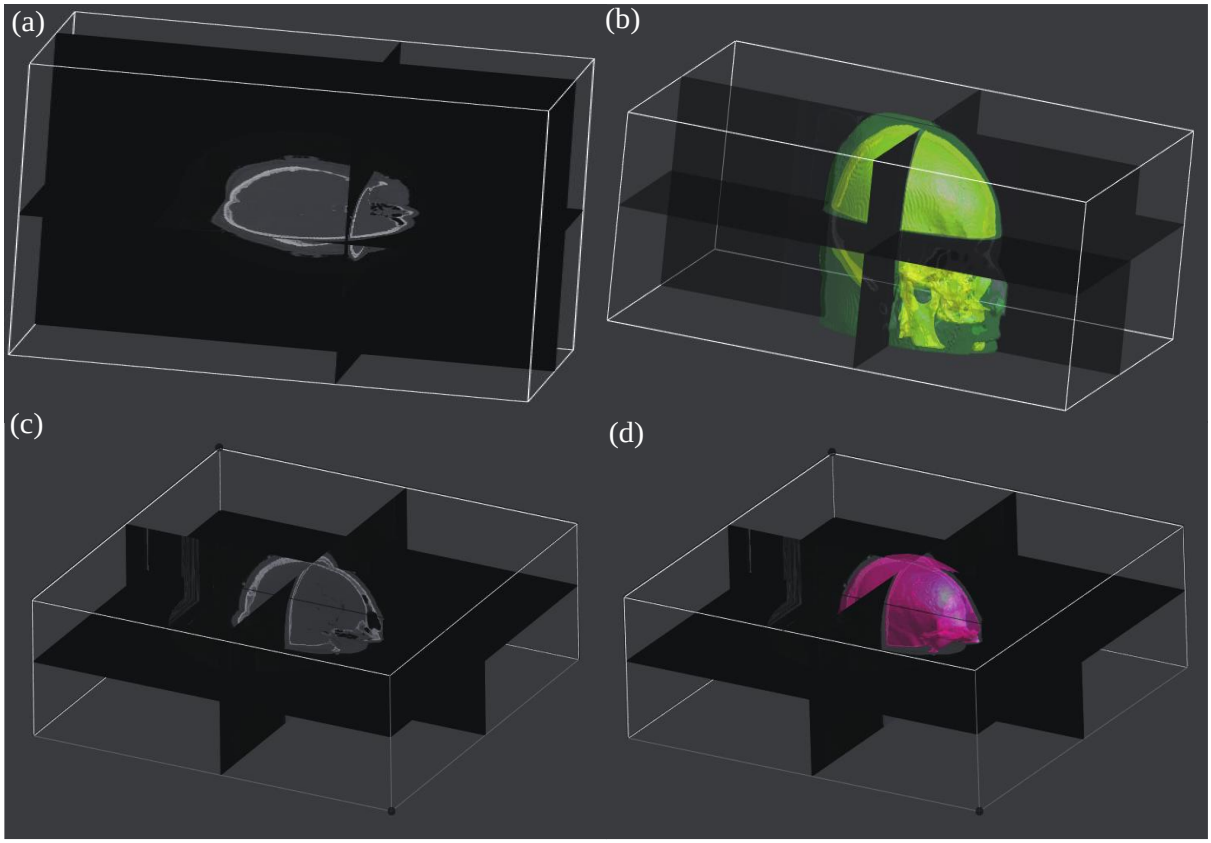

Figure 7-1 (a) CT scans of the anatomical female skull model. (b) Anatomical female skull model after segmentation. (c) CT scans of the anatomical male skull model. (d) Anatomical male skull model after segmentation

7.2.2 Acoustic Properties

The CT image data were used to calculate the acoustic parameters, such as attenuation, sound speed, and density, as these parameters have a linear relationship with the skull porosity [169, 170]. In a previous study, Aubry et al. showed that the bone porosity, Φ, can be derived from raw CT data in Hounsfield units (HU) [168]:

$$\Phi = 1 - \frac{HU}{1000} \qquad \text{Equation 7-1}$$

The skull's acoustic properties (attenuation, sound speed, and density) are then deduced from the skull porosity. Density is induced by the porosity:

$$\rho_{skull} = \rho_{water}\Phi + \rho_{bone}(1 - \Phi) \qquad \text{Equation 7-2}$$

where ρ_{water} is the density of water and ρ_{bone} is the density of the skull.

Carter and Hayes [231] showed that the elastic modulus of bone is proportional to the effective density cubed, and then sound speed could be induced as a linear relationship with the skull porosity:

$$c_{skull} = c_{water}\Phi + c_{bone}(1 - \Phi) \qquad \text{Equation 7-3}$$

where c_{water} is the sound speed of water and c_{bone} is the sound speed of the skull.

$$\alpha_{skull} = \alpha_{min,skull} + (\alpha_{max,skull} - \alpha_{min,skull})\Phi^{0.5} \qquad \text{Equation 7-4}$$

where $\alpha_{min,skull}$ is the attenuation of minimum value and $\alpha_{max,skull}$ is the attenuation of the maximum value. The skull acoustic properties of minimum and maximum attenuation were selected from [232]. The acoustic parameters listed in Table 7-2 were used to calculate the skull's attenuation, sound speed, and density.

Table 7-2 Acoustic parameters

Sound speed ($m\,s^{-1}$)	Density ($kg\,m^{-3}$)	Attenuation ($Np\,MHz^{-1}\,m^{-1}$)
$c_{water} = 1482$	ρ_{water} = 1000	$\alpha_{water} = 3.84 \times 10^{-4}$ [233]
$c_{bone} = 3100$ [169]	ρ_{bone} = 2200 [169]	$\alpha_{min,skull} = 21.5$, $\alpha_{max,skull} = 208.0$ [232]

7.2.3 Simulation setup

LAPWE is derived through fluid dynamic equations, and a partial differential equation of LAPWE is provided below:

$$\rho\nabla\frac{1}{\rho}\nabla\rho - \frac{1}{c^2}\frac{\partial^2 p}{\partial t^2} - \frac{\tilde{\alpha}}{c^2}\frac{\partial p}{\partial t} = 0$$

$$\tilde{\alpha} = 2\alpha\sqrt{\frac{\alpha^2 c^4}{\omega^2} + c^2} \qquad \text{Equation 7-5}$$

where ρ is density, c is sound speed, α is attenuation, p is pressure, t is time, and ω is the angular frequency.

The non-linear variants based on the WLE were used to generate ultrasound propagation through the skull model.

$$\rho\nabla\cdot\frac{1}{\rho}\nabla\rho - \frac{1}{c^2}\frac{\partial^2 p}{\partial t^2} + \frac{\delta}{c^4}\frac{\partial^3 p}{\partial t^3} + \frac{\beta}{2\rho c^4}\frac{\partial^2 p^2}{\partial t^2} = 0 \qquad \text{Equation 7-6}$$

where ρ is the material density, c is the sound of speed, p is the acoustic pressure, t is time, and β is the non-linearity coefficient.

7.2.4 Transducers design

The two types of transducers, including a multiple cylindrical elements transducer and a single spherical element transducer, were customised with the centre frequency at 0.5 MHz. Two transducers of the same sizes were used and placed at the top and near the temporal window (also called the acoustic window, as it is the thinnest of the skull), illustrated in Figure 7-2. The details of the transducer design, such as the transducer geometry

and source amplitude used in computational modelling, are listed in Table 7-3. Due to the character of the skull in tFUS, the customised transducers with the same radius and aperture were used to provide focal spots with enough focal lengths to the deep brain regions.

Table 7-3 Details of transducers design

	Multiple Cylindrical Element Transducers	Single Spherical Element Transducer
Curvature radius (mm)	95	95
Aperture width (mm)	50	50
Aperture length (mm)	30	/
Source amplitude (kPa)	85	60

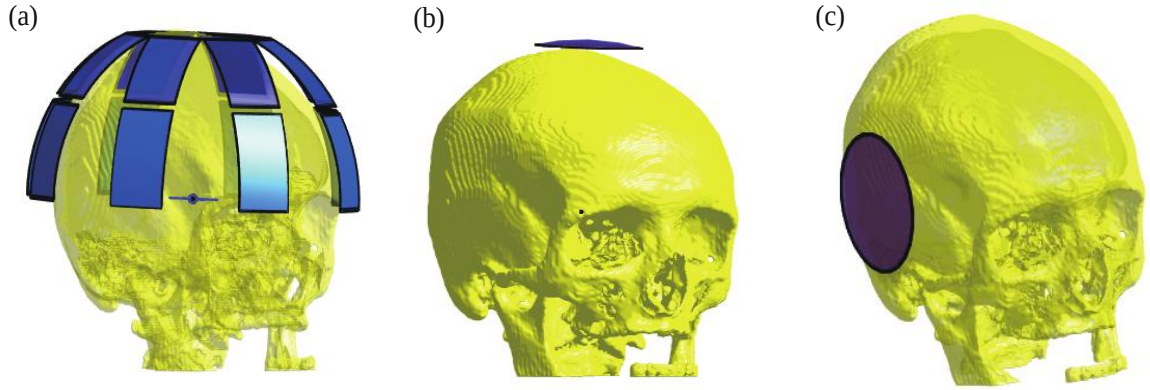

Figure 7-2 (a) Multiple cylindrical elements transducer. (b) The placement of SEFT at the top of the skull. (c) The placement of SEFT at the temporal window of the skull.

7.3 Simulations and Results

The simulations started by comparing the linear and non-linear wave propagation methods as baseline experiments in a water tank. Later, the transducers' effects were investigated, including single-element transducers and multiple cylindrical elements transducers. Also, the frequency-dependent and the skull effect with the different incidences of

wave propagation were studied. Two human head models were used to investigate variation with interpersonal differences to compare the skull morphology in acoustic wave propagation.

7.3.1 Baseline in a water tank

Table 7-4 Transducer Parameters in free water simulation

Parameters	Value
Curvature radius	90 mm
Aperture width	50 mm
Operating frequency	0.5 MHz
Medium's speed of sound	1482 m/s
Source amplitude	0.2 MPa
Source phase	0
Boundary conditions	Perfected matched layers (Absorbing boundary conditions)

The same geometry of ultrasound transducers (multiple elements transducer and single-element transducer) and source amplitude (0.2 MPa) were used to investigate spatial resolution and acoustic intensity in a water tank as the baseline. The details of transducer parameters are provided in Table 7-4. The same ultrasound input parameters and source amplitude were then used to simulate ultrasound propagation using the constructed 3D highly detailed skull model.

Table 7-5 compares the results of linear and non-linear acoustic wave propagation methods (described in section 7.2.3). Between the linear and non-linear models, there was around 1% change in peak intensity and approximately 2% change at peak pressure. Additionally, the FWHM volume only varied by 1.1%, the location of the focal spot area only changed at the major axis by 1%, and the minor axis was identical between linear and non-linear models. These results reinforce that acoustic wave propagation at LIFU is well described by LAPWE acoustic theory. Specifically, the customised multiple cylindrical elements transducer has a superior spatial resolution (the major axis is 2.63 mm, and the minor axis is 1.21

mm) and higher peak pressure than SEFT (around 3.5 times) with the same input transducer parameters.

Table 7-5 Acoustic wave propagation in a water tank

	Linear	Non-Linear	Multiple Cylindrical Elements Transducer (Linear)
Peak pressure (MPa)	2.91	2.97	10.4
Peak intensity (W/cm^2)	297	295	4784
Major axis (mm)	28.43	28.7	2.63
Minor axis (mm)	3.59	3.59	1.21
FWHM (mm^3)	256.3	259.2	2.47

7.3.2 Frequency and transducer effects

Table 7-6 Acoustic wave propagation through the skull at 0.35 MHz and 0.5 MHz

	SEFT (0.35 MHz)	Multiple Cylindrica Elements Transduc er (0.35 MHz)	SEFT (0.5 MHz)	Multiple Cylindrical Elements Transducer (0.5 MHz)
Peak pressure (MPa)	1.00	3.60	1.37	34.16
Peak intensity (W/cm^2)	34.9	657	66.8	931
Major axis (mm)	36.2	3.76	25.7	2.83
Minor axis (mm)	4.69	1.62	3.43	1.26
FWHM (mm^3)	564	7.79	214	2.56

To investigate the contribution of frequency effects to the intracranial intensity maps and spatial resolutions, simulations were run with a linear acoustic model (LAPWE) and compared the results of centre frequency at 0.5 MHz with the centre frequency at 0.35 MHz (these centre frequencies have been studies in tFUS [52, 154, 155]). Compared with a different centre frequency of SEFT, the beam profile at the focal spot area with a higher centre frequency (0.5 MHz) has a higher axial and lateral resolution

with a smaller FWHM volume and more focused intensity distribution. Typically, the spatial resolution in tFUS is mainly determined by the transducer's frequency and the geometry of transducers (curvature radius and aperture width) [154]. When using the same geometry of transducers, the FWHM volume was reduced to 214 mm^3 from 564 mm^3 with centre frequencies at 0.5 MHz and 0.35 MHZ, respectively. Also, the intracranial pressure increased by 37% when a higher frequency was used. In addition, a helmet-like phased array transducer (multiple cylindrical elements transducer) has a higher spatial resolution with a smaller focal spot area of centre frequency at 0.5 MHz (the axial and lateral resolution reach 2.83 mm and 1.26 mm). The details of the comparison of acoustic wave propagation through the skull are shown in Table 7-6. Furthermore, the visualization of the intracranial intensity distribution and the energy deposition in the skull are demonstrated in Figure 7-3. It is noted that a large amount of energy is deposited at a specific area of the skull in Figure 7-3 (c) compared with the energy dispersed to the whole parts under the transducer of the skull in Figure 7-3 (f).

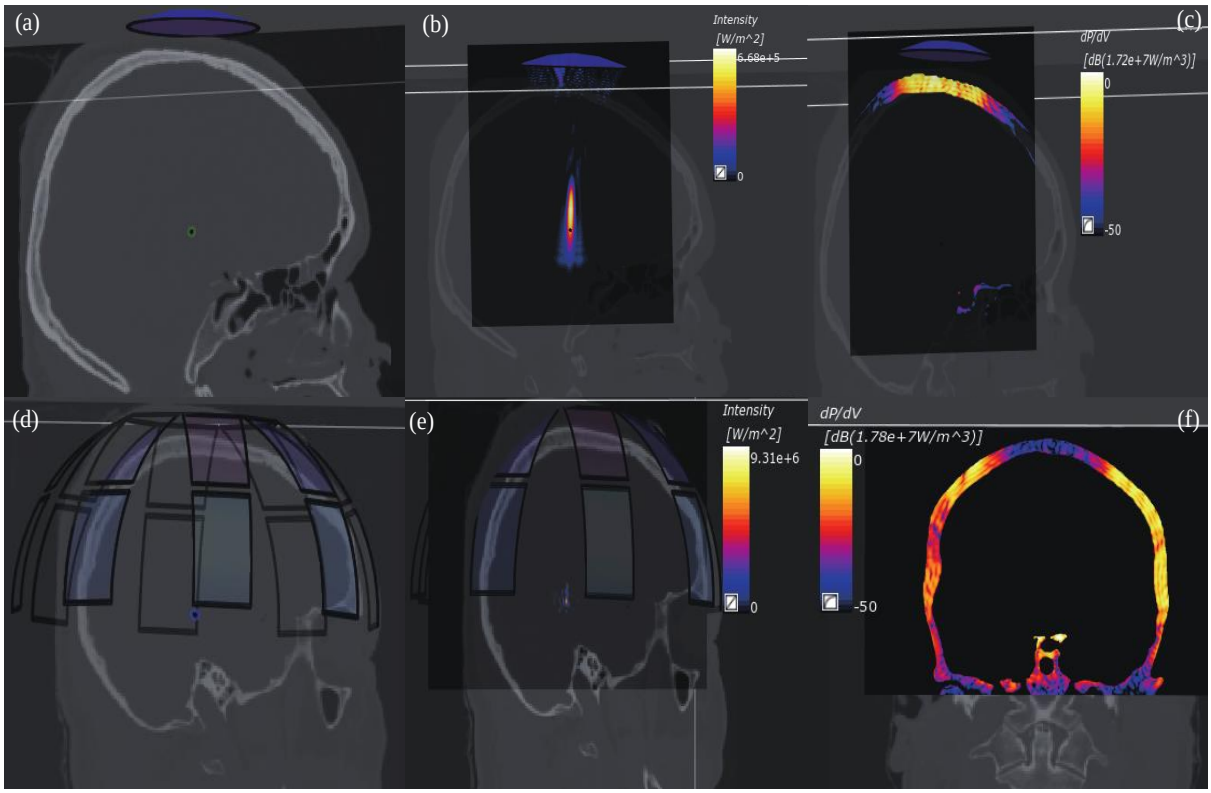

Figure 7-3 Results of ultrasound propagation within skull, (a) Skull model with SEFT. (b) Intensity distribution when acoustic waves of SEFT propagate through the skull. (c) Energy

deposition at the skull using SEFT. (d) Skull model with multiple cylindrical elements transducer. (e) Intensity distribution when acoustic waves of multiple elements transducer propagate through the skull. (f) Energy deposition at the skull multiple elements transducer.

7.3.3 Skull effects: transmission through the temporal window

The temporal window is the thinnest area of the skull and offers relatively lower resistance to acoustic transmission. We modelled the ultrasound transmission through the temporal window using the same source transducer (geometry and source amplitude of the transducer) described in previous computational models. Also, we investigated intracranial intensity distribution and energy deposition in the skull between these two different areas below the transducer and then compared the results reported in Table 7-7 and Figure 7-4. Compared to the intracranial intensity distribution when the transducer is placed over the top area of the skull, the peak intensity increased by 23.4% for transmission through the temporal window. At the same time, the FWHM volume decreased to 34.1 mm^3 through the temporal window from 214 mm^3. These results indicate that the temporal, the thinnest part of the skull, provides a site for intracranial peak intensity and optimal focal spot area using focused ultrasound. Figure 7-4 (b), (c), (e), and (f) demonstrated the energy deposition at the skull. The high absorption coefficient of the skull causes the bone to absorb large amounts of acoustic energy, which induces the radiation of the energy and thermal effects on the surrounding tissues.

Table 7-7 Results comparison of acoustic propagation through the temporal window and from the top of the skull

	Temporal Window	Top
Peak pressure (MPa)	1.32	1.37
Peak intensity (W/cm^2)	82.4	66.8
Major axis (mm)	2.82	25.7
Minor axis (mm)	1.40	3.43

FWHM (mm^3)	34.1	214

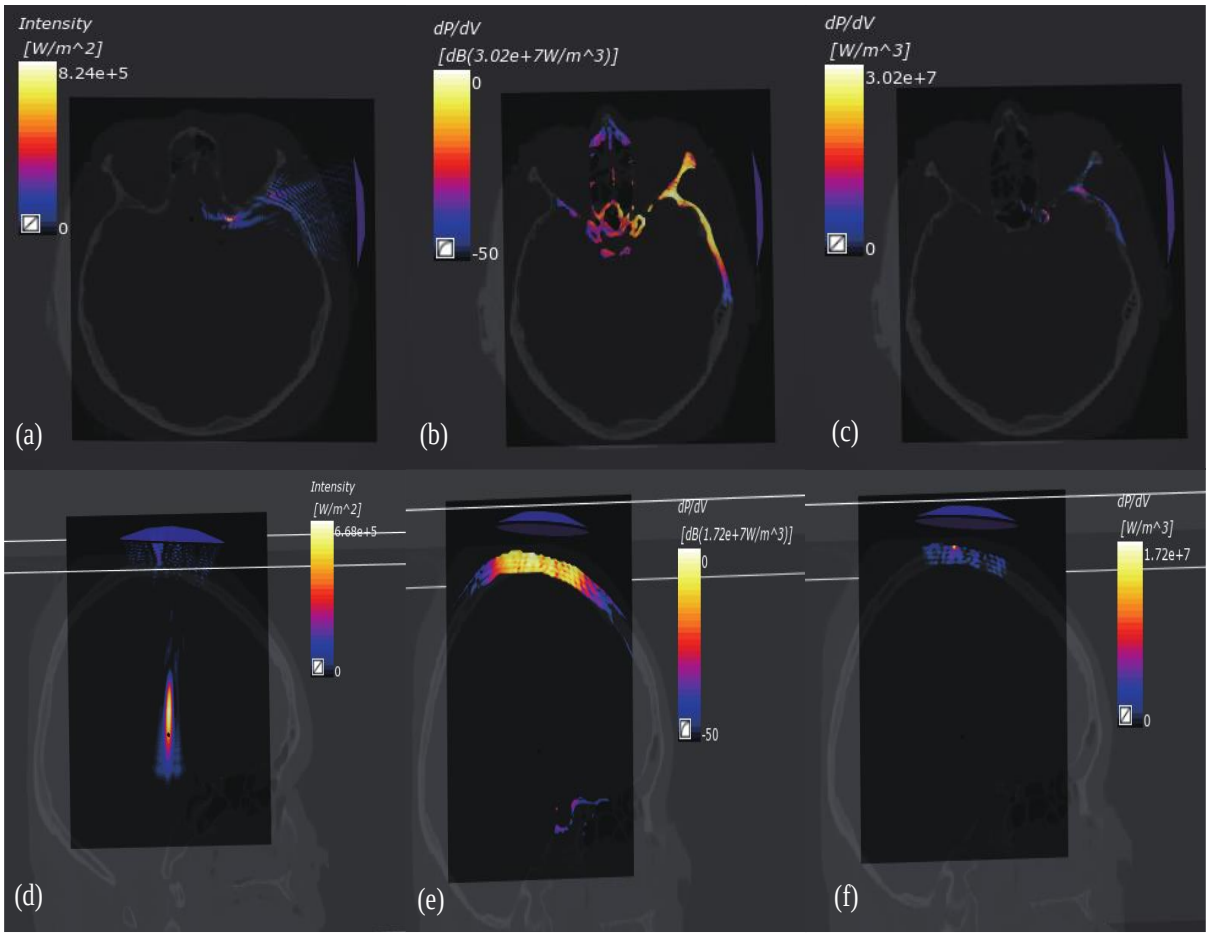

Figure 7-4 Results of acoustic waves propagate through the temporal window (first row three figures) and top of the skull (second row three figures) using SEFT. (a) Intracranial intensity distribution when SEFT is at the temporal window. (b) Energy deposition in dB reference. (c) Energy deposition in linear reference. (d) Intracranial intensity distribution when SEFT is placed at the top of the skull. (e) Energy deposition in dB reference. (f) Energy deposition in linear reference.

7.3.4 Variation with individual differences

Table 7-8 Results comparison of acoustic propagation from the top of the skull between female and male skull models

	Female Skull Model	Male Skull Model
Peak pressure (MPa)	1.37	1.70
Peak intensity (W/cm^2)	66.8	111
Major axis (mm)	25.7	19.4

Minor axis (mm)	3.43	3.23
FWHM (mm^3)	214	154

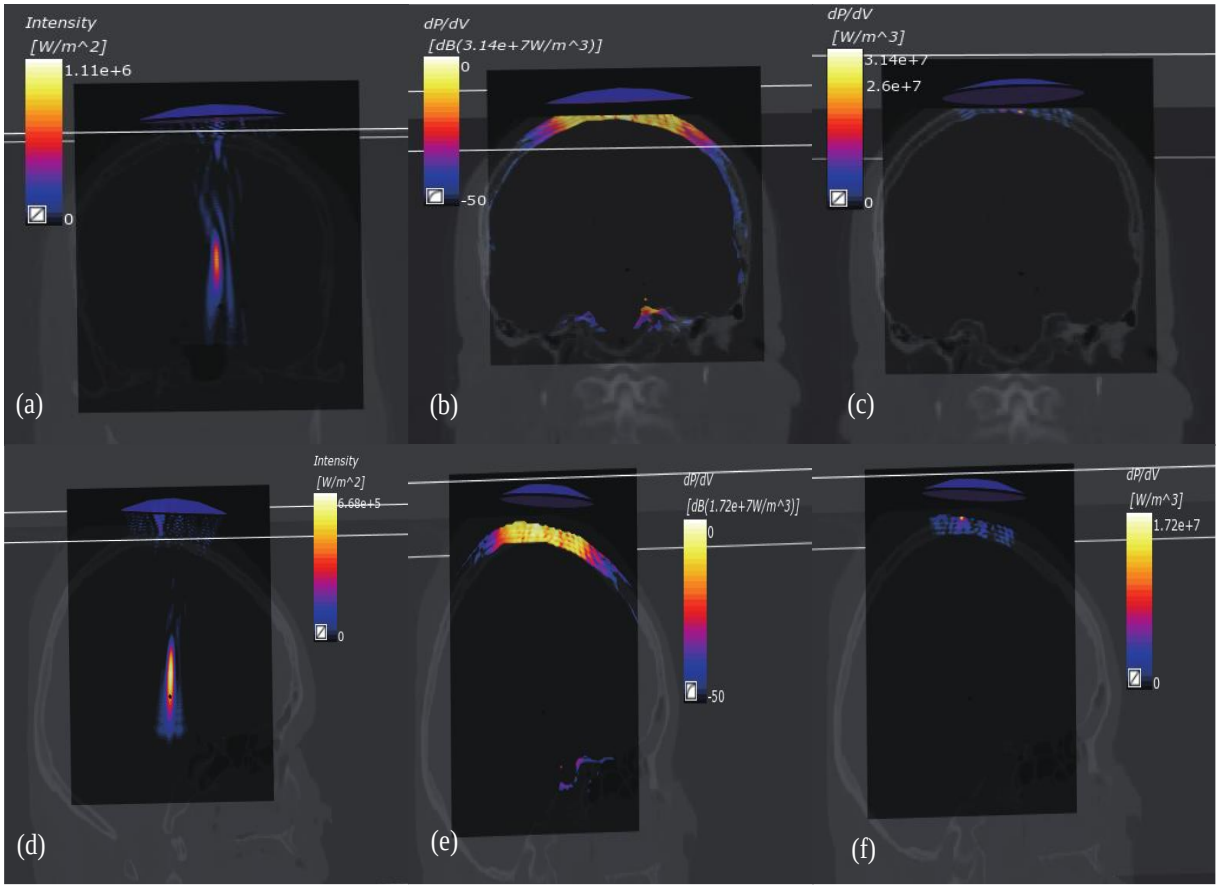

Figure 7-5 Results of acoustic waves propagate from the top of the skull; first row three figures (a)-(c) are from the male skull model, and in the second row three figures (d)-(f) are from the female skull model.

Due to the differences in skull morphology used in acoustic wave propagation, the intracranial intensity distribution, pressure, and focal spot area from focused ultrasound can vary between individuals. To investigate variation with interpersonal differences, the centre frequency at 500 kHz with the linear acoustic modelling method was used to simulate ultrasound using the same single-element transducer at the same top placement over the skull in another VHP male model (described in section 7.2.1). The intracranial peak intensity, pressure, energy deposition at the skull, and FWHM volumes were determined in the male and female skull models. The comparison results are shown in Table 7-8 and Figure 7-5. Overall, as the previous female simulation as a baseline, the peak intensity increased to

111 W/cm^2 from 66.8 W/cm^2, the intracranial pressure increased by 24.1%, and the volume of FWHM decreased by 28% in the male skull model. There was no linear relationship between the thickness of the skull and the peak intensity, pressure, and volume of FWHM. In addition, the deposition energy at the skull and intracranial intensity distribution (in Figure 7-5) were also analysed.

7.4 Discussion

The application of tFUS for neuromodulation is appealing but has diverse stimulation parameters, such as acoustic parameters and individual models, which might induce variable results. Typically, the exact location of the focal spot region and dosing of ultrasound are uncertain when using tFUS non-invasively. Specifically, the skull is the main barrier to ultrasound transmission due to frequency-dependent attenuation and ultrasound waves' dispersion, directly affecting the beam at the focal spot area and the intracranial acoustic energy. To work towards addressing the issue, this chapter developed computational modelling methods based on detailed human skull models from CT scan images for tFUS.

From the numerical results of skull effects and variation with individual differences, the intracranial intensity distribution and pressure map are determined by the overall size of the skull. Compared with the larger skulls in ultrasound propagation, the small skulls are affected more by the reflected interference with the path of the ultrasound beam. The frequency of the ultrasound is also related to the skull effects. The intracranial intensity, pressure, and FWHM volumes experienced greater changes when frequency at 0.35 MHz compared to the frequency at 0.5 MHz in the relatively smaller geometry of the female skull than the male skull. In addition, compared with the baseline experiment in a water tank, the FWHM volume reduced from 256.3 mm^3 (in a water tank) to 214 mm^3 and 154 mm^3 in the female and male skull models, respectively. Furthermore, the intracranial pressure and intensity at different ultrasound targeting

locations were investigated. The results showed that the beam profiles had a higher spatial resolution when the transducer was placed at the temporal window than over the top area of the skull. The variability between individuals and their skull geometries was also studied using computational models. The results might help to explain the variability of tFUS in research or clinical neuromodulation trials.

The CT scan images induced the acoustic properties described in section 7.2.2, and the methods were based on previous studies in [168, 169]. However, the variations in the assumed methods and acoustic parameters, such as sound speed, density, and attenuation in water and bone, might greatly influence intracranial intensity distribution, pressure, and focal spot area. Robertson et al. demonstrated that the intracranial intensity, pressure, and FWHM volume were more sensitive when the sound speed of acoustic properties was varied than density and attenuation were varied at the frequency of 0.5 MHz [234]. Similar results are shown in chapter 4 using the homogeneous skull model at 0.5 MHz [202]. In addition, there is not a linear relationship between the intensity, pressure, and FWHM volume compared to the male and female skull models, which might prove a great difference in acoustic properties between individuals. In the study of [234], Robertson et al. concluded that the 1 mm of skull thickness changes led to 5% changes in FWHM volume with the moving of the focal spot region at 2 mm, and the peak pressure changed by about 20%. The trends and observations made hold despite any errors in the methods used to capture the true values of acoustic characteristics since the methods used to assign acoustic attributes are the same for all models of the individuals utilized in this work.

This study treated all other brain tissues as water domains except the skull. Therefore, linear and non-linear models were validated in a water tank, and no significant difference was observed for peak intensity, pressure, and FWHM volumes. However, Hallaj et al. investigated linear and non-linear

acoustic models on temperature rise, and they found that the temperature rise was negligible when the source pressure was at 1 MPa. The 80% increase in the temperature rose when the source pressure was at 10 MPa using a non-linear acoustic model [235]. Another similar observation in [236] was that the thermal effects induced a significant temperature rise at source pressure around 1 MPa using the non-linear model. Thus, the linear and non-linear acoustic models may need to be considered when applying the source pressure around 1 MPa or in the complex brain models for neuromodulation.

7.5 Conclusion

These numerical results and observations, together with prior research in literature, highlight the need for realistic models of the skull and customised transducers to estimate ultrasound dosing accurately. Despite the sensitivity of the skull in the computational modelling of tFUS, it is possible to compare the acoustic effects of wave propagation through the skull in variations of individual differences if acoustic properties (the frequency, geometry of transducers, and governing equations) were kept consistent in all computational models.

Using realistic human skull models acquired from CT scan images, we simulated transcranial focused ultrasound for non-invasive neuromodulation to evaluate computational simulation approaches and intracranial intensity distribution, pressure, energy deposition, and FWHM volumes between individuals. Due to changes in skull morphology and composition, the focal spot region in the deeper brain and the dosing of focused ultrasound varies between individuals. Computational modelling methods with a realistic human head model from scan images are efficient for individual estimation. The numerical study in this chapter can aid in targeting and dosing, accounting for and lessening variability in studies addressing transcranial focused ultrasound applications.

CHAPTER 8: DISCUSSION AND CONCLUSION

The work performed in this dissertation focused on addressing the precise computational modelling and simulation of neuromodulation using transcranial focused ultrasound, with detailed human head models from MRI and CT images. In particular, the studies have investigated the spatial resolution and evaluation of the skull for neuromodulation to establish the requirements and guidelines for reliable treatment, planning in intracranial energy deposition, and BBB opening. The research issues that were identified in the literature review, such as customised design transducers, validations, sensitivity analyses, and variations in personalised modelling, have been investigated and evaluated in detail. This chapter summarises the major contributions and further research in the future.

8.1 Major contributions

- Simulation Framework
  - A detailed realistic human head model was constructed from MRI and CT images.
  - The Sim4Life platform, which includes acoustic propagation in complex anatomical environments, has been successfully extended to accommodate the detailed realistic head model.

- The ultrasound wave propagation and the energy distribution within the brain tissues using customised single-element ultrasound transducers targeting the hippocampus were investigated.
  - Computational modelling in a water tank as validation was conducted.
  - The focused ultrasound transducers were designed and optimised for precise energy deposition in the deeper brain region.
  - Sensitivity of the skull, brain, muscle, and scalp acoustic properties were analysed and evaluated.

- The MI and the CI, two metrics reflecting ultrasound-induced BBB disruption, were studied and analysed through ultrasound wave propagation in a highly detailed 3D human head model.
  - Different frequencies (centre frequency of ultrasound varied from 0.35 MHz to 0.65 MHz) were applied to compare the frequency effects on MI, CI, and FWHM.
  - The variations of skull properties, such as attenuation, sound speed, and density, were investigated in the volume of the focal spot region and intracranial pressure.
  - The effect of different incidence beam angles on MI, CI, and focal spot displacement was studied. Based on the default incidence beam angle, the deflection angles of SEFT were changed from 3° to 10°.

- The effects of LIFU with dual single-element transducers in beam profiles, including ultrasonic energy change, the volume of FWHM, and axial and lateral directions of the focal area, were investigated.
  - The adapted dual single-element transducers, consisting of two identical single transducers with 0.5 MHz central frequency, were used to simulate the ultrasonic wave propagation through a human head model. The performance of dual transducers at crossing angles from 40° to 80° was studied and evaluated in spatial resolutions, including axial, lateral, and FWHM.
  - The effect of phase difference on the intensity distribution and spatial resolution of FWHM volume was conducted, and the phase difference was set from $\frac{\lambda}{8}$ to $\frac{\lambda}{2}$ (45°, 90°, 135°, and 180°).

- A detailed study of the human skull was conducted to investigate the intracranial intensity, pressure, and focal spot area changes using computational human head models constructed using CT images. The

transducer placements and acoustic frequencies (0.35 MHz and 0.5 MHz) were also studied for female and male detailed skull models.

- human head models with detailed skull tissue identified from CT images were constructed
- The comparison of linear and non-linear acoustic wave propagation methods was conducted.
- The effects of acoustic frequencies and placements of the transducer on intracranial intensity, FWHM volumes, and energy deposition in the skull were investigated.
- The differences in transcranial acoustic wave propagation of the skull morphology were studied using computational female and male skull models.

8.2 Future work and research directions

This dissertation studied the precise applications of tFUS in four areas: the intracranial energy distribution of LIFU neuromodulation for the hippocampus, focused ultrasound-mediated BBB opening characterised by the mechanical and cavitation index, the effect of LIFU with dual DSET in beam profiles, and the evaluation of the skull for neuromodulation with focused ultrasound.

However, taking into account the needs of the scientific and medical communities and the experience of the author, the following work and research directions should be considered in the future:

- The multi-scale models of acoustic brain-activity modulation, including LIFU stimulation and EEG, could be considered for further study. It has been demonstrated that the ability of LIFU to activate neural activity non-invasively provides a high value for therapeutic purposes. The framework of the muti-scale models demonstrates promising and meaningful predictions of brain functions.

- The acoustic properties in this project have been assigned from the tissue properties database and induced by CT images. However, the acoustic properties developed from CT images contain a range of assumptions; it is necessary to consider the impact of CT image parameters and skull heterogeneity for accurate transcranial focused ultrasound simulations.

- The work on tFUS should be expanded to include inter-subject anatomical diversity and age effects. A statistical study on variation between individuals, especially for the skull models, should be considered, which provides a comparison of the effects of individual differences in skull morphology.

- Cavitation events seeded by microbubbles are associated with FUS-induced BBB opening. The computational modelling of cavitation effects on microbubbles could be further extended based on the research in chapter 5. The microbubble activity can be connected with the reversibility and permeability of the BBB opening, which is essential for the practical translation of using passive cavitation detection to monitor and manage the BBB opening.

8.3 List of publications

Huang, Y*., Wen, P., Song, B. and Li, Y., 2022. Real-Time Depth of Anaesthesia Assessment Based on Hybrid Statistical Features of EEG. *Sensors*, *22*(16), p.6099. (Q1, IF:3.847, 2022)

Huang, Y*., Wen, P., Song, B. and Li, Y., 2022. Numerical investigation of the energy distribution of Low-intensity transcranial focused ultrasound neuromodulation for hippocampus. *Ultrasonics*, *124*, p.106724. (Q1, IF:4.062, 2022)

Huang, Y*., Wen, P., Song, B. and Li, Y., 2018, December. An auto TCD probe design and visualization. In *International Conference on Brain Informatics* (pp. 486-495). Springer, Cham.

Huang, Y*., Wen, P., Song, B. and Li, Y., 2022. Numerical Evaluation of the Human Skull with Focused Ultrasound Stimulation. *Neuroscience*, October 2022. (Q1, IF:3.708, 2022)

Huang, Y*., Wen, P., Song, B. and Li, Y., Numerical Investigation on Focused Ultrasound-Mediated Blood-Brain Barrier Opening Characterised by the Mechanical Index and Cavitation Index, under review at *Neuromodulation: Technology at the Neural Interface*, October 2022. (Q1, IF:3.025, 2022)

Huang, Y*., Wen, P., Song, B. and Li, Y., Low-Intensity Transcranial Focused Ultrasound Neuromodulation Study with Dual Single-Element Transducers, under review at *Applied Acoustics*, October 2022. (Q1, IF:3.614, 2022)

Reference

1. Sparing, R. and F.M. Mottaghy, *Noninvasive brain stimulation with transcranial magnetic or direct current stimulation (TMS/tDCS)—from insights into human memory to therapy of its dysfunction.* Methods, 2008. **44**(4): p. 329-337.
2. Heo, J.-H., et al., *The effects of bilateral subthalamic nucleus deep brain stimulation (STN DBS) on cognition in Parkinson disease.* Journal of the neurological sciences, 2008. **273**(1-2): p. 19-24.
3. Mancuso, J.J., et al., *Optogenetic probing of functional brain circuitry.* Experimental physiology, 2011. **96**(1): p. 26-33.
4. McDannold, N.J., F.A. Jolesz, and K.H. Hynynen, *Determination of the optimal delay between sonications during focused ultrasound surgery in rabbits by using MR imaging to monitor thermal buildup in vivo.* Radiology, 1999. **211**(2): p. 419-426.
5. Clement, G.T., et al., *A Magnetic Resonance Imaging–Compatible, Large-Scale Array for Trans-Skull Ultrasound Surgery and Therapy.* Journal of ultrasound in medicine, 2005. **24**(8): p. 1117-1125.
6. Clement, G.T. and K. Hynynen, *A non-invasive method for focusing ultrasound through the human skull.* Physics in Medicine & Biology, 2002. **47**(8): p. 1219.
7. Fry, F., H. Ades, and W. Fry, *Production of reversible changes in the central nervous system by ultrasound.* Science, 1958. **127**(3289): p. 83-84.
8. Manlapaz, J., et al., *Effects of ultrasonic radiation in experimental focal epilepsy in the cat.* Experimental neurology, 1964. **10**(4): p. 345-356.
9. Rinaldi, P.C., et al., *Modification by focused ultrasound pulses of electrically evoked responses from an in vitro hippocampal preparation.* Brain research, 1991. **558**(1): p. 36-42.
10. Tyler, W.J., et al., *Remote excitation of neuronal circuits using low-intensity, low-frequency ultrasound.* PloS one, 2008. **3**(10): p. e3511.
11. Legon, W., et al., *Pulsed ultrasound differentially stimulates somatosensory circuits in humans as indicated by EEG and FMRI.* PloS one, 2012. **7**(12): p. e51177.
12. Kim, H., et al., *Noninvasive transcranial stimulation of rat abducens nerve by focused ultrasound.* Ultrasound in medicine & biology, 2012. **38**(9): p. 1568-1575.
13. Tufail, Y., et al., *Ultrasonic neuromodulation by brain stimulation with transcranial ultrasound.* nature protocols, 2011. **6**(9): p. 1453-1470.
14. Foley, J.L., J.W. Little, and S. Vaezy, *Image-guided high-intensity focused ultrasound for conduction block of peripheral nerves.* Annals of biomedical engineering, 2007. **35**(1): p. 109-119.
15. Gandaglia, G., et al., *Effect of minimally invasive surgery on the risk for surgical site infections: results from the National Surgical Quality Improvement Program (NSQIP) Database.* JAMA surgery, 2014. **149**(10): p. 1039-1044.
16. Hynynen, K. and R.M. Jones, *Image-guided ultrasound phased arrays are a disruptive technology for non-invasive therapy.* Physics in Medicine & Biology, 2016. **61**(17): p. R206.

17. Haworth, K.J., et al., *Towards aberration correction of transcranial ultrasound using acoustic droplet vaporization.* Ultrasound in medicine & biology, 2008. **34**(3): p. 435-445.
18. Hynynen, K., et al., *MRI-guided noninvasive ultrasound surgery.* Medical physics, 1993. **20**(1): p. 107-115.
19. Carpentier, A., et al., *Clinical trial of blood-brain barrier disruption by pulsed ultrasound.* Science translational medicine, 2016. **8**(343): p. 343re2-343re2.
20. Mishra, S., et al., *Advances in piezoelectric polymer composites for energy harvesting applications: a systematic review.* Macromolecular Materials and Engineering, 2019. **304**(1): p. 1800463.
21. Kyriakou, A., *Multi-physics computational modeling of focused ultrasound therapies*. 2015, ETH Zurich.
22. Aubry, J.-F. and T. Mickael, *Non-invasive therapy of brain disorders with focused ultrasound: From animal experiments to clinical transfer*. 2014, Université Pierre et Marie Curie-Paris VI.
23. Angelsen, B.A., et al., *Which transducer array is best?* European journal of ultrasound, 1995. **2**(2): p. 151-164.
24. Chen, D., et al., *SonoKnife for ablation of neck tissue: In vivo verification of a computer layered medium model.* International Journal of Hyperthermia, 2012. **28**(7): p. 698-705.
25. Khanna, N., et al., *Intracranial applications of MR imaging–guided focused ultrasound.* American Journal of Neuroradiology, 2017. **38**(3): p. 426-431.
26. Fisher, R., et al., *Electrical stimulation of the anterior nucleus of thalamus for treatment of refractory epilepsy.* Epilepsia, 2010. **51**(5): p. 899-908.
27. Baizabal-Carvallo, J.F., et al., *The safety and efficacy of thalamic deep brain stimulation in essential tremor: 10 years and beyond.* Journal of Neurology, Neurosurgery & Psychiatry, 2014. **85**(5): p. 567-572.
28. Wathen, C.A., et al., *Deep brain stimulation of the cerebellum for poststroke motor rehabilitation: from laboratory to clinical trial.* Neurosurgical focus, 2018. **45**(2): p. E13.
29. Davis, N.J., et al., *Challenges of proper placebo control for non-invasive brain stimulation in clinical and experimental applications.* European Journal of Neuroscience, 2013. **38**(7): p. 2973-2977.
30. Abosch, A., et al., *Long-term recordings of local field potentials from implanted deep brain stimulation electrodes.* Neurosurgery, 2012. **71**(4): p. 804-814.
31. Kalu, U., et al., *Transcranial direct current stimulation in the treatment of major depression: a meta-analysis.* Psychological medicine, 2012. **42**(9): p. 1791-1800.
32. George, M.S. and G. Aston-Jones, *Noninvasive techniques for probing neurocircuitry and treating illness: vagus nerve stimulation (VNS), transcranial magnetic stimulation (TMS) and transcranial direct current stimulation (tDCS).* Neuropsychopharmacology, 2010. **35**(1): p. 301-316.
33. Guler, S., et al., *Optimization of focality and direction in dense electrode array transcranial direct current stimulation (tDCS).* Journal of neural engineering, 2016. **13**(3): p. 036020.
34. Furubayashi, T., et al., *Short and long duration transcranial direct current stimulation (tDCS) over the human hand motor area.* Experimental brain research, 2008. **185**(2): p. 279-286.

35. Priori, A., M. Hallett, and J.C. Rothwell, *Repetitive transcranial magnetic stimulation or transcranial direct current stimulation?* Brain stimulation, 2009. **2**(4): p. 241-245.
36. Batsikadze, G., et al., *Effect of the nicotinic α4β2-receptor partial agonist varenicline on non-invasive brain stimulation-induced neuroplasticity in the human motor cortex.* Cerebral Cortex, 2015. **25**(9): p. 3249-3259.
37. Moreno-Duarte, I., et al., *Transcranial electrical stimulation: Transcranial direct current stimulation (tDCS), transcranial alternating current stimulation (tACS), transcranial pulsed current stimulation (tPCS), and transcranial random noise stimulation (tRNS)*, in *The stimulated brain*. 2014, Elsevier. p. 35-59.
38. Boccard, S.G., E.A. Pereira, and T.Z. Aziz, *Deep brain stimulation for chronic pain.* Journal of Clinical Neuroscience, 2015. **22**(10): p. 1537-1543.
39. Miocinovic, S., et al., *Outcomes, management, and potential mechanisms of interleaving deep brain stimulation settings.* Parkinsonism & related disorders, 2014. **20**(12): p. 1434-1437.
40. Foutz, T.J. and C.C. McIntyre, *Evaluation of novel stimulus waveforms for deep brain stimulation.* Journal of neural engineering, 2010. **7**(6): p. 066008.
41. Grill, W.M., *Safety considerations for deep brain stimulation: review and analysis.* Expert review of medical devices, 2005. **2**(4): p. 409-420.
42. DiLorenzo, D.J., et al., *Neurohistopathological findings at the electrode–tissue interface in long-term deep brain stimulation: systematic literature review, case report, and assessment of stimulation threshold safety.* Neuromodulation: Technology at the Neural Interface, 2014. **17**(5): p. 405-418.
43. Pirini, M., et al., *A computational modelling approach to investigate different targets in deep brain stimulation for Parkinson's disease.* Journal of computational neuroscience, 2009. **26**(1): p. 91-107.
44. Nordi, T.M., et al., *Low-Noise Amplifier for Deep-Brain Stimulation (DBS).* Electronics, 2022. **11**(6): p. 939.
45. Lefaucheur, J.-P., *Transcranial magnetic stimulation.* Handbook of clinical neurology, 2019. **160**: p. 559-580.
46. Sommer, M., et al., *Half sine, monophasic and biphasic transcranial magnetic stimulation of the human motor cortex.* Clinical neurophysiology, 2006. **117**(4): p. 838-844.
47. Fregni, F., et al., *Non-invasive brain stimulation for Parkinson's disease: a systematic review and meta-analysis of the literature.* Journal of Neurology, Neurosurgery & Psychiatry, 2005. **76**(12): p. 1614-1623.
48. George, M.S., J.J. Taylor, and E.B. Short, *The expanding evidence base for rTMS treatment of depression.* Current opinion in psychiatry, 2013. **26**(1): p. 13.
49. Chang, W.H., et al., *Long-term effects of rTMS on motor recovery in patients after subacute stroke.* Journal of rehabilitation medicine, 2010. **42**(8): p. 758-764.
50. Hamada, M., et al., *The role of interneuron networks in driving human motor cortical plasticity.* Cerebral cortex, 2013. **23**(7): p. 1593-1605.
51. Hallett, M., *Transcranial magnetic stimulation: a primer.* Neuron, 2007. **55**(2): p. 187-199.

52. King, R.L., et al., *Effective parameters for ultrasound-induced in vivo neurostimulation.* Ultrasound in medicine & biology, 2013. **39**(2): p. 312-331.
53. Younan, Y., et al., *Influence of the pressure field distribution in transcranial ultrasonic neurostimulation.* Medical physics, 2013. **40**(8): p. 082902.
54. Sun, J. and K. Hynynen, *Focusing of therapeutic ultrasound through a human skull: a numerical study.* The Journal of the Acoustical Society of America, 1998. **104**(3): p. 1705-1715.
55. Horder, M.M., et al., *In vivo heating of the guinea-pig fetal brain by pulsed ultrasound and estimates of thermal index.* Ultrasound in medicine & biology, 1998. **24**(9): p. 1467-1474.
56. Tufail, Y., et al., *Transcranial pulsed ultrasound stimulates intact brain circuits.* Neuron, 2010. **66**(5): p. 681-694.
57. Kim, H., et al., *Focused ultrasound-mediated non-invasive brain stimulation: examination of sonication parameters.* Brain stimulation, 2014. **7**(5): p. 748-756.
58. Haller, J., et al., *A comparative evaluation of three hydrophones and a numerical model in high intensity focused ultrasound fields.* The Journal of the Acoustical Society of America, 2012. **131**(2): p. 1121-1130.
59. Haar, G.t., *Ultrasound bioeffects and safety.* Proceedings of the Institution of Mechanical Engineers, Part H: Journal of Engineering in Medicine, 2010. **224**(2): p. 363-373.
60. Nyborg, W., *Acoustic streaming in Physical acoustics, Vol. II (B), ed. WP Mason*. 1965, Academic Press, New York.
61. Plesset, M.S. and A. Prosperetti, *Bubble dynamics and cavitation.* Annual review of fluid mechanics, 1977. **9**: p. 145-185.
62. Fry, W.J., et al., *Ultrasonic lesions in the mammalian central nervous system.* Science, 1955. **122**(3168): p. 517-518.
63. Martin, E., et al., *Clinical neurological HIFU applications: The Zurich experience.* Translational Cancer Research, 2014. **3**(5): p. 449-458.
64. McDannold, N., et al., *Temporary Disruption of the Blood–Brain Barrier by Use of Ultrasound and Microbubbles: Safety and Efficacy Evaluation in Rhesus MacaquesBlood–Brain Barrier Disruption via Focused Ultrasound.* Cancer research, 2012. **72**(14): p. 3652-3663.
65. Meng, Y., K. Hynynen, and N. Lipsman, *Applications of focused ultrasound in the brain: from thermoablation to drug delivery.* Nature Reviews Neurology, 2021. **17**(1): p. 7-22.
66. Folloni, D., et al., *Manipulation of subcortical and deep cortical activity in the primate brain using transcranial focused ultrasound stimulation.* Neuron, 2019. **101**(6): p. 1109-1116. e5.
67. Meng, Y., et al., *Safety and efficacy of focused ultrasound induced blood-brain barrier opening, an integrative review of animal and human studies.* Journal of Controlled Release, 2019. **309**: p. 25-36.
68. Ballantine, H., E. Bell, and J. Manlapaz, *Progress and problems in the neurological applications of focused ultrasound.* Journal of neurosurgery, 1960. **17**(5): p. 858-876.
69. Mazoue, H., P. Chauchard, and R. Busnel, *Nervous excitation with high frequency ultrasonics.* Journal de physiologie, 1953. **45**(1): p. 179-182.
70. Bachtold, M.R., et al., *Focused ultrasound modifications of neural circuit activity in a mammalian brain.* Ultrasound in medicine & biology, 1998. **24**(4): p. 557-565.

71. Koroleva, V., N. Vykhodtseva, and V. Elagin, *Cortical and subcortical spreading depression in rats produced by focused ultrasound.* Neurophysiology, 1986. **18**(1): p. 43-48.
72. Velling, V. and S. Shklyaruk, *Modulation of the functional state of the brain with the aid of focused ultrasonic action.* Neuroscience and behavioral physiology, 1988. **18**(5): p. 369-375.
73. King, R.L., J.R. Brown, and K.B. Pauly, *Localization of ultrasound-induced in vivo neurostimulation in the mouse model.* Ultrasound in medicine & biology, 2014. **40**(7): p. 1512-1522.
74. Fry, W., et al., *Physical factors involved in ultrasonically induced changes in living systems: I. Identification of non-temperature effects.* The Journal of the Acoustical Society of America, 1950. **22**(6): p. 867-876.
75. Foley, J.L., J.W. Little, and S. Vaezy, *Effects of high-intensity focused ultrasound on nerve conduction.* Muscle & Nerve: Official Journal of the American Association of Electrodiagnostic Medicine, 2008. **37**(2): p. 241-250.
76. Wahab, R.A., et al., *Mechanical bioeffects of pulsed high intensity focused ultrasound on a simple neural model.* Medical physics, 2012. **39**(7Part1): p. 4274-4283.
77. Wright, C., J. Rothwell, and N. Saffari. *Ultrasonic stimulation of peripheral nervous tissue: an investigation into mechanisms*. in *Journal of physics: Conference series*. 2015. IOP Publishing.
78. Wright, C.J., et al., *Unmyelinated peripheral nerves can be stimulated in vitro using pulsed ultrasound.* Ultrasound in medicine & biology, 2017. **43**(10): p. 2269-2283.
79. Gavrilov, L., E. Tsirulnikov, and I.a.I. Davies, *Application of focused ultrasound for the stimulation of neural structures.* Ultrasound in medicine & biology, 1996. **22**(2): p. 179-192.
80. Hameroff, S., et al., *Transcranial ultrasound (TUS) effects on mental states: a pilot study.* Brain stimulation, 2013. **6**(3): p. 409-415.
81. Mueller, J., et al., *Transcranial focused ultrasound modulates intrinsic and evoked EEG dynamics.* Brain stimulation, 2014. **7**(6): p. 900-908.
82. Lee, W., et al., *Image-guided transcranial focused ultrasound stimulates human primary somatosensory cortex.* Scientific reports, 2015. **5**(1): p. 1-10.
83. Lee, W., et al., *Simultaneous acoustic stimulation of human primary and secondary somatosensory cortices using transcranial focused ultrasound.* BMC neuroscience, 2016. **17**(1): p. 1-11.
84. Lee, W., et al., *Transcranial focused ultrasound stimulation of human primary visual cortex.* Scientific reports, 2016. **6**(1): p. 1-12.
85. Monti, M.M., et al., *Non-invasive ultrasonic thalamic stimulation in disorders of consciousness after severe brain injury: a first-in-man report.* Brain Stimul, 2016. **9**(6): p. 940-941.
86. Yoo, S.-S., et al., *Transcranial focused ultrasound to the thalamus alters anesthesia time in rats.* Neuroreport, 2011. **22**(15): p. 783.
87. Ishibashi, K., et al., *Inhibitory effects of low-energy pulsed ultrasonic stimulation on cell surface protein antigen C through heat shock proteins GroEL and DnaK in Streptococcus mutans.* Applied and Environmental Microbiology, 2010. **76**(3): p. 751-756.
88. Fry, W.J., *Intense ultrasound—a new tool for neurological research.* Journal of Mental Science, 1954. **100**(418): p. 85-96.

89. Borrelli, M., K. Bailey, and F. Dunn, *Early ultrasonic effects upon mammalian CNS structures (chemical synapses).* The Journal of the Acoustical Society of America, 1981. **69**(5): p. 1514-1516.
90. Yoo, S.-S., et al., *Focused ultrasound modulates region-specific brain activity.* Neuroimage, 2011. **56**(3): p. 1267-1275.
91. Krasovitski, B., et al., *Intramembrane cavitation as a unifying mechanism for ultrasound-induced bioeffects.* Proceedings of the National Academy of Sciences, 2011. **108**(8): p. 3258-3263.
92. Hynynen, K., et al., *Noninvasive MR imaging–guided focal opening of the blood-brain barrier in rabbits.* Radiology, 2001. **220**(3): p. 640-646.
93. Plaksin, M., E. Kimmel, and S. Shoham, *Cell-type-selective effects of intramembrane cavitation as a unifying theoretical framework for ultrasonic neuromodulation.* Eneuro, 2016. **3**(3).
94. Naor, O., et al., *Towards multifocal ultrasonic neural stimulation II: design considerations for an acoustic retinal prosthesis.* Journal of neural engineering, 2012. **9**(2): p. 026006.
95. Nelson, T.R., et al., *Ultrasound biosafety considerations for the practicing sonographer and sonologist.* 2009.
96. De Bock, M., et al., *Endothelial calcium dynamics, connexin channels and blood–brain barrier function.* Progress in neurobiology, 2013. **108**: p. 1-20.
97. Pardridge, W.M., *The blood-brain barrier: bottleneck in brain drug development.* NeuroRx, 2005. **2**(1): p. 3-14.
98. Greenwood, J., et al., *Hyperosmolar opening of the blood-brain barrier in the energy-depleted rat brain. Part 1. Permeability studies.* Journal of Cerebral Blood Flow & Metabolism, 1988. **8**(1): p. 9-15.
99. Salahuddin, T., et al., *Structural changes in the rat brain after carotid infusions of hyperosmolar solutions.* Acta neuropathologica, 1988. **77**(1): p. 5-13.
100. Chen, Y. and L. Liu, *Modern methods for delivery of drugs across the blood–brain barrier.* Advanced drug delivery reviews, 2012. **64**(7): p. 640-665.
101. Abbott, N.J., *Inflammatory mediators and modulation of blood–brain barrier permeability.* Cellular and molecular neurobiology, 2000. **20**(2): p. 131-147.
102. Karyekar, C.S., et al., *Zonula occludens toxin increases the permeability of molecular weight markers and chemotherapeutic agents across the bovine brain microvessel endothelial cells.* Journal of pharmaceutical sciences, 2003. **92**(2): p. 414-423.
103. Sanovich, E., et al., *Pathway across blood-brain barrier opened by the bradykinin agonist, RMP-7.* Brain research, 1995. **705**(1-2): p. 125-135.
104. Jones, A.R. and E.V. Shusta, *Blood–brain barrier transport of therapeutics via receptor-mediation.* Pharmaceutical research, 2007. **24**(9): p. 1759-1771.
105. Frisella, W.A., et al., *Intracranial injection of recombinant adeno-associated virus improves cognitive function in a murine model of mucopolysaccharidosis type VII.* Molecular Therapy, 2001. **3**(3): p. 351-358.
106. Kiyatkin, E.A. and H.S. Sharma, *Permeability of the blood–brain barrier depends on brain temperature.* Neuroscience, 2009. **161**(3): p. 926-939.
107. Moriyama, E., M. Salcman, and R.D. Broadwell, *Blood-brain barrier alteration after microwave-induced hyperthermia is purely a thermal*

effect: I. Temperature and power measurements. Surgical neurology, 1991. **35**(3): p. 177-182.
108. Lange, D.G. and J. Sedmak, *Japanese encephalitis virus (JEV): potentiation of lethality in mice by microwave radiation.* Bioelectromagnetics, 1991. **12**(6): p. 335-348.
109. Qiu, L.-B., et al., *The role of protein kinase C in the opening of blood–brain barrier induced by electromagnetic pulse.* Toxicology, 2010. **273**(1-3): p. 29-34.
110. Bakay, L., et al., *Ultrasonically produced changes in the blood-brain barrier.* AMA Archives of Neurology & Psychiatry, 1956. **76**(5): p. 457-467.
111. Shealy, C.N. and D. Crafts, *Selective alteration of the blood-brain barrier.* Journal of Neurosurgery, 1965. **23**(5): p. 484-487.
112. Hynynen, K. and F.A. Jolesz, *Demonstration of potential noninvasive ultrasound brain therapy through an intact skull.* Ultrasound in medicine & biology, 1998. **24**(2): p. 275-283.
113. Hosseinkhah, N., D.E. Goertz, and K. Hynynen, *Microbubbles and blood–brain barrier opening: a numerical study on acoustic emissions and wall stress predictions.* IEEE Transactions on Biomedical Engineering, 2014. **62**(5): p. 1293-1304.
114. Leighton, T., *The acoustic bubble*. 2012: Academic press.
115. Hynynen, K., *Ultrasound for drug and gene delivery to the brain.* Advanced drug delivery reviews, 2008. **60**(10): p. 1209-1217.
116. McDannold, N., N. Vykhodtseva, and K. Hynynen, *Effects of acoustic parameters and ultrasound contrast agent dose on focused-ultrasound induced blood-brain barrier disruption.* Ultrasound in medicine & biology, 2008. **34**(6): p. 930-937.
117. McDannold, N., N. Vykhodtseva, and K. Hynynen, *Targeted disruption of the blood–brain barrier with focused ultrasound: association with cavitation activity.* Physics in Medicine & Biology, 2006. **51**(4): p. 793.
118. McDannold, N., N. Vykhodtseva, and K. Hynynen, *Blood-brain barrier disruption induced by focused ultrasound and circulating preformed microbubbles appears to be characterized by the mechanical index.* Ultrasound in medicine & biology, 2008. **34**(5): p. 834-840.
119. Bing, K.F., et al., *Blood-brain barrier (BBB) disruption using a diagnostic ultrasound scanner and Definity® in mice.* Ultrasound in medicine & biology, 2009. **35**(8): p. 1298-1308.
120. Liu, H.-L., et al., *Opening of the blood-brain barrier by low-frequency (28-kHz) ultrasound: a novel pinhole-assisted mechanical scanning device.* Ultrasound in medicine & biology, 2010. **36**(2): p. 325-335.
121. Pajek, D. and K. Hynynen, *The application of sparse arrays in high frequency transcranial focused ultrasound therapy: A simulation study.* Medical physics, 2013. **40**(12): p. 122901.
122. Choi, J.J., et al., *Microbubble-size dependence of focused ultrasound-induced blood–brain barrier opening in mice in vivo.* IEEE Transactions on Biomedical Engineering, 2009. **57**(1): p. 145-154.
123. Chopra, R., N. Vykhodtseva, and K. Hynynen, *Influence of exposure time and pressure amplitude on blood− brain-barrier opening using transcranial ultrasound exposures.* ACS chemical neuroscience, 2010. **1**(5): p. 391-398.
124. Samiotaki, G., et al., *A quantitative pressure and microbubble-size dependence study of focused ultrasound-induced blood-brain barrier*

opening reversibility in vivo using MRI. Magnetic resonance in medicine, 2012. **67**(3): p. 769-777.
125. McDannold, N., N. Vykhodtseva, and K. Hynynen, *Use of ultrasound pulses combined with Definity for targeted blood-brain barrier disruption: a feasibility study.* Ultrasound in medicine & biology, 2007. **33**(4): p. 584-590.
126. Huh, H., et al., *A local difference in blood–brain barrier permeability in the caudate putamen and thalamus of a rat brain induced by focused ultrasound.* Scientific reports, 2020. **10**(1): p. 1-11.
127. Suomi, V., et al., *Full modeling of high-intensity focused ultrasound and thermal heating in the kidney using realistic patient models.* IEEE Transactions on Biomedical Engineering, 2017. **65**(5): p. 969-979.
128. Montanaro, H., et al., *The impact of CT image parameters and skull heterogeneity modeling on the accuracy of transcranial focused ultrasound simulations.* Journal of Neural Engineering, 2021. **18**(4): p. 046041.
129. Cocosco, C.A., et al. *Brainweb: Online interface to a 3D MRI simulated brain database*. in *NeuroImage*. 1997. Citeseer.
130. Shahid, S., P. Wen, and T. Ahfock, *Effects of model complexity and tissue anisotropic conductivity on cortical modulation during transcranial direct current stimulation.* IET Science, Measurement & Technology, 2012. **6**(6): p. 464-473.
131. Smith, S.M., et al., *Advances in functional and structural MR image analysis and implementation as FSL.* Neuroimage, 2004. **23**: p. S208-S219.
132. *Tissue Properties Database V4.0*, I.I. Foundation, Editor. 2018.
133. Blauert, J. and N. Xiang, *Acoustics for engineers: Troy lectures*. 2009: Springer.
134. Kamakura, T., T. Ishiwata, and K. Matsuda, *Model equation for strongly focused finite-amplitude sound beams.* The Journal of the Acoustical Society of America, 2000. **107**(6): p. 3035-3046.
135. Schafer, M., P.A. Lewin, and J.M. Reid. *Propagation through inhomogeneous media using the angular spectrum method*. in *IEEE 1987 Ultrasonics Symposium*. 1987. IEEE.
136. Neufeld, E., et al., *Approach to validate simulation-based distribution predictions combining the gamma-method and uncertainty assessment: application to focused ultrasound.* Journal of Verification, Validation and Uncertainty Quantification, 2016. **1**(3).
137. Taflove, A., S.C. Hagness, and M. Piket-May, *Computational electromagnetics: the finite-difference time-domain method.* The Electrical Engineering Handbook, 2005. **3**: p. 629-670.
138. Zienkiewicz, O.C., et al., *The finite element method: solid mechanics*. Vol. 2. 2000: Butterworth-heinemann.
139. Ginter, S., *Numerical simulation of ultrasound-thermotherapy combining nonlinear wave propagation with broadband soft-tissue absorption.* Ultrasonics, 2000. **37**(10): p. 693-696.
140. Mast, T.D., et al., *Simulation of ultrasonic pulse propagation, distortion, and attenuation in the human chest wall.* The Journal of the Acoustical Society of America, 1999. **106**(6): p. 3665-3677.
141. Westervelt, P.J., *Parametric acoustic array.* The Journal of the acoustical society of America, 1963. **35**(4): p. 535-537.

142. Yee, K., *Numerical solution of initial boundary value problems involving Maxwell's equations in isotropic media.* IEEE Transactions on antennas and propagation, 1966. **14**(3): p. 302-307.
143. Courant, R., K. Friedrichs, and H. Lewy, *On the partial difference equations of mathematical physics.* IBM journal of Research and Development, 1967. **11**(2): p. 215-234.
144. Pennes, H.H., *Analysis of tissue and arterial blood temperatures in the resting human forearm.* Journal of applied physiology, 1948. **1**(2): p. 93-122.
145. Nyborg, W.L., *Heat generation by ultrasound in a relaxing medium.* The Journal of the Acoustical Society of America, 1981. **70**(2): p. 310-312.
146. Berenger, J.-P., *A perfectly matched layer for the absorption of electromagnetic waves.* Journal of computational physics, 1994. **114**(2): p. 185-200.
147. Wang, L., et al., *Cubic lattice-based spherical uniaxial perfectly matched layer for the FDTD method.* International Journal of Numerical Modelling: Electronic Networks, Devices and Fields, 2020. **33**(2): p. e2621.
148. Chew, W.C. and W.H. Weedon, *A 3D perfectly matched medium from modified Maxwell's equations with stretched coordinates.* Microwave and optical technology letters, 1994. **7**(13): p. 599-604.
149. Constans, C., et al., *A 200–1380-kHz quadrifrequency focused ultrasound transducer for neurostimulation in rodents and primates: transcranial in vitro calibration and numerical study of the influence of skull cavity.* IEEE transactions on ultrasonics, ferroelectrics, and frequency control, 2017. **64**(4): p. 717-724.
150. Hynynen, K., et al., *500-element ultrasound phased array system for noninvasive focal surgery of the brain: A preliminary rabbit study with ex vivo human skulls.* Magnetic Resonance in Medicine: An Official Journal of the International Society for Magnetic Resonance in Medicine, 2004. **52**(1): p. 100-107.
151. Lu, M., et al., *Design and experiment of 256-element ultrasound phased array for noninvasive focused ultrasound surgery.* Ultrasonics, 2006. **44**: p. e325-e330.
152. Maimbourg, G., et al., *3D-printed adaptive acoustic lens as a disruptive technology for transcranial ultrasound therapy using single-element transducers.* Physics in Medicine & Biology, 2018. **63**(2): p. 025026.
153. Mueller, J.K., et al., *Computational exploration of wave propagation and heating from transcranial focused ultrasound for neuromodulation.* Journal of neural engineering, 2016. **13**(5): p. 056002.
154. Legon, W., et al., *Neuromodulation with single-element transcranial focused ultrasound in human thalamus.* Human brain mapping, 2018. **39**(5): p. 1995-2006.
155. Mueller, J.K., et al., *Numerical evaluation of the skull for human neuromodulation with transcranial focused ultrasound.* Journal of neural engineering, 2017. **14**(6): p. 066012.
156. Ye, P.P., J.R. Brown, and K.B. Pauly, *Frequency dependence of ultrasound neurostimulation in the mouse brain.* Ultrasound in medicine & biology, 2016. **42**(7): p. 1512-1530.
157. *Sim4Life Zurich Med Tech*. Available from: https:zurichmedtech.com/sim4life/.

158. Christov, I., C. Christov, and P. Jordan, *Modeling weakly nonlinear acoustic wave propagation.* Quarterly Journal of Mechanics and Applied Mathematics, 2007. **60**(4): p. 473-495.
159. Kyriakou, A., et al., *Full-wave acoustic and thermal modeling of transcranial ultrasound propagation and investigation of skull-induced aberration correction techniques: a feasibility study.* Journal of therapeutic ultrasound, 2015. **3**(1): p. 1-18.
160. Deffieux, T. and E.E. Konofagou, *Numerical study of a simple transcranial focused ultrasound system applied to blood-brain barrier opening.* IEEE transactions on ultrasonics, ferroelectrics, and frequency control, 2010. **57**(12): p. 2637-2653.
161. Fry, F.J. and J.E. Barger, *Acoustical properties of the human skull.* The Journal of the Acoustical Society of America, 1978. **63**(5): p. 1576-1590.
162. White, D., G. Curry, and R. Stevenson, *The acoustic characteristics of the skull.* Ultrasound in medicine & biology, 1978. **4**(3): p. 225-252.
163. Goss, S., R. Johnston, and F. Dunn, *Compilation of empirical ultrasonic properties of mammalian tissues. II.* The Journal of the Acoustical Society of America, 1980. **68**(1): p. 93-108.
164. Pulkkinen, A., et al., *Simulations and measurements of transcranial low-frequency ultrasound therapy: skull-base heating and effective area of treatment.* Physics in Medicine & Biology, 2011. **56**(15): p. 4661.
165. Pichardo, S., V.W. Sin, and K. Hynynen, *Multi-frequency characterization of the speed of sound and attenuation coefficient for longitudinal transmission of freshly excised human skulls.* Physics in Medicine & Biology, 2010. **56**(1): p. 219.
166. Samoudi, M.A., T. Van Renterghem, and D. Botteldooren, *Computational modeling of a single-element transcranial focused ultrasound transducer for subthalamic nucleus stimulation.* Journal of neural engineering, 2019. **16**(2): p. 026015.
167. Howell, B. and C.C. McIntyre, *Role of soft-tissue heterogeneity in computational models of deep brain stimulation.* Brain stimulation, 2017. **10**(1): p. 46-50.
168. Aubry, J.-F., et al., *Experimental demonstration of noninvasive transskull adaptive focusing based on prior computed tomography scans.* The Journal of the Acoustical Society of America, 2003. **113**(1): p. 84-93.
169. Marquet, F., et al., *Non-invasive transcranial ultrasound therapy based on a 3D CT scan: protocol validation and in vitro results.* Physics in Medicine & Biology, 2009. **54**(9): p. 2597.
170. Kyriakou, A., et al., *A review of numerical and experimental compensation techniques for skull-induced phase aberrations in transcranial focused ultrasound.* International Journal of Hyperthermia, 2014. **30**(1): p. 36-46.
171. Kinoshita, M., et al., *Noninvasive localized delivery of Herceptin to the mouse brain by MRI-guided focused ultrasound-induced blood–brain barrier disruption.* Proceedings of the National Academy of Sciences, 2006. **103**(31): p. 11719-11723.
172. Nance, E., et al., *Non-invasive delivery of stealth, brain-penetrating nanoparticles across the blood− brain barrier using MRI-guided focused ultrasound.* Journal of controlled release, 2014. **189**: p. 123-132.
173. Darrow, D.P., *Focused ultrasound for neuromodulation.* Neurotherapeutics, 2019. **16**(1): p. 88-99.

174. Blackmore, J., et al., *Ultrasound neuromodulation: a review of results, mechanisms and safety.* Ultrasound in medicine & biology, 2019. **45**(7): p. 1509-1536.
175. Van Rhoon, G.C., et al., *CEM43° C thermal dose thresholds: a potential guide for magnetic resonance radiofrequency exposure levels?* European radiology, 2013. **23**(8): p. 2215-2227.
176. Constans, C., et al., *Potential impact of thermal effects during ultrasonic neurostimulation: retrospective numerical estimation of temperature elevation in seven rodent setups.* Physics in Medicine & Biology, 2018. **63**(2): p. 025003.
177. Li, G.-F., et al., *Improved anatomical specificity of non-invasive neuro-stimulation by high frequency (5 MHz) ultrasound.* Scientific reports, 2016. **6**(1): p. 1-11.
178. Yang, P.S., et al., *Transcranial focused ultrasound to the thalamus is associated with reduced extracellular GABA levels in rats.* Neuropsychobiology, 2012. **65**(3): p. 153-160.
179. Kamimura, H.A., et al., *Focused ultrasound neuromodulation of cortical and subcortical brain structures using 1.9 MHz.* Medical physics, 2016. **43**(10): p. 5730-5735.
180. Gerstenmayer, M., et al., *Acoustic transmission factor through the rat skull as a function of body mass, frequency and position.* Ultrasound in medicine & biology, 2018. **44**(11): p. 2336-2344.
181. Zlokovic, B.V., *Neurovascular pathways to neurodegeneration in Alzheimer's disease and other disorders.* Nature Reviews Neuroscience, 2011. **12**(12): p. 723-738.
182. Groothuis, D.R., *The blood-brain and blood-tumor barriers: a review of strategies for increasing drug delivery.* Neuro-oncology, 2000. **2**(1): p. 45-59.
183. Abbott, N.J. and I.A. Romero, *Transporting therapeutics across the blood-brain barrier.* Molecular medicine today, 1996. **2**(3): p. 106-113.
184. Redzic, Z., *Molecular biology of the blood-brain and the blood-cerebrospinal fluid barriers: similarities and differences.* Fluids and Barriers of the CNS, 2011. **8**(1): p. 1-25.
185. Dong, X., *Current strategies for brain drug delivery.* Theranostics, 2018. **8**(6): p. 1481.
186. Upadhyay, R.K., *Drug delivery systems, CNS protection, and the blood brain barrier.* BioMed research international, 2014. **2014**.
187. McDannold, N., et al., *Temporary disruption of the blood–brain barrier by use of ultrasound and microbubbles: safety and efficacy evaluation in rhesus macaques.* Cancer research, 2012. **72**(14): p. 3652-3663.
188. Cohen-Inbar, O., Z. Xu, and J.P. Sheehan, *Focused ultrasound-aided immunomodulation in glioblastoma multiforme: a therapeutic concept.* Journal of therapeutic ultrasound, 2016. **4**(1): p. 1-9.
189. Karakatsani, M.E.M., et al., *Targeting effects on the volume of the focused ultrasound-induced blood–brain barrier opening in nonhuman primates In Vivo.* IEEE transactions on ultrasonics, ferroelectrics, and frequency control, 2017. **64**(5): p. 798-810.
190. Legon, W., et al., *Transcranial focused ultrasound modulates the activity of primary somatosensory cortex in humans.* Nature neuroscience, 2014. **17**(2): p. 322-329.

191. Foffani, G., et al., *Focused ultrasound in Parkinson's disease: A twofold path toward disease modification.* Movement Disorders, 2019. **34**(9): p. 1262-1273.
192. Götz, J., G. Richter-Stretton, and E. Cruz, *Therapeutic Ultrasound as a Treatment Modality for Physiological and Pathological Ageing Including Alzheimer's Disease.* Pharmaceutics, 2021. **13**(7): p. 1002.
193. Marquet, F., et al., *Noninvasive, transient and selective blood-brain barrier opening in non-human primates in vivo.* PloS one, 2011. **6**(7): p. e22598.
194. Wu, S.-Y., et al., *Transcranial cavitation detection in primates during blood-brain barrier opening-a performance assessment study.* IEEE transactions on ultrasonics, ferroelectrics, and frequency control, 2014. **61**(6): p. 966-978.
195. Cho, H., et al., *Localized down-regulation of P-glycoprotein by focused ultrasound and microbubbles induced blood-brain barrier disruption in rat brain.* Scientific reports, 2016. **6**(1): p. 1-10.
196. McMahon, D., R. Bendayan, and K. Hynynen, *Acute effects of focused ultrasound-induced increases in blood-brain barrier permeability on rat microvascular transcriptome.* Scientific reports, 2017. **7**(1): p. 1-15.
197. Pinton, G., et al., *Attenuation, scattering, and absorption of ultrasound in the skull bone.* Medical physics, 2012. **39**(1): p. 299-307.
198. Hynynen, K., et al., *Local and reversible blood–brain barrier disruption by noninvasive focused ultrasound at frequencies suitable for trans-skull sonications.* Neuroimage, 2005. **24**(1): p. 12-20.
199. Chu, P.-C., et al., *Focused ultrasound-induced blood-brain barrier opening: association with mechanical index and cavitation index analyzed by dynamic contrast-enhanced magnetic-resonance imaging.* Scientific reports, 2016. **6**(1): p. 1-13.
200. McMahon, D., C. Poon, and K. Hynynen, *Evaluating the safety profile of focused ultrasound and microbubble-mediated treatments to increase blood-brain barrier permeability.* Expert opinion on drug delivery, 2019. **16**(2): p. 129-142.
201. Tech, Z.M. *Sim4Life*. Available from: https://zmt.swiss/.
202. Huang, Y., et al., *Numerical Investigation of the Energy Distribution of Low-intensity Transcranial Focused Ultrasound Neuromodulation for Hippocampus.* Ultrasonics, 2022: p. 106724.
203. Holland, C.K. and R.E. Apfel, *An improved theory for the prediction of microcavitation thresholds.* IEEE transactions on ultrasonics, ferroelectrics, and frequency control, 1989. **36**(2): p. 204-208.
204. Apfel, R.E. and C.K. Holland, *Gauging the likelihood of cavitation from short-pulse, low-duty cycle diagnostic ultrasound.* Ultrasound in medicine & biology, 1991. **17**(2): p. 179-185.
205. Bader, K.B. and C.K. Holland, *Gauging the likelihood of stable cavitation from ultrasound contrast agents.* Physics in Medicine & Biology, 2012. **58**(1): p. 127.
206. Kong, C., et al., *Factors Associated with Energy Efficiency of Focused Ultrasound Through the Skull: A Study of 3D-Printed Skull Phantoms and Its Comparison with Clinical Experiences.* Frontiers in Bioengineering and Biotechnology, 2021. **9**.
207. Park, T.Y., K.J. Pahk, and H. Kim, *Method to optimize the placement of a single-element transducer for transcranial focused ultrasound.* Computer Methods and Programs in Biomedicine, 2019. **179**: p. 104982.

208. Nitsche, M.A., et al., *Transcranial direct current stimulation: state of the art 2008.* Brain stimulation, 2008. **1**(3): p. 206-223.
209. Perlmutter, J.S. and J.W. Mink, *Deep brain stimulation.* Annu. Rev. Neurosci., 2006. **29**: p. 229-257.
210. Walsh, V. and A. Cowey, *Transcranial magnetic stimulation and cognitive neuroscience.* Nature Reviews Neuroscience, 2000. **1**(1): p. 73-80.
211. Bronstein, J.M., et al., *Deep brain stimulation for Parkinson disease: an expert consensus and review of key issues.* Archives of neurology, 2011. **68**(2): p. 165-165.
212. Dallapiazza, R.F., et al., *Noninvasive neuromodulation and thalamic mapping with low-intensity focused ultrasound.* Journal of neurosurgery, 2017. **128**(3): p. 875-884.
213. Tyler, W.J., S.W. Lani, and G.M. Hwang, *Ultrasonic modulation of neural circuit activity.* Current opinion in neurobiology, 2018. **50**: p. 222-231.
214. Wattiez, N., et al., *Transcranial ultrasonic stimulation modulates single-neuron discharge in macaques performing an antisaccade task.* Brain stimulation, 2017. **10**(6): p. 1024-1031.
215. Naor, O., S. Krupa, and S. Shoham, *Ultrasonic neuromodulation.* Journal of neural engineering, 2016. **13**(3): p. 031003.
216. Kim, H., et al., *Miniature ultrasound ring array transducers for transcranial ultrasound neuromodulation of freely-moving small animals.* Brain stimulation, 2019. **12**(2): p. 251-255.
217. Song, J. and K. Hynynen, *Feasibility of using lateral mode coupling method for a large scale ultrasound phased array for noninvasive transcranial therapy.* IEEE transactions on biomedical engineering, 2009. **57**(1): p. 124-133.
218. Jiang, Y., et al., *Optoacoustic brain stimulation at submillimeter spatial precision.* Nature communications, 2020. **11**(1): p. 1-9.
219. Lee, W., et al., *Image-guided focused ultrasound-mediated regional brain stimulation in sheep.* Ultrasound in medicine & biology, 2016. **42**(2): p. 459-470.
220. Pouliopoulos, A.N., et al., *A clinical system for non-invasive blood–brain barrier opening using a neuronavigation-guided single-element focused ultrasound transducer.* Ultrasound in medicine & biology, 2020. **46**(1): p. 73-89.
221. Nyborg, W.L., *Biological effects of ultrasound: development of safety guidelines. Part II: general review.* Ultrasound in medicine & biology, 2001. **27**(3): p. 301-333.
222. Lee, H.I., et al., *Pre-conditioning with transcranial low-level light therapy reduces neuroinflammation and protects blood-brain barrier after focal cerebral ischemia in mice.* Restorative neurology and neuroscience, 2016. **34**(2): p. 201-214.
223. Li, X., et al., *Seizure control by low-intensity ultrasound in mice with temporal lobe epilepsy.* Epilepsy research, 2019. **154**: p. 1-7.
224. Pernot, M., et al., *High power transcranial beam steering for ultrasonic brain therapy.* Physics in Medicine & Biology, 2003. **48**(16): p. 2577.
225. Hatakeyama, R., et al., *Measurement of speed of sound in skull bone and its thickness using a focused ultrasonic wave.* Japanese journal of applied physics, 2002. **41**(5S): p. 3327.
226. Clement, G.T., P.J. White, and K. Hynynen, *Enhanced ultrasound transmission through the human skull using shear mode conversion.* The Journal of the Acoustical Society of America, 2004. **115**(3): p. 1356-1364.

227. Top, C.B., P.J. White, and N.J. McDannold, *Nonthermal ablation of deep brain targets: a simulation study on a large animal model.* Medical physics, 2016. **43**(2): p. 870-882.
228. Ackerman, M.J., *The visible human project.* Proceedings of the IEEE, 1998. **86**(3): p. 504-511.
229. Lorensen, B., *Visible Human Project DICOM CT Datasets*. 1995.
230. Foundation, I.I., *The Medical Image Segmentation Tool Set iSEG*. 2018.
231. Carter, D.R. and W.C. Hayes, *The compressive behavior of bone as a two-phase porous structure.* The Journal of bone and joint surgery. American volume, 1977. **59**(7): p. 954-962.
232. Connor, C.W., *Simulation methods and tissue property models for non-invasive transcranial focused ultrasound surgery*. 2005, Massachusetts Institute of Technology.
233. Pinkerton, J.M., *The absorption of ultrasonic waves in liquids and its relation to molecular constitution.* Proceedings of the Physical Society. Section B, 1949. **62**(2): p. 129.
234. Robertson, J., et al., *Sensitivity of simulated transcranial ultrasound fields to acoustic medium property maps.* Physics in Medicine & Biology, 2017. **62**(7): p. 2559.
235. Hallaj, I.M. and R.O. Cleveland, *FDTD simulation of finite-amplitude pressure and temperature fields for biomedical ultrasound.* The Journal of the Acoustical Society of America, 1999. **105**(5): p. L7-L12.
236. Holt, R.G. and R.A. Roy, *Measurements of bubble-enhanced heating from focused, MHz-frequency ultrasound in a tissue-mimicking material.* Ultrasound in medicine & biology, 2001. **27**(10): p. 1399-1412.